A CERENKOV-ΔE-CERENKOV DETECTOR FOR HIGH ENERGY COSMIC RAY ISOTOPES and AN ACCELERATOR STUDY OF ^{40}Ar & ^{56}Fe FRAGMENTATION

Thesis by

Koon H. Lau

In Partial Fulfillment of the Requirements
for the Degree of
Doctor of Philosophy

California Institute of Technology
Pasadena, California

1985
(Submitted May 31, 1985)

Acknowledgements

I wish to thank my advisor, Professor Edward Stone, for his guidance and support throughout my graduate years at Caltech. His advice, both on technical problems and on my personal growth as an experimental physicist, was very much appreciated.

I also thank Drs. Andrew Buffington and Stephen Schindler, not only for their design and development efforts on HEIST, but also for their numerous contributions to my education as a physicist. Thanks are also due to Dr. Ib Rasmussen and Mr. Steen Laursen of the Danish Space Research Institute for their collaborations on the HEIST project. In addition, I would like to thank Ib for his advice on both technical and personal problems. His company on the basketball and badminton courts provided some much-needed relief from the intense preparation work for the Bevalac calibration.

I would like to thank Drs. Dick Mewaldt and Mark Wiedenbeck for their collaboration on the fragmentation studies. Their advice on m[illegible]ccasions was very much needed and appreciated.

I am very grateful to Mr. William Althouse. His guidance and advice on the electronics designs for HEIST was invaluable. I have also learned and benefited a great deal from our many discussions on electronics, computers, and system designs.

John South and Wallace Campbell provided excellent design and support on the HEIST electronics. Brownlee Gauld provided a great deal of programming assistance and some very appreciated consulting. Former undergraduates Bruce Pricket and Kent Neuberger provided valuable assistance in the early stages of the experiment and the Bevalac calibrations. Graduate students Eric Christian and Eric Grove also provided a great deal of much-

needed help on HEIST. They have also made the office more livable.

I am grateful to the Heckman/Greiner group at the Lawrence Berkeley Laboratory, especially Dr. Hank Crawford, for assisting with the accelerator calibrations.

I would like to thank the University of California, Berkeley, for the unique undergraduate education. Not only did I get a solid background in physics, but I also learned to be aware of social problems and to be responsible to the community which I live in. I am grateful to my parents, my two brothers, Steve and James, for their constant support throughout the years. Finally, my deepest thanks are due to my wife, Janet, for her love and support in the last few years. Her criticism of the form and content of this thesis was much appreciated.

This work was supported in part by NASA under grants NGR 05-002-160 and NAG 5-308.

Abstract

This thesis has two major parts. The first part of the thesis will describe a high energy cosmic ray detector -- the High Energy Isotope Spectrometer Telescope (HEIST). HEIST is a large area (0.25 m^2sr) balloon-borne isotope spectrometer designed to make high-resolution measurements of isotopes in the element range from neon to nickel ($10 \leq Z \leq 28$) at energies of about 2 GeV/nucleon. The instrument consists of a stack of 12 NaI(Tl) scintillators, two Cerenkov counters, and two plastic scintillators. Each of the 2-cm thick NaI disks is viewed by six 1.5-inch photomultipliers whose combined outputs measure the energy deposition in that layer. In addition, the six outputs from each disk are compared to determine the position at which incident nuclei traverse each layer to an accuracy of ~2 mm. The Cerenkov counters, which measure particle velocity, are each viewed by twelve 5-inch photomultipliers using light integration boxes.

HEIST-2 determines the mass of individual nuclei by measuring both the change in the Lorentz factor ($\Delta\gamma$) that results from traversing the NaI stack, and the energy loss (ΔE) in the stack. Since the total energy of an isotope is given by $E = \gamma M$, the mass M can be determined by $M = \Delta E/\Delta\gamma$. The instrument is designed to achieve a typical mass resolution of 0.2 amu.

The second part of this thesis presents an experimental measurement of the isotopic composition of the fragments from the breakup of high energy ^{40}Ar and ^{56}Fe nuclei. Cosmic ray composition studies rely heavily on semi-empirical estimates of the cross-sections for the nuclear fragmentation reactions which alter the composition during propagation through the interstellar medium. Experimentally measured yields of isotopes from the fragmentation of ^{40}Ar and ^{56}Fe are compared with calculated yields based on semi-empirical cross-section formulae. There are two sets of measurements. The first set of measurements, made at the Lawrence Berkeley Laboratory Bevalac using a beam of 287 MeV/nucleon ^{40}Ar incident on a CH_2 target, achieves excellent mass resolution ($\sigma_m \leq 0.2$ amu) for isotopes of Mg through K using a Si(Li) detector telescope. The second set of measurements, also made at the Lawrence Berkeley Laboratory Bevalac, using a beam of 583 MeV/nucleon ^{56}Fe incident on a CH_2 target, resolved Cr, Mn, and Fe fragments with a typical mass resolution of ~ 0.25 amu, through the use of the Heavy Isotope Spectrometer Telescope (HIST) which was later carried into space on ISEE-3 in 1978. The general agreement between calculation and experiment is good, but some significant differences are reported here.

Table of Contents

Chapter 1

Introduction

Cosmic rays represent a directly accessible sample of material from other regions of the galaxy. Measurements of cosmic ray abundances can provide information on the environments under which these particles were synthesized. Because cosmic rays are extremely young ($\sim 10^7$ yr.) in comparison with the solar system which condensed $\sim 4.6\times 10^9$ yr. ago, it is of interest to know how astrophysical conditions for nucleosynthesis differ from those of solar system material. To do this, one must determine the isotopic composition of the cosmic ray source material. The cosmic ray abundances observed near earth are contaminated by the products of nuclear interactions suffered in the interstellar medium. Since the cross-sections for such interactions are mass-dependent, only by measuring the isotopic composition can one adequately deconvolve observed abundances into source abundances and at the same time understand the nature of the galactic propagation process. Cosmic ray isotope measurements can also be used to determine the age of cosmic rays if radioactive nuclides, such as ^{26}Al, with half-lives of the order of the cosmic ray age can be resolved from the more abundant neighboring isotopes.

According to Woosley and Weaver (1981), isotopic abundances of cosmic rays have implications for the metallicity (and neutron excess) of the sites for nucleosynthesis. Moreover, Woosley (1976) has considered the implications of non-solar isotope ratios for cosmic ray Fe-peak elements (Cr through Ni) and shows that isotope ratios are sensitive functions of the neutron excess. Cosmic ray relative abundances for neutron-rich isotopes of the elements Ne, Mg, and Si have been discovered to be enhanced when compared to their relative abundances in the solar system (e.g., Mewaldt, Spalding, and Stone, 1980; and Wiedenbeck and Greiner, 1981). Isotopes for higher charge elements generally have lower abundances, and have not yet been measured with sufficient statistical accuracy to determine if the cosmic ray and solar system compositions differ.

In the first part (Chapter 2) of this thesis, we will describe a new high-resolution cosmic ray mass spectrometer with a relatively large geometry factor. The instrument, the High Energy Isotope Spectrometer Telescope (HEIST), is designed to make high-resolution measurements of isotopes for the elements ranging from neon to nickel. A Cerenkov-ΔE-Cerenkov technique is employed. This technique involves measuring the velocity (or Lorentz factor) of a particle before and after the particle traverses an energy absorbing medium (NaI), which also measures the energy loss of the particle. This technique will be discussed in detail in section 2.1. In addition, the mass uncertainty contributions associated with this technique will be analyzed.

HEIST will analyze particles with incident energies from 1.3 GeV/nucleon to above 2 GeV/nucleon. The relatively high energy which this instrument covers has some advantages. First of all, interpretative difficulties such as energy dependent cross-sections, solar modulation, and correction for dE/dx losses, which are most important at low energies, can be minimized. In addition, balloon flights are most easily and inexpensively carried out at the National Scientific Balloon Facility at Palestine, Texas, where the geomagnetic cutoff limits observations to particles above a rigidity of about 4.5 GV/c (Lorentz factor of about 2.5). Finally, observations from this instrument will also be the first high-resolution measurements in this energy range.

With the combination of good mass resolution and large geometry factor, this instrument is expected to provide improved observations of the isotopic composition for the elements Ne, Mg, Si, and Fe; at the same time, it also has the potential for yielding the first well-resolved observations of some interesting, but rare, isotopes. In addition, since our observations will be done at high energy, they can be compared to those done at lower energies to identify any possible energy dependence of isotopic abundances.

Several innovations have been incorporated into this instrument. In particular, the stack of NaI scintillators is used to measure the trajectory of the incident particles as well as to measure energy loss. These high-resolution (about 2mm rms) trajectory measurements make it possible to make corrections for variations of light collection efficiency in the scintillators and the Cerenkov counters. Large-area trajectory measurements are traditionally done with gas-filled multi-wire proportional counters. The elimination of a non-solid state device from our instrument may make possible future space qualification easier.

The overall system design of HEIST-2 will be presented in section 2.2. In section 2.3, we will describe the NaI scintillator stack and will discuss how a position resolution of about 2 mm can be achieved with this kind of scintillator. Scintillation efficiency of NaI will also be discussed briefly. In section 2.4, we will describe the Cerenkov counters and will discuss why photoelectron statistical fluctuations in these counters will be the dominating factor in the mass measurement uncertainty. In the last section of chapter 2, we will discuss the expected mass resolution of HEIST-2.

In the second part (chapter 3) of this thesis, we will present an experimental measurement of the isotopic composition of the fragments from the breakup of high energy ^{40}Ar and ^{56}Fe nuclei. Cosmic ray composition studies rely heavily on the cross-sections for nuclear fragmentation reactions in order to correct for alterations that occur in the composition during propagation through the interstellar medium. Therefore, it is not adequate to only improve the statistical accuracy of cosmic ray composition observations, but it is also necessary to obtain precise values (at least relative values) for the nuclear fragmentation cross-sections. Direct measurements of a wide range of nuclear fragmentation reactions would be desirable. However, these measurements are tedious and very time consuming. Today, most of the propagation calculations rely heavily on semi-empirical cross-section formulae.

A semi-empirical cross-section formula was first derived by Rudstam (1955, 1956, 1966, 1969), to fit experimental data, and later extended by several authors (see for example Bernas et al. 1967, Audouze et al. 1967, and Beck and Yiou 1968). These formulae, however, are designed for specific applications and have inherent limits to their usage. In 1973, Silberberg and Tsao (1973a,b) constructed a semi-empirical formula for a more general application. Using experimental cross-sections, a semi-empirical equation was developed for calculating cross-sections of proton interactions with various target nuclei :

$$\sigma = \sigma_o \cdot f(A) \cdot f(E) \cdot e^{-P \cdot \Delta A} \cdot \exp(-R \cdot \left| Z - S \cdot A + T \cdot A^2 \right|^{\nu}) \cdot \Omega \cdot \eta \cdot \xi . \qquad (1.1)$$

This equation is applicable for calculating cross-sections of targets having mass numbers in the range of $9 \leq A_t \leq 209$ and products with $6 \leq A \leq 200$, except for very large and small values of ΔA (i.e., $A_t - A$). The correction factors f(A) and f(E) are applicable only to products from heavy targets with $Z_t > 30$, when ΔA is very large. They are set to 1 for $Z_t \leq 30$. The factor $e^{-P \cdot \Delta A}$ describes the diminution of cross-sections as the difference between the target and product mass, ΔA, increases. The factor $\exp(-R\cdot|Z-S\cdot A+T\cdot A^2|^{\nu})$ describes the distribution of cross-sections for the production of various isotopes of an element of atomic number Z. The width of the distribution of cross-sections is represented by the parameter R. The parameter S describes the location of the peaks of these distribution curves. The parameter T describes the shift of the distribution curves toward greater neutron excess as the atomic number of the product increases. The factor ν is usually 2 except for $21 \leq Z_t$. The factor Ω is related to nuclear structure. The factor η is the nucleon pairing factor of the product nuclides for the different combinations of proton-neutron numbers : even-even, odd N, odd Z, and odd-odd. The factor ξ represents an enhancement factor for light evaporation products. The factor σ_o gives the overall normalization factor for the cross-sections.

Silberberg and Tsao also found that the cross-sections cease to decrease with decreasing values of A. Hence, for large values of ΔA, ΔA_c is substituted in equation (1.1), where :

$$\Delta A_c = \begin{cases} 31.5+0.052\cdot(A_t-36)\cdot(\ln E-3.17) & E<E_o \\ 31.5+0.045\cdot(A_t-36)\cdot(\ln A_t+1.23) & E\geq E_o \end{cases} \qquad (1.2)$$

and $E_o = 69\cdot A_t^{0.867}$. The substitution is made if $\Delta A \geq \Delta A_c$. The energy E is expressed in units of MeV; E_o is the critical energy above which no significant change in the values of cross-sections is expected.

For very small values of ΔA, peripheral types of reactions play a dominant role. The general form of the cross-sections for peripheral reactions is

$$\sigma_p = \sigma(E_o)\cdot H(E)\cdot Y(A_t,Z_t)\cdot \varphi(A_t,E). \qquad (1.3)$$

Here $\sigma(E_o)$ is the high-energy value of the cross-sections, i.e., at the energy

E_o above which the cross-sections are approximately independent of energy. The function H(E) represents the energy dependence of the cross-sections. The factor $Y(A_t,Z_t)$ corrects for the neutron excess or deficiency of target nuclei. The normalization factor $\varphi(A_t,E)$ is not used here (applicable for $157 \leq A_t$) and is set to 1. Equation (1.3) is used whenever the number of neutrons emitted is less than or equal to x_{max}. The correction functions and parameters used in equations (1.1) and (1.3) as well as x_{max} are given in Silberberg and Tsao (1973a,b).

Based on new experimental data, Silberberg and Tsao (1977b, 1979) revised some of the parameters used in the above cross-sections equations. These updated parameter are used in our Monte Carlo calculations.

Cross-sections for charge exchange reactions are given by Silberberg and Tsao (1977a)

$$\sigma(E) = \sigma(E_o) \cdot G(E) \cdot H(Z_t,x) \cdot \Omega. \qquad (1.4)$$

Again $\sigma(E_o)$ is the high-energy value of the cross-sections. The function G(E) describes the energy dependence of the cross-sections. Evaporation of neutrons is reduced by competition from fission, and this is described by the correction factor $H(Z_t,x)$ where x is the number of neutrons emitted. The factor Ω is the nuclear structure factor which has different values from the one used in equation (1.1).

Cross-sections for fragmentation on heavier nuclei (other than hydrogen) are scaled from proton-nuclei cross-sections using the scaling formula of Silberberg and Tsao (1977c)

$$\sigma(N_1,N_2) = \sigma(N_1,p) \cdot S_c \cdot \varepsilon_n \cdot \varepsilon_L \cdot \varepsilon_1 \cdot \varepsilon_\Delta. \qquad (1.5)$$

Here $\sigma(N_1,p)$ is calculated, using equations (1.1) through (1.4), at proton energy equal to that of the total kinetic energy of the nucleus. The scaling factor S_c is a function of the nuclear skin thickness. The other factors ε_n, ε_L, ε_1, and ε_Δ respectively represent correction terms for neutron-deficient products, light products, single-nucleon stripping, and for reactions with large ΔA.

It is necessary to test these semi-empirical formulae so that the accuracy of the formulae can be determined and systematic deficiencies can be identified and corrected. In this thesis, we will present a method which provides a mechanism for testing the semi-empirical formulae without directly measuring cross-sections. This method involves the comparison of experimentally measured fragmentation yields with those expected from a Monte Carlo simulation calculation based on the semi-empirical cross-section formulae. Even though this method does not provide absolute measurements of the cross-sections and their energy dependence, any systematic difference between the measurements and calculations can be used as a basis for refining the semi-empirical formulae.

In chapter 3 of this thesis, we will analyze two sets of experimental data to obtain relative yields of isotopes from the fragmentation of ^{40}Ar and ^{56}Fe. These measured fragmentation yields will be compared with calculated yields based on the semi-empirical cross-section formulae. Systematic differences between the measured and calculated yields will be reported.

Chapter 2

The High Energy Isotope Spectrometer Telescope

The High Energy Isotope Spectrometer Telescope is a balloon-borne mass spectrometer which utilizes the Cerenkov-ΔE-Cerenkov technique for resolving mass. Dr. Andrew Buffington was responsible for the conception of the design for this instrument. The instrument consists of a top Cerenkov counter (with index of refraction $n = 1.10$) and a bottom Cerenkov counter (a combination of $n = 1.34$ and $n = 1.49$) with a stack of 12 NaI scintillators (~90 gm/cm^2 total thickness) in between the two Cerenkov counters. There are two 1 cm thick plastic scintillators, one above and one below the apparatus. In the first section of this chapter, we present a discussion on the measurement technique and a discussion on the fundamental limitations in mass resolution. We describe the overall system hardware configuration in the second section. The construction of the NaI stack and some of the stack's ΔE and position measuring capabilities is discussed in section 3. In the fourth section, we will present discussions on the plastic scintillators and the Cerenkov counters. The different contributions to the mass resolution will be discussed in the final section of this chapter.

2.1. Measurement Technique

When a particle of charge Z, mass number A, and total energy E passes through matter, it loses energy predominantly by means of collisions with atomic electrons in the medium. Some materials have characteristics that allow the measurement of the energy deposition by such methods as the collection of scintillation light, the collection of electron-hole pairs, etc. In general, the energy depostion is not identically the same as the energy loss in the medium. However, in some cases, the energy deposition can be considered as a reasonable approximation to the energy loss. If in addition to the energy loss, a velocity-related parameter is measured before and after the charged particle's encounter with the energy absorbing medium, the mass of the particle can be deduced. One such parameter is the Lorentz factor, γ, in the energy-mass equivalence relation

$$E = \gamma Mc^2 \tag{2.1}$$

where M is the mass of the particle, $\gamma = (1-\beta)^{-1/2}$, β is the velocity of the particle divided by the speed of light (i.e., $\beta = v/c$), and c is the speed of light. Figure 2.1 illustrates the geometry of the measurement.

In this scheme, there are three measured quantities :

γ_1	the Lorentz factor of the particle prior to the penetration,
γ_2	the Lorentz factor of the particle after the penetration; if the particle stops in the medium, $\gamma_2 = 1$,
ΔE_d	the energy deposition of the particle in the medium; we will assume here that $\Delta E = \Delta E_d$, where ΔE is the energy loss of the particle in the medium.

With γ_1, γ_2 and equation (2.1), we obtain

$$E_1 = \gamma_1 Mc^2 \qquad \text{and} \qquad E_2 = \gamma_2 Mc^2 \tag{2.2}$$

Now, the energy loss in medium is given by

$$\Delta E = E_1 - E_2 = (\gamma_1 - \gamma_2)Mc^2 = \Delta\gamma \cdot Mc^2. \tag{2.3}$$

The only unknown in equation (2.3) is the mass M. Therefore, the mass can be deduced from equation (2.3) by solving for M.

Before continuing on to the discussion of mass resolution, we will put things in terms of the particle's atomic mass number, A, instead of the absolute mass, M. The mass of the particle can be expressed as

Figure 2.1

Schematic illustration of geometry for Cerenkov-ΔE-Cerenkov measurement of particle mass. If particle stops in the medium, $\gamma_2 = 1$.

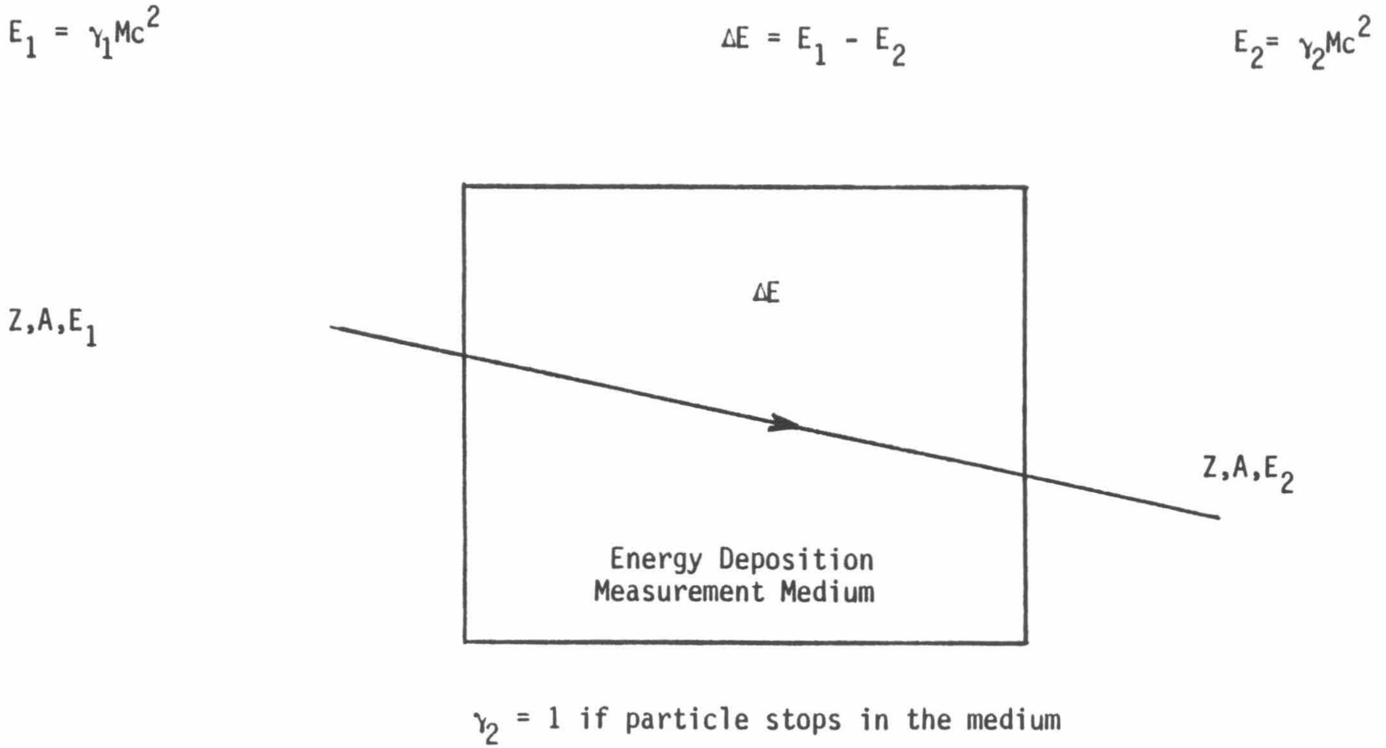
$E_1 = \gamma_1 Mc^2$
$\Delta E = E_1 - E_2$
$E_2 = \gamma_2 Mc^2$
ΔE
Z, A, E_1
Z, A, E_2
Energy Deposition
Measurement Medium
$\gamma_2 = 1$ if particle stops in the medium

$$M = Z \cdot M_p + (A - Z)M_n - E_b / c^2. \tag{2.4}$$

where $M_p = 938.28$ MeV/ c^2 and $M_n = 939.57$ MeV/ c^2 are the proton and neutron masses respectively, and E_b is the nuclear binding energy of the particle. For particles we are interested in ($10 \leq Z \leq 28$), E_b is about 8 MeV/nucleon. Equation (2.4) can be approximated as

$$M \simeq A \cdot M_a \tag{2.4'}$$

where $M_a = 931.50$ MeV/ c^2 is the mass per atomic mass unit. Combining equations (2.3) and (2.4'),

$$A \simeq \frac{\Delta E}{M_a c^2 \cdot \Delta\gamma}. \tag{2.5}$$

Equation (2.5) shows that the determination of mass number A depends on the measurements of ΔE and $\Delta\gamma$. Differentiating equation (2.5) gives

$$\frac{\delta A}{A} \simeq \frac{\delta \Delta E}{\Delta E}. \quad \text{and} \quad \frac{\delta A}{A} \simeq \frac{\delta \Delta\gamma}{\Delta\gamma} \tag{2.6}$$

Thus, for example, if one wants 0.1 a.m.u. resolution for iron isotopes ($A \simeq 56$), one must measure both ΔE and $\Delta\gamma$ to better than 0.2%.

The uncertainties in the ΔE and $\Delta\gamma$ measurements have many contributing factors. Some of these contributions are intrinsic to the detector system and will pose fundamental physical limitations on system performance. These limitations cannot be reduced without altering system design. For example, Cerenkov radiation and scintillation light are usually observed using photomultipliers, and statistical fluctuations in the number of photoelectrons produced in the photomultipliers is one such contribution. Other contributions are not intrinsic, but they are results of technical imperfections. For example, thickness variations in the detectors is one such contribution. Imperfect correction for variations in detector response with position introduces another such contribution. In designing an instrument, one would like to reduce uncertainties due to technical imperfections so that these uncertainties are small compare to the fundamental physical limitations on the system.

In this section, we will discuss the physical limitations on the mass resolution. The technical limitations will be discussed in the later sections. Since the ΔE and $\Delta\gamma$ measurements are done independently, the mass resolution contribution due to their uncertainties are independent of each other. Therefore, we will discuss the two contributions separately.

First, we will present an analysis of the physical limitations for the ΔE measurement. As we will show later, it is possible to achieve a few tenths of a percent accuracy in the ΔE measurement. For ΔE of the order of GeV/nucleon, NaI scintillators can be used to measure the energy loss. The photoelectron statistical fluctuation will be a fundamental limitation on this measurement. The number of photoelectrons, N_{PE}, is given by

$$N_{PE} = (\Delta E/\overline{h\nu})\cdot\varepsilon\cdot F_s\cdot G\cdot K. \tag{2.7}$$

In this expression,

ΔE is the energy loss,

$\overline{h\nu}$ is the average energy of the scintillation photons,

ε is the scintillation efficiency of the crystal for relativistic $Z = 1$ particles,

F_s is the light conversion saturation factor, $F_s = 1$ for relativistic $Z = 1$ particle and $F_s < 1$ for heavy ions,

G is the geometric light collection efficiency, i.e., the fraction of scintillation light seen by photomultipliers, K is the photocathode quantum efficiency.

For NaI, the average wavelength of the scintillation light is around 400 nm (i.e., $\overline{h\nu} = 3.1\mathrm{eV}$), and the scintillation efficiency is about 15% (Harshaw Scintillation Phosphors, 3rd Edition). According to Salamon et al. 1981, F_s of NaI can become quite low just before the charged particle stops because of the higher value in dE/dx. However, if we average F_s over a thickness of more than 10 gm/cm^2 of NaI, the average value of F_s does not go below 0.4 even for iron (Z = 26) nuclei. A light collection system with a geometric light collection efficiency of a few percent can easily be constructed. The photocathode quantum efficiency ranges from 20% to 25% for typical photomultipliers. Now, if we take $\Delta E = 50\mathrm{GeV}$, $h\nu = 3.1\mathrm{eV}$, $\varepsilon = 0.15$, $F_s = 0.4$, $G = 0.02$, and $K = 0.20$, then we will get about $4 \cdot 10^6$ photoelectrons and a photoelectron statistical fluctuation of ~0.05%. Therefore, the photoelectron statistical fluctuations in the ΔE measurement do not put a significant limitation on the mass resolution.

Landau fluctuations in the energy loss also contribute to the mass uncertainty. For example, in the ΔE-E' method (see Stone 1974), it is required to have a knowledge of the rate of energy loss, dE/dx, as a function of energy (or the range-energy relationship). Such knowledge can be obtained either empirically by experiment, or from tabulated tables (such as Barkas and Berger, 1964; Janni, 1966). However, due to the statistical nature of the ionization energy loss process, knowledge of dE/dx can only be obtained for an average over many particles of the same charge and same mass. In our present scheme, knowledge of dE/dx is not required for deducing the mass. Therefore, the Landau fluctuations do not have a direct contribution to the mass uncertainty in this case. However, as we will show later, Landau fluctuations will have an indirect contribution to the mass uncertainty through the $\Delta\gamma$ determination.

We have shown that physical limitations of the ΔE measurement do not put any significant limit on the mass resolution. However, the $\Delta\gamma$ measurement is a more difficult one. The Lorentz factors, γ_1 and γ_2, can be measured by Cerenkov counters. Now since γ_1 and γ_2 are measured independently, we have

$$(\delta\Delta\gamma)^2 = (\delta\gamma_1)^2 + (\delta\gamma_2)^2 \tag{2.8}$$

When a particle travels at a velocity greater than that of light in the medium, it will generate electromagnetic radiation (see page 638 of Jackson 1975). This is called Cerenkov radiation. The strength of the Cerenkov signal, C, is given by

$$C \propto Z^2 \left\{ 1 - \frac{1}{n^2\beta^2} \right\} \tag{2.9}$$

where n is the index of refraction of the medium, and β is the velocity of the particle divided by the velocity of light. Now, define f to be the ratio of the Cerenkov light generated at velocity β to that generated by relativistic ($\beta=1$) particles,

$$f(\beta) = \frac{1 - \dfrac{1}{n^2\beta^2}}{1 - \dfrac{1}{n^2}} \tag{2.10}$$

or

$$f(\gamma) = \frac{n^2(\gamma^2-1) - \gamma^2}{(\gamma^2-1)(n^2-1)}. \tag{2.10$'$}$$

Figure 2.2 shows $f(\gamma)$ for different indices of refraction. How well we can measure γ depends both on how well we can measure f and the value of $df/d\gamma$. For an accurate γ measurement, we should restrict γ to be near the

Figure 2.2

A plot of the fraction, f, of relativistic Cerenkov light made by particles of Lorentz factor γ incident on Cerenkov media of various indices of refraction n. The slope $df/d\gamma$ evaluated at $f = 0$ (Cerenkov threshold) is simply $2n^2\sqrt{1-1/n^2}$. This plot ignores scintillation and delta-ray contributions to the light, which are likely to be important below $f \simeq 0.05$.

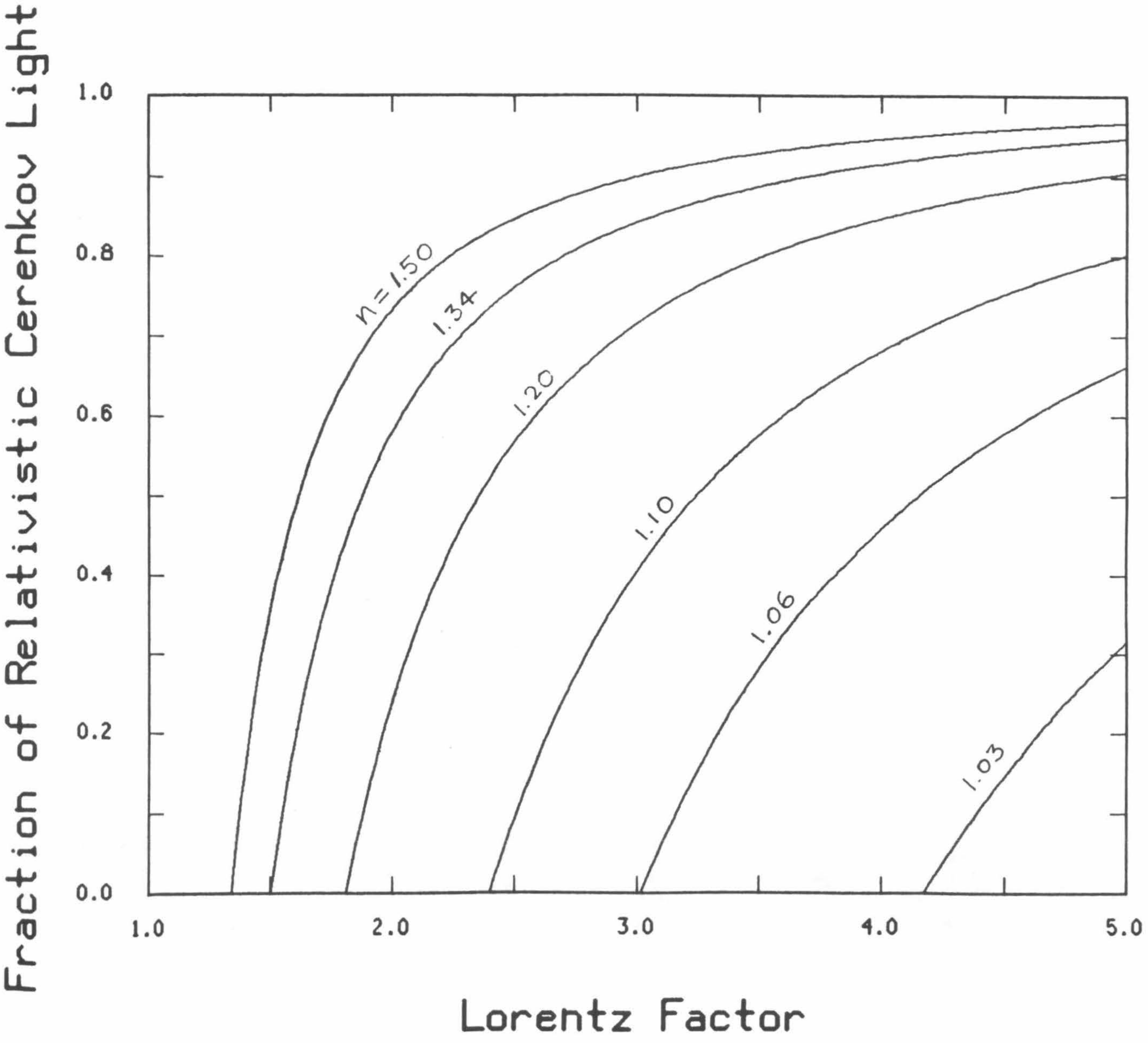
Fraction of Relativistic Cerenkov Light
1.0
0.8
0.6
0.4
0.2
0.0
1.0
2.0
3.0
4.0
5.0
Lorentz Factor
n=1.50
1.34
1.20
1.10
1.06
1.03

threshold where the slope of f is reasonably steep.

The number of photoelectrons detected by the Cererkov counter system, $N_{PE,C}$, is

$$N_{PE,C} = Z^2 \cdot N_{rel} \cdot f \tag{2.11}$$

where N_{rel} is the number of photoelectrons that would be detected for a relativistic $Z = 1$ particle. Taking the differentials of both sides, we get

$$\begin{aligned} \delta N_{PE,C} &= Z^2 \cdot N_{rel} \cdot \delta f \\ &= Z^2 \cdot N_{rel} \cdot \frac{df}{d\gamma} \cdot \delta\gamma. \end{aligned} \tag{2.12}$$

The photoelectron statistical fluctuation is just the square root of $N_{PE,C}$, and $df/d\gamma$ can be obtained by differentiating equation (2.10′)

$$\frac{df}{d\gamma} = \frac{2\gamma}{(n^2-1)(\gamma^2-1)^2} \tag{2.13}$$

Combining these and equation (2.12), we get

$$(\delta\gamma)^2 = \frac{(n^2-1)(\gamma^2-1)^3}{4 \cdot Z^2 \cdot \gamma^2 \cdot N_{rel}} \left[(n^2-1)\gamma^2 - n^2\right]. \tag{2.14}$$

Substituting n_1, $N_{rel,1}$, γ_1 into equation (2.14) to get $(\delta\gamma_1)^2$ and n_2, $N_{rel,2}$, γ_2 to get $(\delta\gamma_2)^2$, equation (2.8) gives

$$\begin{aligned} \delta\Delta\gamma_{PE} = \frac{1}{2Z} \Bigg\{ & \frac{(n_1^2-1)(\gamma_1^2-1)^3}{\gamma_1^2 \cdot N_{rel,1}} \left[(n_1^2-1)\gamma_1^2 - n_1^2\right] \\ & + \frac{(n_2^2-1)(\gamma_2^2-1)^3}{\gamma_2^2 \cdot N_{rel,2}} \left[(n_2^2-1)\gamma_2^2 - n_2^2\right] \Bigg\}^{1/2}. \end{aligned} \tag{2.15}$$

The mass uncertainty due to the Cerenkov photoelectron statistical fluctuations is

$$\delta A_{PE,C} = A \cdot \delta\Delta\gamma_{PE} / \Delta\gamma \tag{2.16}$$

where $\delta\Delta\gamma_{PE}$ is given by equation (2.15) above. At first glance, $\delta A_{PE,C}$ doesn't seem to have any Z dependence for A = 2Z particles. However, both γ_2 and $\Delta\gamma$ do depend on Z. The mass uncertainty should be smaller for higher Z because $\Delta\gamma$ is larger for higher charge particles. Also, γ_2 will be smaller for higher charge particles and thus a higher $df/d\gamma$ will result.

With a certain given detector configuration (i.e., fix n_1, n_2, and thickness of the ΔE detector), the mass uncertainty depends on the energy of the incident particle and the angle of incidence. The mass uncertainty also has a secondary dependence on the charge as discussed in the previous paragraph. The energy dependence is clearly shown in equation (2.15) in terms of γ_1 and γ_2. The angular dependence comes into play through two contributions. First, both $N_{rel,1}$ and $N_{rel,2}$ have a $\sec\vartheta$ dependence where ϑ is the angle of incidence of the particle. Secondly, the path length in the ΔE detector also goes like $\sec\vartheta$. As a result, a larger ϑ will cause a larger $\Delta\gamma$ and a smaller γ_2. All of these point to better mass resolution (i.e., smaller δA) as ϑ increases.

It is difficult to show all the dependences of the mass uncertainty at the same time. Figure 2.3 shows the energy dependence of the mass uncertainty due to the γ_1 measurement alone. The curve in figure 2.3 is applicable for all A = 2Z particles. Note that this is exactly $\delta A_{PE,C}$ for particles stopping in the ΔE detector. If the particle penetrates the ΔE detector, we can still use this curve to estimate $\delta A_{PE,C}$ as long as the γ_2 contribution in equation (2.15) is small compared to the γ_1 contribution. In this case, a very good approximation can be obtained by scaling the curve with $(\gamma_1-1)/(\gamma_1-\gamma_2)$.

What if the particle penetrates the ΔE detector but γ_2 is lower than the Cerenkov threshold of the second Cerenkov counter? There are two

Figure 2.3

A plot of the mass uncertainty due to the Cerenkov photoelectron statistical fluctuations, $\delta A_{PE,C}$, for A = 2Z particles with Lorentz factor γ incident on Cerenkov media with $n = 1.10$ and $N_{rel,1} = 30$. The plot shows only the mass uncertainty contribution from the first Cerenkov counter for normally incident particles (i.e., $\vartheta = 0$). For ϑ other than 0, scale the curve by $\cos^{1/2}\vartheta$. For $N_{rel,1}$ other than 30, scale the curve by $\sqrt{30/N_{rel,1}}$.

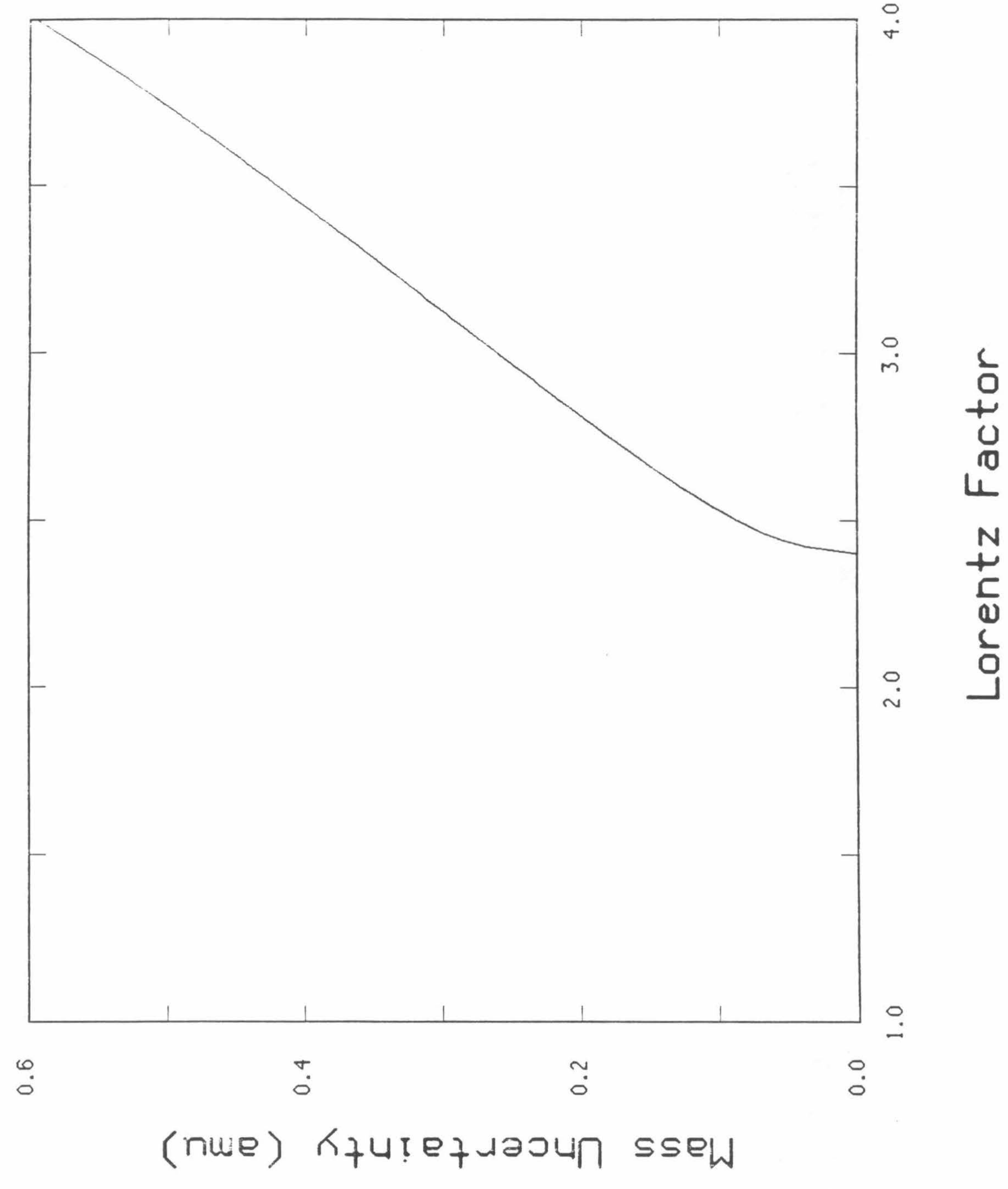
Mass Uncertainty (amu)
0.0
0.2
0.4
0.6
Lorentz Factor
1.0
2.0
3.0
4.0

possibilities. If the particle penetrates the second Cerenkov counter, the missing ΔE can be as high as 320 MeV/nucleon for $n_2 = 1.50$. However, we can utilize an anti-coincidence scintillator in the back of the second Cerenkov counter to reject these events. On the other hand, if the particle stops in the second Cerenkov counter, there is almost nothing we can do. This is because we do not have an easy way to distinguish these events from the ones which stop in the ΔE detector. We could introduce a thin anti-coincidence scintillator between the ΔE detector and the second Cerenkov counter to reject these events. Otherwise, we will have a low mass tail for each of the isotope peaks in a mass histogram. Because of the higher dE/dx just before the particle stops, the fraction of the ΔE missing can be a few times the ratio of the equivalent thickness of the second Cerenkov counter to that of the ΔE detector. Now, if we have about 100 g/cm^2 of NaI for the ΔE detector and about 2 g/cm^2 of NaI equivalent for the second Cerenkov counter, the missing ΔE can be as high as 6%. From equation (2.5), the mass is proportional to ΔE; therefore the tail can extend all the way to 6% lower than the real mass. The fraction of events contributing to the tails is approximately equal to the ratio of stopping powers mentioned above. This fraction will go higher if we only accept events which penetrate at least a certain fraction of the ΔE detector. We have eliminated the problem, at the cost of somewhat reduced energy coverage, by using a segmented ΔE counter.

In the discussion of the $\Delta\gamma$ measurement, we have only talked about the photoelectron statistical fluctuations. So far, we have assumed that we have knowledge of the incident angle, ϑ, and the charge of the particle. The charge of the particle can be obtained by using a multi-element detector system for the ΔE measurement. Since the charge Z is discrete, we can assume that there is no uncertainty in Z. The incident angle can be measured by using more than one position measuring device. Rewriting equation (2.11) to show the ϑ dependence, we get

$$N_{PE,C} = Z^2 \cdot N_{rel,0} \cdot \sec\vartheta \cdot f \tag{2.17}$$

or

$$f = \frac{N_{PE,C}}{Z^2 \cdot N_{rel,0}} \cos\vartheta \tag{2.17'}$$

where $N_{rel,0}$ is N_{rel} for $\vartheta = 0$. Taking the differentials of both sides, we get

$$\delta f = \frac{df}{d\gamma} \cdot \delta\gamma = -\frac{N_{PE,C}}{Z^2 \cdot N_{rel,0}} \sin\vartheta \cdot \delta\vartheta$$

$$= -\sec\vartheta \cdot f \cdot \sin\vartheta \cdot \delta\vartheta = -f \cdot \tan\vartheta \cdot \delta\vartheta. \tag{2.18}$$

Substituting equation (2.13) for $df/d\gamma$ and equation (2.10') for f, equation (2.6) gives

$$\delta A_{\vartheta,C} = \frac{A \cdot (\gamma+1)}{2\gamma} \left[n^2(\gamma^2-1) - \gamma^2\right] \cdot \tan\vartheta \cdot \delta\vartheta \tag{2.19}$$

for stopping particles. Equation (2.19) shows that $\delta A_{\vartheta,C}$ goes linearly in A and has a $\tan\vartheta$ dependence. The mass is more uncertain for increasing A and increasing ϑ. We will plug some numbers in equation (2.19) to see whether a reasonable mass resolution can be achieved. For $n = 1.10$, $\gamma = 3.0$, $A = 50$, $\delta A_{\vartheta,C}$ is equal to $23 \cdot \tan\vartheta \cdot \delta\vartheta$. This says that even with an angular resolution of the order of a degree (i.e., $\delta\vartheta = 0.02$), we still will not be able to obtain a good mass resolution for ϑ greater than 30°. Figure 2.4 shows a plot of equation (2.19) for $A = 50$ and $\delta\vartheta = 0.02$. The plot shows that even for $A = 50$, this contribution to the mass uncertainty is comparable to or greater than the photoelectron statistical fluctuation contribution for most

Figure 2.4

A plot of the angular uncertainty contribution to the mass uncertainty, $\delta A_{\vartheta,C}$, for a particle with mass A = 50, and several incident angles ϑ. The index of refraction of the Cerenkov radiator is 1.10 and the angular uncertainty is taken to be 0.02 rad. The solid curves scale linearly with the mass, A. The dashed line is the photoelectron statistical fluctuation contribution from figure 2.3.

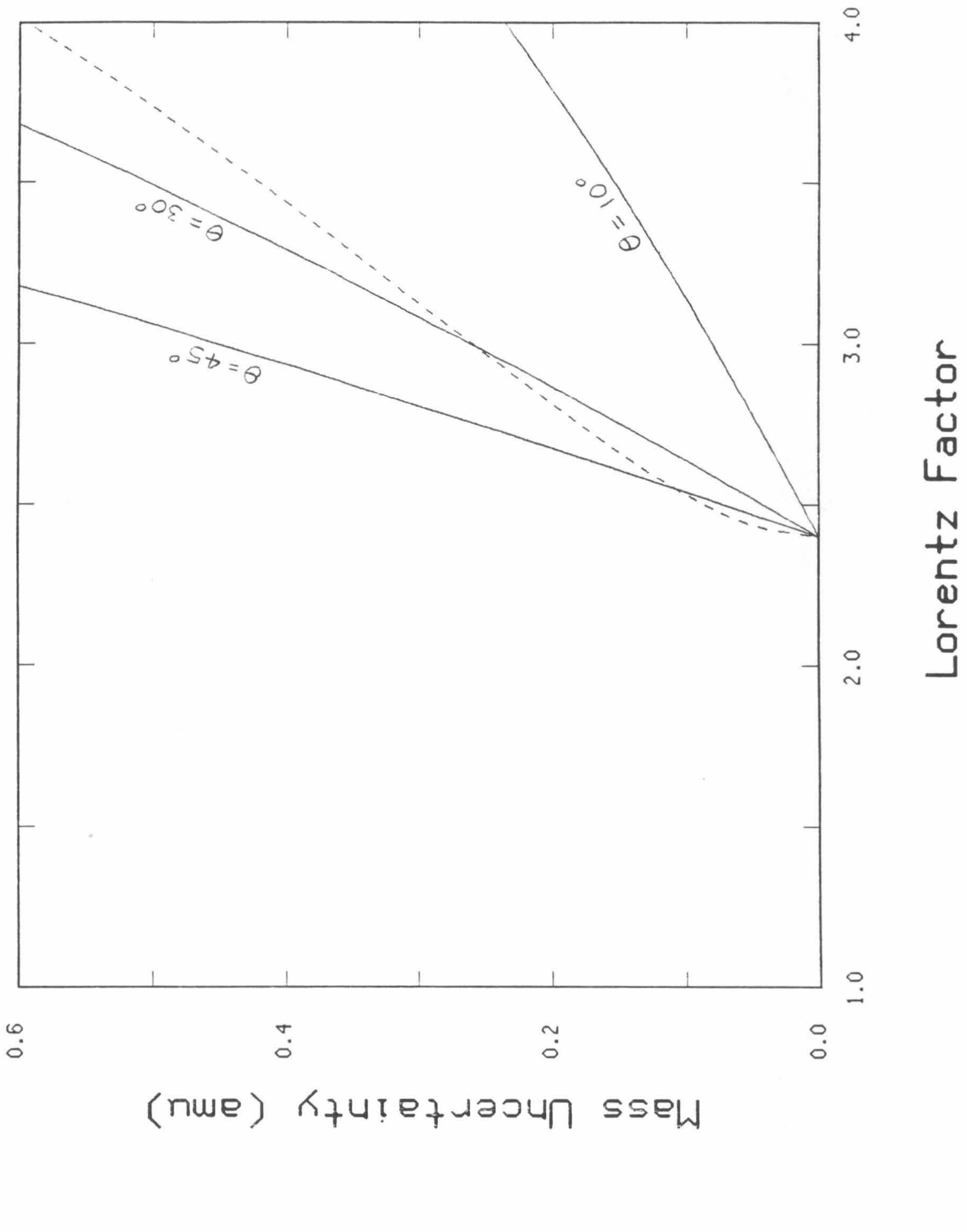
Mass Uncertainty (amu)
0.6
0.4
0.2
0.0
Lorentz Factor
1.0
2.0
3.0
4.0
θ = 10°
θ = 30°
θ = 45°

of the incident angles.

Fortunately, there is a way to go around this obstacle. Using a multi-element detector system for the ΔE measurement, we can deduce γ from the ratio of the Cerenkov signal to the response in the adjacent ΔE measuring element. Since both responses increase as the secant of the incident angle, we have eliminated the need for pathlength corrections in determining γ. The Cerenkov response can be written as

$$C = \alpha_1 \cdot \frac{Z^2}{\beta^2} \cdot \sec\vartheta \cdot \left[1 - \frac{1}{\gamma^2} - \frac{1}{n^2}\right] \tag{2.20}$$

and the response in the adjacent ΔE measuring element is approximately given by

$$S = \alpha_2 \cdot \frac{Z^2}{\beta^2} \cdot \sec\vartheta \tag{2.21}$$

where α_1 and α_2 are just proportionality constants. Here, we have ignored the relativistic rise factor, $\left[\ln(\gamma^2 \cdot \beta^2) - \beta^2 + \kappa\right]$, in the energy loss equation (see Janni, 1966). Taking the ratio of the two responses, we get

$$R \equiv \frac{C}{S} = \frac{\alpha_1}{\alpha_2} \cdot \left[1 - \frac{1}{\gamma^2} - \frac{1}{n^2}\right] \tag{2.22}$$

and thus,

$$\frac{1}{\gamma^2} = 1 - \frac{1}{n^2} - R \cdot \frac{\alpha_2}{\alpha_1}. \tag{2.23}$$

With this *scheme*, then, γ is determined directly without ever having to get involved with trajectory measurements except, of course, for correcting spatial nonuniformities of the Cerenkov and scintillator responses. Since S is in the ratio R, Landau fluctuations in S contribute to the uncertainty in γ. Taking the differentials of both sides of equation (2.23), we get

$$-\frac{2\delta\gamma}{\gamma^3} = -\delta R\cdot\frac{\alpha_2}{\alpha_1} \tag{2.24}$$

or

$$\delta\gamma = -\gamma^3\cdot\frac{\alpha_2}{2\alpha_1}\cdot R\cdot\frac{\delta S}{S} = -\frac{\gamma^3}{2}\cdot\left[1-\frac{1}{\gamma^2}-\frac{1}{n^2}\right]\cdot\frac{\delta S}{S} \tag{2.25}$$

where δS is the Landau fluctuation. We have parametrized the treatment in Rossi's "High Energy Particles", pages 32 throught 35, to an accuracy of about 1%. A 2 cm thick slab of NaI has $\alpha_2 \simeq 10$ MeV and a characteristic fluctuation size that drops from about 1.4 Z MeV at $\gamma = 3$ to about 0.8 Z MeV at $\gamma = 1.5$. For particles with $Z \geq 10$, the distribution shape is nearly gaussian. Taking the fluctuation size to be $\alpha_3\cdot Z\cdot\sec^{½}\vartheta$, equation (2.25) gives

$$\delta\gamma = -\frac{\gamma^3\cdot\beta^2}{2Z\cdot\sec^{½}\vartheta}\cdot\frac{\alpha_3}{\alpha_2}\cdot\left[1-\frac{1}{\gamma^2}-\frac{1}{n^2}\right]. \tag{2.26}$$

Both $\delta\gamma_1$ and $\delta\gamma_2$ can be obtained from equation (2.26); substituting them back in equation (2.8), we get

$$\delta\Delta\gamma_L = \frac{\cos^{½}\vartheta}{2Z}\cdot\frac{\alpha_3}{\alpha_2}\cdot\left\{\gamma_1^6\cdot\beta_1^4\cdot\left[1-\frac{1}{\gamma_1^2}-\frac{1}{n_1^2}\right]^2 + \gamma_2^6\cdot\beta_2^4\cdot\left[1-\frac{1}{\gamma_2^2}-\frac{1}{n_2^2}\right]^2\right\}^{½}. \tag{2.27}$$

Here we have assumed that the characteristics (i.e., α_2 and α_3) of the adjacent ΔE measuring element for the second Cerenkov counter are the same as those for the first Cerenkov counter. The mass uncertainty due to Landau fluctuations is

$$\delta A_{L,C} = A\cdot\delta\Delta\gamma_L / \Delta\gamma \tag{2.28}$$

where $\delta\Delta\gamma_L$ is given by equation (2.27) above. Figure 2.5 shows the Landau fluctuation contribution to the mass uncertainty due to the first Cerenkov counter alone. The curve is for normally incident $A = 2Z$ particles. For particles with non-zero incident angle, the Laudau fluctuation contribution will

Figure 2.5

A plot of the Landau fluctuation contribution to the mass uncertainty, $\delta A_{L,C}$, for normally incident A = 2Z particles with Lorentz factor γ. The plot shows only the contribution from the first Cerenkov counter. It assumes the adjacent ΔE measuring element to be a 2 cm thick slab of NaI which has $\alpha_2 \simeq 10$ MeV and a characteristic fluctuation size that drops from about 1.4 Z MeV at $\gamma = 3$ to about 0.8 Z MeV at $\gamma = 1.5$. The dashed line is the photoelectron statistical fluctuation contribution from figure 2.3.

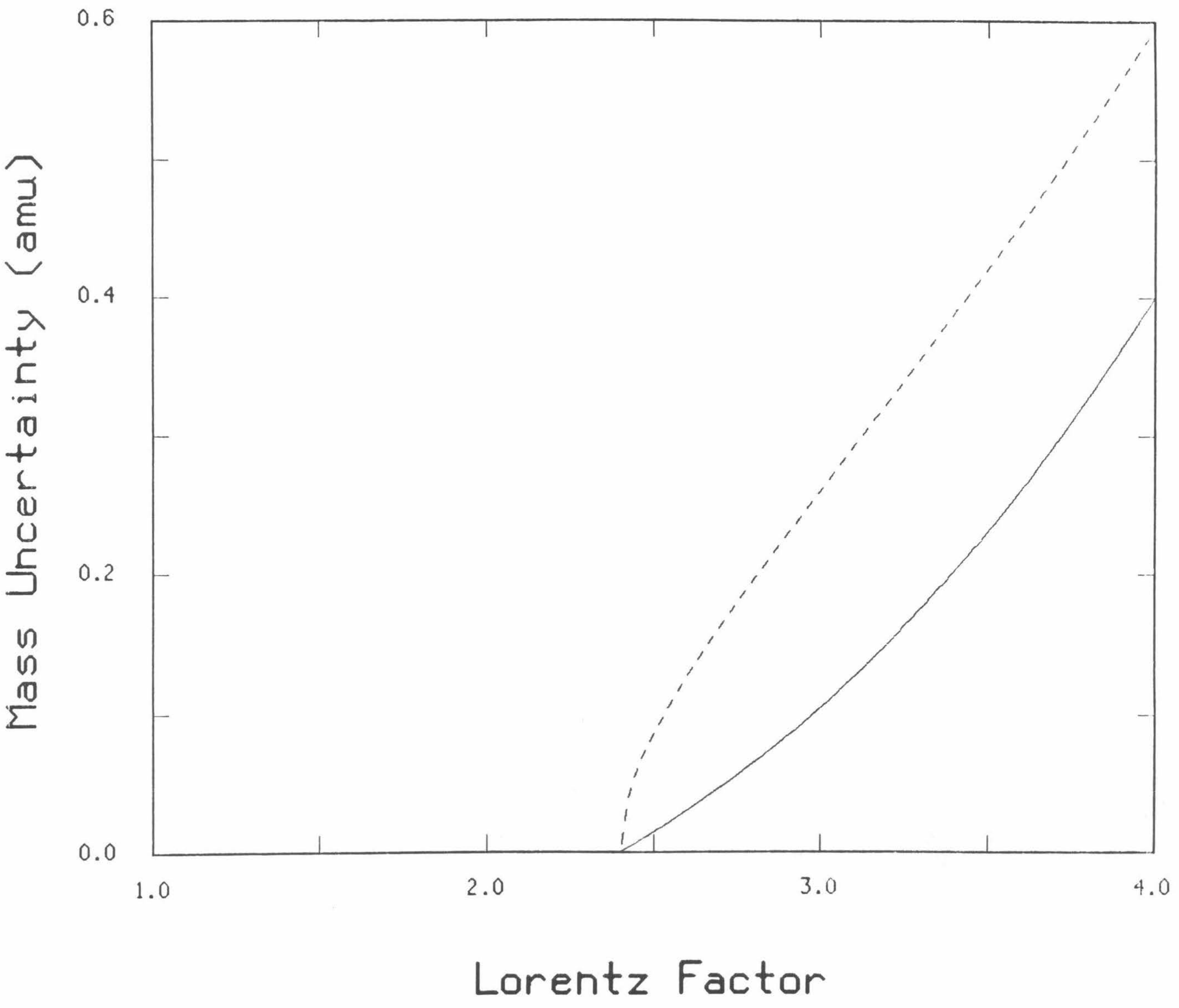
Mass Uncertainty (amu)
0.6
0.4
0.2
0.0
1.0
2.0
3.0
4.0
Lorentz Factor

be smaller by a factor of $\cos^{1/2}\vartheta$.

The mass uncertainty due to the $\Delta\gamma$ measurement is the sum in quadrature of $\delta A_{PE,C}$ (equation 2.16), and $\delta A_{L,C}$ (equation 2.28). Assuming that the uncertainty in the ΔE measurement is small compared to this, this sum represents the full mass uncertainty. Monte Carlo simulations, which are free of the Z^2/β^2 assumption used in equation (2.21), have verified that equation (2.21) is a very good approximation.

The full mass uncertainty should also contain contributions from multiple Coulomb scattering, which causes a different value of $\sec\vartheta$ for the C and the S parts of the ratio $R = C/S$; and from delta-ray production in and near the Cerenkov counters, which causes a departure from the curves in figure 2.2 and introduces additional fluctuations. Both of these extra sources of error are expected to be small compared with the error contributions of equations (2.16) and (2.28).

In this section, we have presented a method of identifying the mass of a charged particle using a Cerenkov-ΔE-Cerenkov analysis. An analysis of the mass uncertainty has shown that the $\Delta\gamma$ measurement is the major contributor to the mass error. To eliminate the need for pathlength corrections in determining γ, we can deduce γ from the ratio of the Cerenkov signal to the response in the adjacent ΔE measuring element. In the next section, we will present an overview of an instrument designed to separate isotopes using the method discussed in this section.

2.2. System Configuration of HEIST

2.2.1. Overview of the Instrument

The High Energy Isotope Spectrometer Telescope is a balloon-borne instrument designed to detect galactic cosmic ray heavy isotopes with mass resolution better than 0.3 a.m.u. for elements from neon through iron. The energy window of the instrument has the Lorentz factor ranging from 2.4 to 3.2. Figure 2.6 shows a cross sectional view of the instrument. A stack of twelve NaI(Tl) discs 52 cm in diameter and a total of 87.2 gm/ cm^2 in thickness provides a direct measurement of ΔE. Each stack layer is viewed by six photomultipliers which are individually digitized. Such an arrangement measures not only the energy deposition, but also the trajectory location in the layer (Buffington, Lau and Schindler, 1981). A direct measurement of ΔE reduces the dependence of the experiment upon accurate trajectory measurements, and independent determinations of response in many stack layers provides a powerful means of removing the numerous fragmenting events within the stack. Plastic scintillators above and below the apparatus provide a means of identifying fragmenting events in the Cerenkov counters. The lower plastic scintillator also identifies penetrating events which are below the bottom Cerenkov cutoff. The refractive indices of the two Cerenkov counters, $n \simeq 1.10$ (aerogel) above and a combination of $n = 1.34$ (teflon) and $n = 1.49$ (Pilot 425) below, fix the range of incident charge Z and Lorentz factor γ to be covered by this experiment.

Descriptions of the detectors will be presented in the succeeding sections. In this section, we will discuss the overall system of HEIST. The HEIST system is constructed from subsystems which interface with each other through minimal number of protocol signals. The major subsystems are : trigger logic, data acquisition and housekeeping, data formatting and

Figure 2.6

Schematic diagram of the instrument (HEIST-2). (a) plastic scintillators; (b) aerogel Cerenkov counter; (c) NaI scintillator stack; (d) bottom Cerenkov counter with Pilot 425 and teflon.

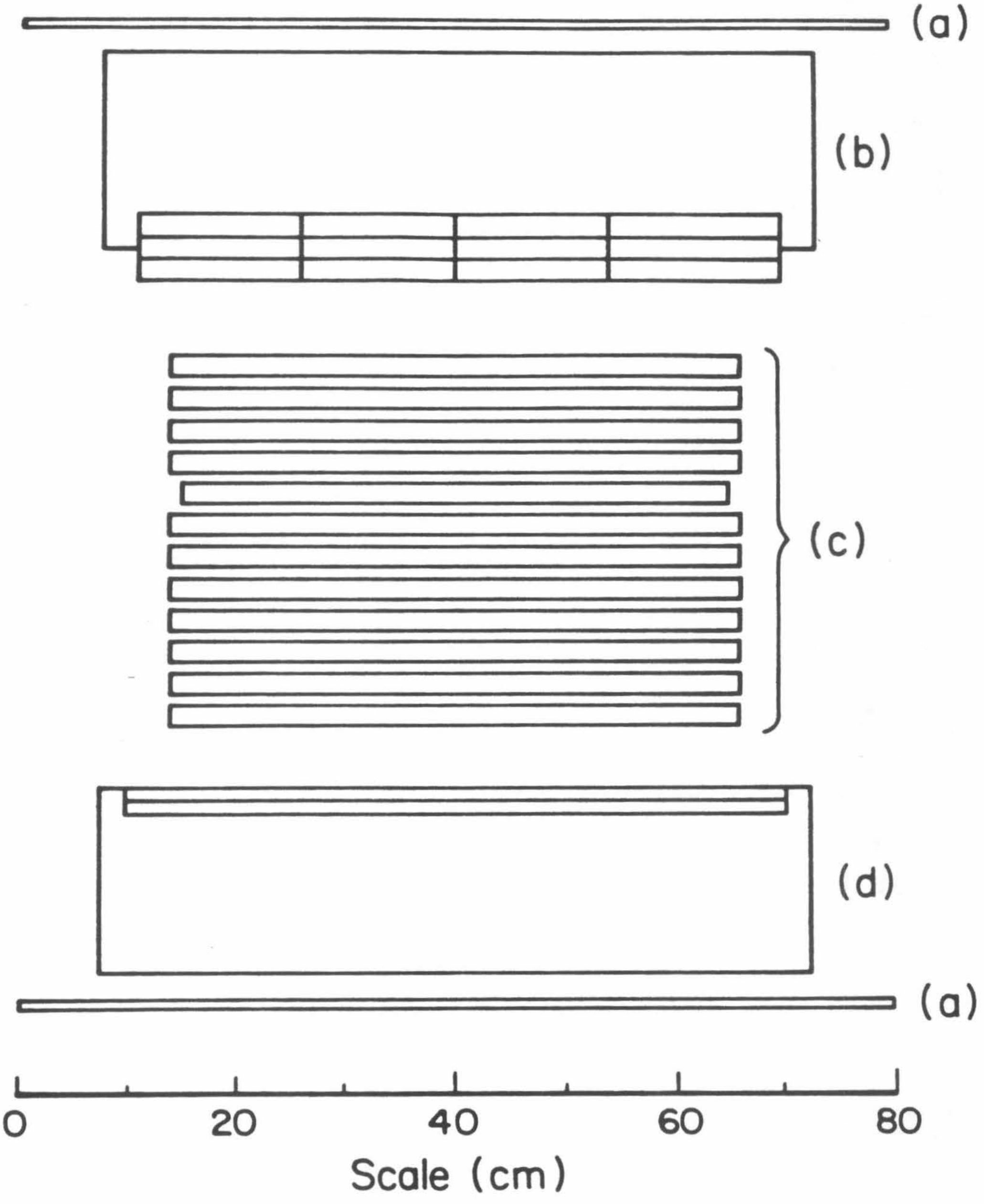
(a)
(b)
(c)
(d)
(a)
0
20
40
60
80
Scale (cm)

recording, high voltage, thermal control, command, and ground support equipment. With the exception of the ground support equipment, the subsystems are all on-board the gondola.

Figure 2.7 shows the configuration of the overall system. The microprocessor in the on-board data acquisition and housekeeping subsystem controls the experiment. It handles all the data i/o, telemetry, and other functions for the system. However, the trigger logic subsystem makes the important decision of what constitutes a valid trigger (i.e., an event of interest). A valid trigger in this experiment is defined as an event which passes through both the top scintillator (S_T) and the fifth layer (L_5) of the NaI stack with energy depositions in these detectors greater than the thresholds. These thresholds are command-adjustable individually. The fifth layer is in the trigger requirement because particles in the desired charge range and energy range do not stop before reaching layer 5.

All of the measurements in this experiment are done with photomultipliers. There are a total of 108 photomultipliers used for the measurements: each of the Cerenkov counters is viewed by twelve 5 inch tubes (EMI 9709) and each of the stack layers and scintillators is viewed by six 1.5 inch tubes (Amperex 2008). All of these 108 tubes are pulse-height-analyzed. For each of the photomultipliers, the anode signal is connected to a charge integration circuit which is followed by a 12-bit (4096 channels) analog-to-digital converter (ADC). Figure 2.8 shows a block diagram of the circuitry. The combined circuitry is designed so that the ADC binning error will be the dominating electronic error contribution. In addition to the anode signal, the last dynode signal is connected to the same circuitry through a pre-ampliflier with a typical gain of 100. The pre-ampliflers are not turned on during normal operation; they are primarily used on muons for system func-

Figure 2.7

Schematic diagram of the overall system configuration of HEIST-2.

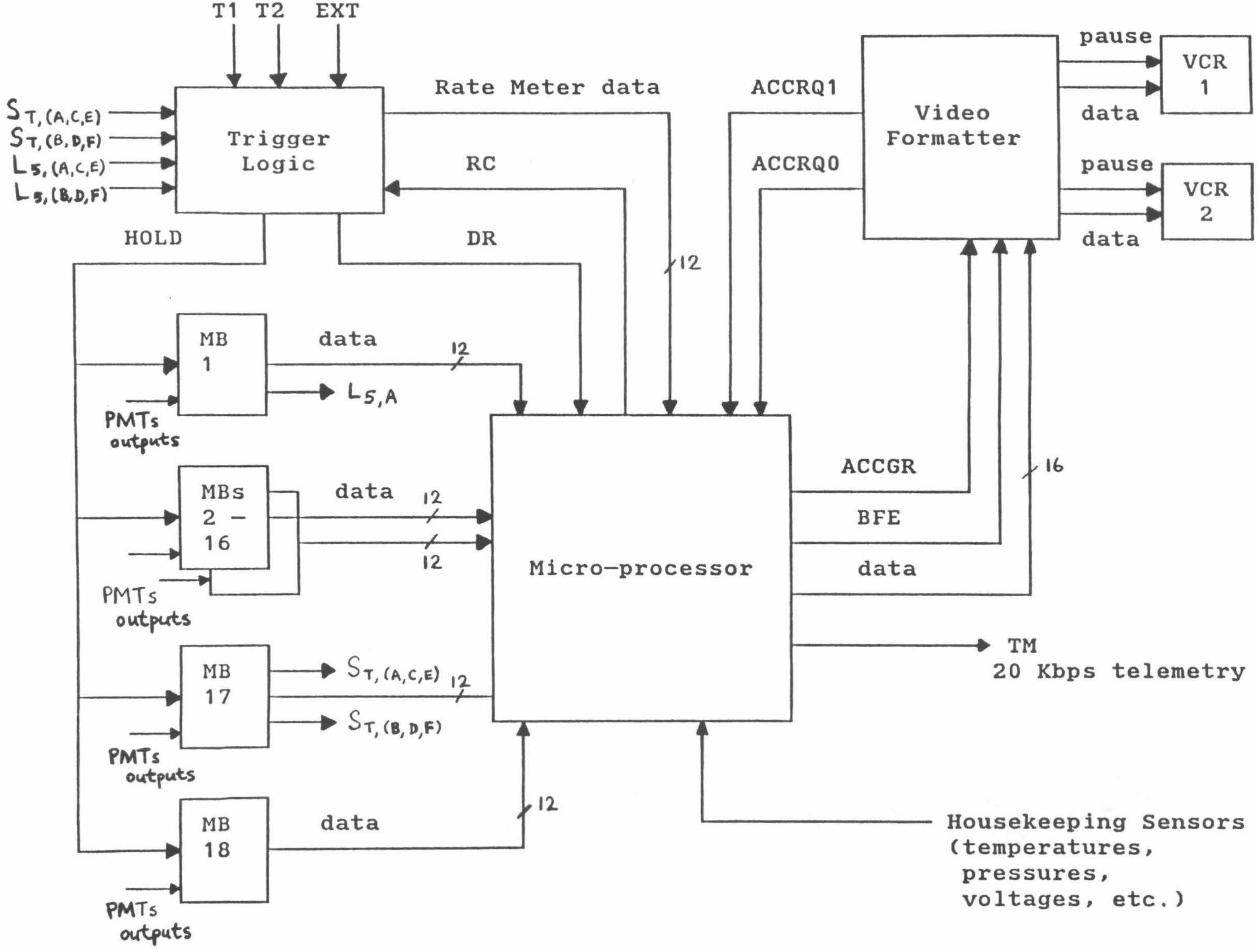
T1
T2
EXT
$S_{T,(A,C,E)}$
$S_{T,(B,D,F)}$
$L_{5,(A,C,E)}$
$L_{5,(B,D,F)}$
Trigger Logic
HOLD
Rate Meter data
RC
DR
12
ACCRQ1
ACCRQ0
Video Formatter
pause
data
VCR 1
pause
data
VCR 2
MB 1
data
12
$L_{5,A}$
PMTs outputs
MBs 2 – 16
data
12
12
PMTs outputs
MB 17
$S_{T,(A,C,E)}$
12
$S_{T,(B,D,F)}$
PMTs outputs
MB 18
data
12
PMTs outputs
Micro-processor
ACCGR
BFE
data
16
TM
20 Kbps telemetry
Housekeeping Sensors (temperatures, pressures, voltages, etc.)

Figure 2.8

Block diagram showing the signal processing circuitry for a photomulitplier.

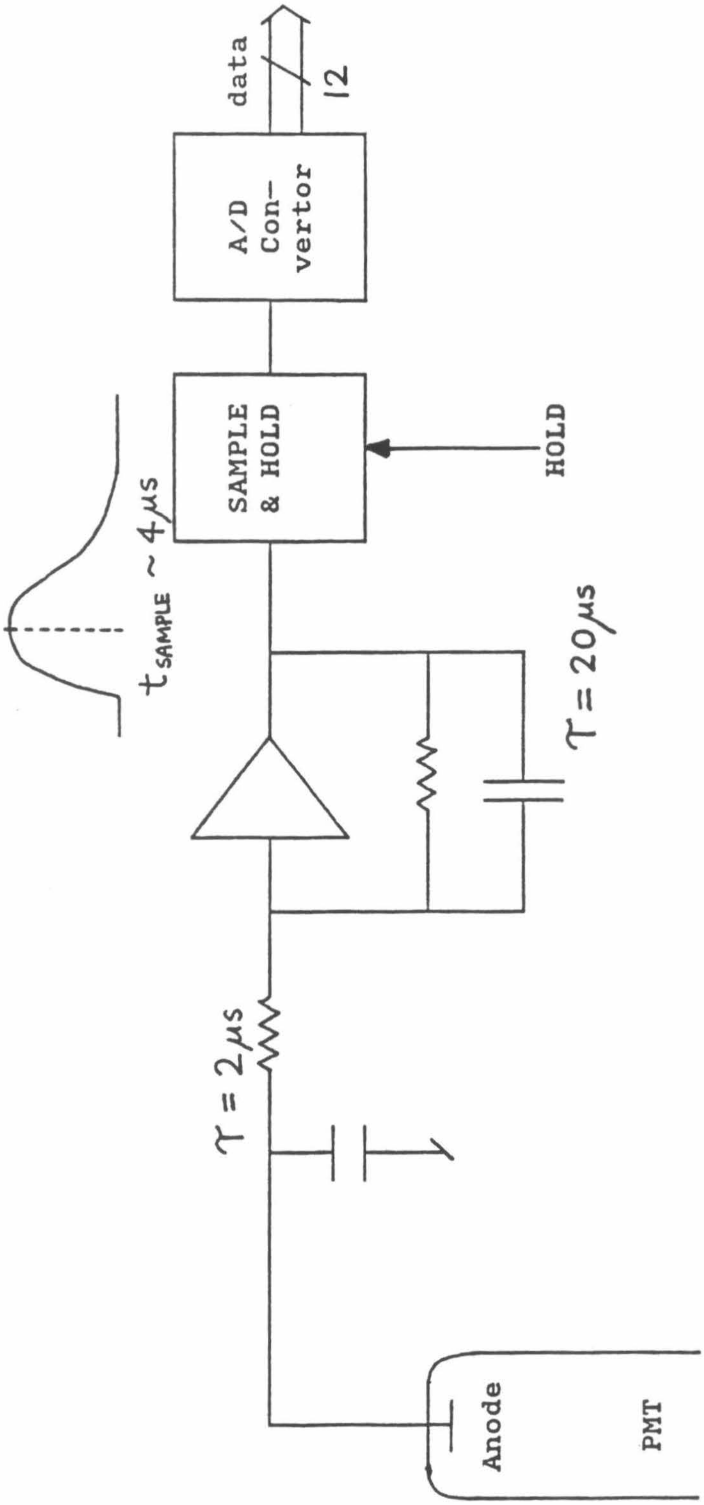
data
12
A/D Con- vertor
SAMPLE & HOLD
HOLD
$t_{SAMPLE} \sim 4\mu s$
$\tau = 20\mu s$
$\tau = 2\mu s$
Anode
PMT

tional checkout and calibration purposes on the ground. The pre-amplifier, charge integration, and ADC circuits are all packaged on a printed-circuit board with dual-inline-packaging so that it looks like a 40-pin IC chip. We call these ADC circuits even though they actually contain more than their name implies. These ADC circuits are plugged onto the 18 motherboards (6 ADC circuits each) which supply the power, control signals, and data readout circuitry. In addition to the 108 photomultipliers mentioned above, there are two photomultipliers (labelled T1, T2) on the top scintillator. These two tubes are used for timing and coincidence purposes only and are not pulse-height-analyzed.

2.2.2. Trigger Logic Subsystem

The trigger logic has two major coincidence requirements: fast coincidence and slow coincidence. The fast coincidence is used to establish the timing of the event and the slow coincidence is used to determine whether the event constitutes a valid trigger. The fast coincidence has three inputs: T1, T2, and EXT. T1 and T2 are the signals from the two timing tubes on the top scintillator. The EXT input is used for generating false triggers to the system. When EXT receives a pulse, the trigger logic will trigger the system regardless of the states of T1, T2, and the slow coincidence. These false triggers are required, and are provided by the ground support equipment when it performs automated calibrations on the electronics. False triggers are also generated by a timer in the trigger logic circuitry at half minute intervals to keep a running record of the system baseline. In addition to these half minute false triggers, the timer also generates false triggers whenever there is no trigger in 1.5 second. This is done to prevent a particular failure mode in the data recording system. All of these false-triggered events are tagged in the data format. The T1 and T2 photomultiplier signals go through two discriminators in the trigger logic. The fast coincidence condition is given by the logic equation EXT+f(T1,T2), where f(T1,T2) is command-programmable to one of the four states: T1, T2, T1+T2, or T1·T2. In the muon mode, the thresholds of the discriminators are set to roughly two-thirds of the most probable response for muons. In the flight mode, the thresholds are set to approximately 20 times the muon mode value so that they will accept all of the incident C, N, O nuclei, but none of the He. When the fast coincidence condition is met, the trigger logic will consider the slow coincidence condition about 4 μs later, which is right before the charge integration peak time. If the slow coincidence is met, the trigger logic will issue a 40 μs HOLD signal to the ADC circuits. Upon receiving the HOLD signal, the outputs of the charge integration circuits will be held (for the length of the HOLD signal) and the analog-to-digital conversion process will begin. The conversion process takes about 35 μs. The leading edge of the HOLD signal is designed to coincide with the peaks of the charge integrated output signals so that error in timing will have the least impact on the pulse height analysis. At the end of this 40 μs, the trigger logic will issue a DR (data ready) signal to the microprocessor, and this signal will stay up until a RC (read complete) signal is sent back by the microprocessor. This reading process takes approximately 15 ms, and the system is dead during this time.

We will now go back to discuss the slow coincidence condition. The slow coincidence is determined from the charge integrated outputs of the 12 photomultipliers from S_T and L_5. The 12 outputs are divided into four groups: $S_{T,A}$, $S_{T,B}$, $L_{5,A}$, and $L_{5,B}$. The 3 outputs in each group are added with an analog summing junction and the sum is fed to a discriminator. The thresholds of the four discriminators are normally set to accept sea-level muons in the muon mode and everything from carbon and up in the flight mode. The thresholds are also command-settable, individually, to one of the eight discrimination levels which span a factor of more than 20 in input signal amplitude. The slow coincidence condition is normally given by the logic equation $S_{T,A} \cdot S_{T,B} \cdot L_{5,A} \cdot L_{5,B}$; however, $S_{T,A}$ and $S_{T,B}$ are both command-removable from the coincidence requirement.

In addition to the coincidence capability, the trigger logic has a rate meter which keeps track of the trigger rates of T1, T2, $S_{T,A}$, $S_{T,B}$, $L_{5,A}$, and $L_{5,B}$. It also has a hazard timer which will tag the current event if another event triggered the system within a 256 μs window before the current trigger.

2.2.3. Data Acquisition and Data Recording Subsystems

The data acquisition subsystem consists of a microprocessor and its resident software. The data acquisition subsystem reads data from the ADC circuits, In addition, it also reads data from many of the housekeeping sensors. There are temperature sensors which monitor temperatures in different locations of the experiment, voltage sensors which monitor system votage supplies, pressure gauges which monitor internal pressure of the gondola, high voltage sensors which monitor voltages going to the NaI stack photomultipliers, and magnetometers which monitor orientation of the experiment with respect to the earth's magnetic field. These housekeeping data are updated for every recorded event and every telemetry frame. The microprocessor also handles the telemetry data stream at about 9 events/sec (~20 kbit/sec). The most current event will be telemetered if there are more than one event since the last telemetered event. On the other hand, if there are no new events, the last event will be telemetered again along with current housekeeping data. The microprocessor has a 50K memory buffer which holds data for 200 events. When this memory buffer is full, the microprocessor will issue a BFE (buffer full/empty) signal to the video formatter and data will be transferred to the video formatter redundantly through two DMA channels. The video formatter puts the data into video format, 16 bits/line and two copies of the same event on a video field, and transfers the formatted data onto two commercial portable video recorders. The two recorders are normally used in parallel and with the data being recorded twice on each recorder, we thus have a four fold redundancy in our data recording. In addition, a checksum is computed and recorded for every data field.

2.2.4. High Voltage Subsystem

High voltage for the 110 photomultipliers is provided by 6 DC-DC high voltage supplies and a high voltage battery-pack. The top and bottom Cerenkov counters use four high voltage supplies. All four supplies are set to have +1550V output. Each supply provides the high voltages for 6 non-adjacent photomultipliers on one counter so that, in the event of a power supply failure, we still have a symmetric measurement. The two supplies for the plastic scintillators are connected with the same philosophy. Each supply provides the high voltages for 3 photomultipliers on the top scintillator, 3 photomultipliers on the bottom scintillator, and one timing tube. These two supplies are set to have -1350V output. The timing tubes are run at -1250V using a resistive voltage divider. Noise measurements and other documentation on the high voltage supplies can be found in the *On-board HV Supply* folder. High voltage distribution information can be found in the *Cerenkov PM Base Design* and *Scintillator PM Base Design* folders.

The 72 stack photomultipliers get their high voltages from the high voltage battery-pack. The pack consists of 800 silver oxide batteries (Eveready 384) in series. These batteries are the same as the ones used in digital wrist watches. They were chosen because of their good discharge characteristic which provides relatively constant voltage throughout the last two-thirds of their life time. The Eveready 384 was chosen because its current capability matches the needs of our application. These batteries have a life time of ~35 mA-hr. The voltage of these batteries decreases throughout roughly the first third of their life time and reaches a plateau value in ~12 mA-hr. Therefore, to minimize the voltage variation in the pack, the batteries were pre-discharged to 13 mA-hr prior to connection to the system. The pack is organized into eight 160V packs, and each of these has twenty 8V sticks. These 8V sticks are considered to be the basic units of the pack. They are constructed from five 1.6V cells spot-welded together in series and wrapped together with low-temperature shrink-tubing. Each stick has two terminals for electrical connections. Twenty of these sticks are wired to a 24-pin connector (Amphenol 67-02E18-24) to form a 160V pack. Each 160V pack is wrapped with low-temperature shrink-tubing with the connector at one end of the one meter long pack. The 24-pin connector carries the 21 voltages of the 20 sticks with 3 pins unused. The eight 160V packs are connected to a high voltage distribution box. They are connected so that three packs provide voltages up to +480V and the other five packs provide voltages down to -800V. The distribution box has thirteen 104-pin connectors (Amphenol 201037). These thirteen connectors are bussed together with twelve of them used for connections to the photomultipliers and the remaining one for connections to external high voltage power supplies. The external connector is used for non-battery operation and during the battery connecting procedures. Due to the system electrical capacitances, the system has to be charged up using external power supplies through this external connector prior to battery-pack connection. There are high-voltage monitors connected to the -800V and +248V points of the high voltage distribution box. Documentation on the pin assignments of connectors, battery-pack connection procedures, and the high voltage monitors, can be found in the *Stack High Voltage* folder.

We procured 100 Amperex 2008 tubes for use on the stack and the two plastic scintillators. Extensive testing was done on 12 sample tubes before this procurement. Some results of this testing will be discussed in *The NaI Stack* section. These tubes have greater than a factor of two variation in their tube to tube gains. If all of the stack photomultipliers were powered with the same high voltage distribution, the maximum response on some of the ADC circuits would be lower than half-scale in order to keep the others on scale. To minimize this effect for maximum utilization of the ADC dynamic ranges, we do not use the same high voltage setting for the 72 tubes. Instead, we use the following scheme. The photomultipliers are grouped into 12 groups according to their rankings in gains so that each group will have small variation (typically 10%) in gain. The six tubes from each group are used on the stack with tubes from the same group read out by the same motherboard and sharing the same high voltages. Six tubes from any given group are placed on six alternating layers of the stack. This is done to minimize the relation of the electronics and high voltage to the stack layers, so that information on any layer will not be totally lost in the event of single electronics or high voltage failure. The Amperex 2008 tubes are 10 stage photomultipliers and we use the first 7 stages to adjust the gains of the tubes. The anodes are all connected to +376V, D10's (the 10th dynodes) are all connected to +248V, D9's to +160V, D8's to +72V, D7's to ground, and D6's through K's (cathodes) will have different settings for different groups. The voltages of D6 through K can be adjusted only by steps of 8V because of the battery configuration. Nevertheless, this is good enough to adjust the gains to within 10% variation. The photomultipliers' ranking, grouping, and location in the stack are documented in the *Stack PM Info.* folder; and the high voltage settings are documented in the *Stack HV Distribution* folder.

2.2.5. Thermal Control Subsystem

The sodium iodide scintillators in the stack are extremely sensitive to temperature, both in light output and structurally. Therefore, we like to keep the stack at a near constant temperature. By thermally isolating the hermetic can, which contains the NaI detectors, as much as possible from the remainder of the experiment, we can slow down the rate of heat transfer. However, with the experiment's electronics and power conditioning system dissipating about 260 watts, the temperature of the gondola will increase with time unless a means is devised to remove the unwanted heat. A number of possibilities were considered : flying a block of ice, utilizing other means of "storing cold" such as liquid nitrogen, improving the thermal connection to the outside world during the nights, and active or passive refrigeration systems. After careful consideration, a refrigeration system, which utilizes the evaporation of water into the near-vacuum that exists near the gondola during the balloon flight, was chosen. Water appears to be the best choice for the working fluid because it is commonly available, has a very large heat of vaporization near room temperature, and has a reasonably high vapor pressure near room temperature. About 18 kilograms of water is needed to offset the heat generation by the system for a flight duration of 2 days. Our cooling system has a donut-shape aluminum container with about 50 liter capacity (i.e., same as 50 Kg for water). At launch, this container will be filled to about two thirds of its capacity to give us approximately a factor of two safety margin for the 2 day flight. The cooling system has three valves for controlling the cooling cycles so as to prevent single point failure of this system. These valves can be controlled automatically by a group of temperature sensors located at different parts of the gondola, or manually by sending commands. There are also two fans inside the gondola to give air circulation to equilibrate the gondola thermally.

2.2.6. Command Subsystem

With a complex instrument such as this one, it is wise not to totally rely on preconceptions, but rather leave the experimenters some real-time controls on the instrument. To do this, we put a command system on board HEIST. Through this command system, we can switch the power to the subsystems, including the high voltage supplies, define the trigger requirements, set the thresholds of discriminators on the trigger logic, switch the video recorders on and off, select automatic or manual mode for the cooling system and control the valves in the manual mode, and release gas stored in a gas bottle in case of decreasing pressure inside the gondola due to leakage. This command system has two command receivers for redundancy. They operate at different frequencies and only one of them is needed at any given time.

2.2.7. Ground Support Equipment

A minicomputer based ground support equipment system (GSE) was built to do on-line monitoring, system calibrations, real-time data acquisitions and real-time data analysis. This is a PDP11/10 based system with the following peripherals :

1. a system console terminal for entering instructions to the computer and editing programs

2. a set of console switches which interface to computer programs for various control functions
3. 28 K words (16 bits) of random access memory for program execution and data buffers
4. a dual floppy disk drive (RX02) for program and data storage and retrieval
5. a magnetic tape drive (Kennedy 9-track) for transferring telemetry data or video data onto magtapes
6. a clock (TCU100) for keeping time and generating 1-minute interrupts to the CPU for housekeeping purposes
7. an arithmetic extention unit (KE11A) for fast arithmetics
8. a storage scope (Tektronics 603 driven by an AR11) for graphic display of various types of data
9. terminal interfaces (DL11-B) for connections to terminals and printers for data entries, printouts, and pseudo-stripcharts
10. a DMA controller (MDB11, an equivalent of DR11) for taking data input from either the telemetry interface or video interface
11. parallel i/o ports (DEC kit 11-H) which connects to a DAC for system calibration and a command status display panel for command verification.

For details on the hardware and system configuration, please see Koon Lau's *HEIST GSE Notebooks, volume I & II.*

Extensive software packages have been written for this system to handle monitoring, calibrations, graphic displays, and data analysis. Directions for using the software can be found in Eric Christian's *User's Guide to HEIST Software*. We present here a very brief summary of the software capabilities. The HEIST GSE runs under the FORTH operating system which contains an editor and other utility functions. Some of the most often used functions are listed below:

1. MONITOR -- which monitors the systems voltages and currents. It works like a storage scope with 16 input channels and samples each of the channels at 2 ms intervals.
2. HCAL -- which does automated calibration of the ADC circuits at 8 voltages and determines the gains and offsets from these calibration points
3. translation of data from video tapes onto magtape
4. on-line recording of telemetry data
5. verification of commands and system status through telemetry data
6. keeping a minute by minute record of all the housekeeping data on floppy disk
7. displaying housekeeping data on the storage scope and putting up to 9 channels of housekeeping data on a pseudo-stripchart
8. doing real-time data analysis through either telemetry or video data link and displaying the results graphically on the storage scope.

The GSE is a very important system both during accelerator calibrations and flight. It allows the experimenters to perform real-time data analysis. This is particularly important during flight, at which time the experimenters need to get a real-time feedback from the system before they can make such decisions as discriminator threshold settings, trigger requirement, cooling system operations, etc.

2.3. The NaI Stack

The sodium iodide stack is a major component of this instrument. The stack consists of twelve 2 cm thick NaI discs and provides measurements for both ΔE and particle trajectory. NaI(Tl) is suitable for this purpose because it is a hard, homogeneous material capable of being ground and polished to an optical finish; and because for a given stopping power it causes fewer fragmentation reactions than does plastic. In addition, NaI(Tl) is efficient at converting dE/dx energy losses into visible light, and this efficiency remains more constant with the large dE/dx values for heavy ions as compared to plastic scintillator (Salamon and Ahlen 1981, 1982). Another candidate for the scintillation material would be CsI which has similar properties as NaI; however, it costs five to seven times as much as NaI. The discs were prepared in a similar fashion to that previously described (Buffington, Lau and Schindler 1981), except here they are each viewed by six photomultipliers rather than four; and the photomultipliers are mounted within the hermetic can. The 72 photomultipliers are individually digitized, thus permitting measurement of the particle transverse coordinates and energy deposition in each layer. A muon (relativistic $Z = 1$ particle) passing through the stack near the axis yields typically 10^2 photoelectrons in each photomultiplier. The individual layer energy deposition measurements are constrained in the data analysis to fit a proper Bragg energy deposition curve for the isotope, and the resulting fit is effective in removing most types of fragmentation events. The position information can be used to correct position dependences in the responses of the individual NaI stack layers, and also provides the trajectory information for similar corrections in the Cerenkov counters and plastic scintillators above and below the stack. In this section, we will discuss the construction of the stack and some of its ΔE and position measuring capabilities.

Because of the hygroscopic nature of NaI, the stack has to be kept in a dry environment. A hermetic can was built for this purpose. In addition to the NaI discs, the hermetic can also houses the plastic lightpipes and the 72 photomultipliers. Cable harnesses and hermetic electrical feed-through connectors were used for connecting the photomultipliers to the outside. The lightpipes were constructed from 0.75 inch thick plexiglass. These lightpipes have a 30 inch outer diameter. The inner diameters are 22.3 inches except for layer 5 where it is 20 inches to accommodate the smaller disc. Figure 2.9 shows a picture of one of the lightpipes. A 1/16 inch thick, 5/8 inch wide, plexiglass ring was glued to the bottom of each lightpipe around the inner diameter to support the scintillator disc. Six plexiglass tube holders were glued onto the outer edge of each lightpipe at 60° apart. Each of the tube holders was constructed by glueing a plexiglass cylindrical cup onto a near trapezoidal piece of plexiglass. The inner cylindrical surface was threaded. Figure 2.10 shows some tube holders with and without photomultiplier. Threaded aluminum rings were used for holding the photomulitpliers in place. A thin piece of glass, with diameter slightly larger than that of the photomultipliers, was glued on the face of each photomultiplier for this tube attachment scheme. A 1/16 inch thick silicone wafer placed between the photomultiplier and the holder was used to improve the optical coupling.

The lightpipes were sanded and painted black except on areas where scintillation light might have a direct reflective path to one of the photomultipliers. This was done to minimize the contribution of secondary light from reflection and scattering. For better position resolution, we tried to minimize this secondary contribution to maximize the gradient of light collection

Figure 2.9

Top view of one of the plexiglass lightpipe with one photomultiplier attached. Ignore the gray background caused by the shadow of the black paint on the lightpipe. The lightpipes were sanded and painted black except in areas where scintillation light might have a direct path to one of the photomultipliers. This is done to minimize the contribution of secondary light from reflection and scattering. For better position resolution, we tried to minimize this secondary contribution to maximize the gradients of light collection efficiencies. The lightpipes were constructed from 0.75 inch thich plexiglass. These lightpipes have a 30 inch outer diameter and a 22.3 inch inner diameter except for layer 5 where the inner diameter is 20 inches to accommodate the smaller disc. A 1/16 inch thick, 5/8 inch wide, plexiglass ring was glued to the bottom of each lightpipe around the inner diameter to support the scintillator disc. The inset of the figure shows a cross-sectional view of the scintillator-lightpipe interface. The silicone adhesive provides optical coupling between the scintillator and the lightpipe as well as holding the scintillator in place.

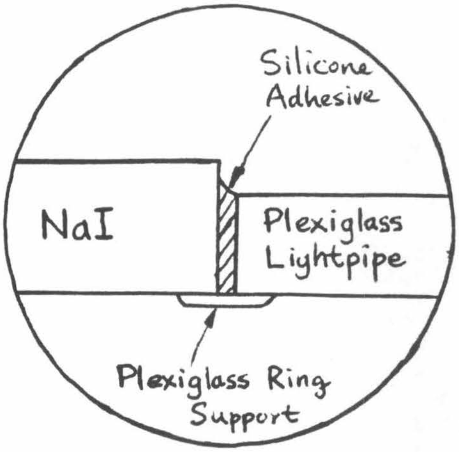
Silicone Adhesive
NaI
Plexiglass Lightpipe
Plexiglass Ring Support

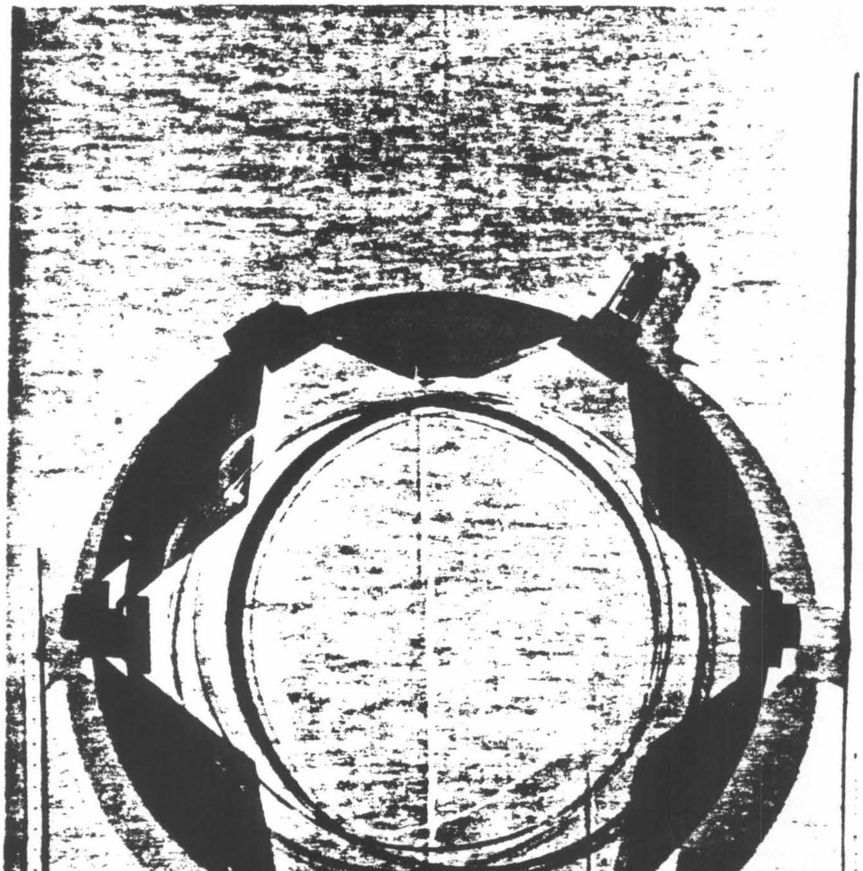

Figure 2.10

Picture of tube holders with and without photomultipliers. Threaded aluminum rings were used for holding the photomultipliers in place. A thin piece of glass, with diameter slightly larger than that of the photomultiplier, was glued on the face of each photomultiplier for this tube attachment scheme. A 1/16 inch thick silicone wafer placed between the photomultiplier and the holder was used to improve the optical coupling.

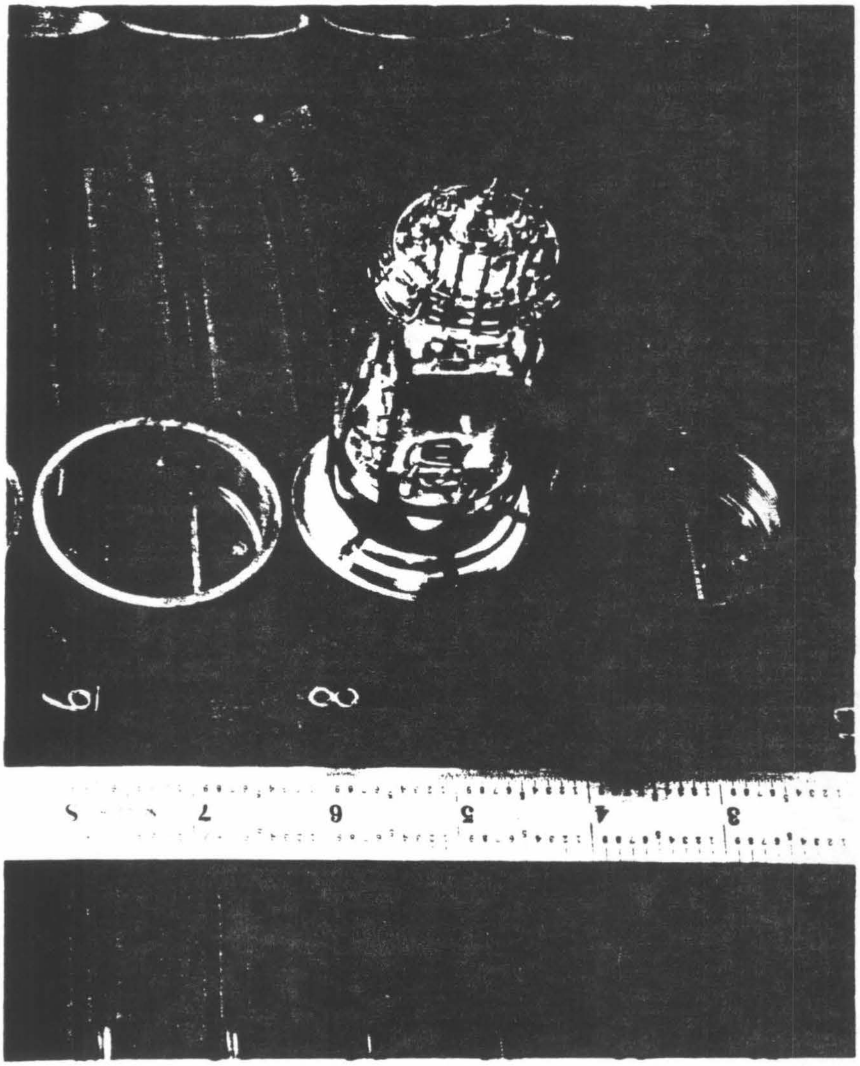

efficiency as a function of position. The inside of the hermetic can was painted black and black painted aluminum foils were employed between layers to minimize inter-layer optical coupling. Figure 2.11 shows the complete assembly of the stack lightpiping system.

To remove most of the water content, we baked the hermetic can with the lightpipe assembly inside (without scintillators and photomultipliers) at 85°C for about 100 hours, while flushing the hermetic can with dry nitrogen. The hermetic can along with the lightpipe assembly was shipped to Cleveland for installation of NaI scintillators inside a dry room at the Harshaw Chemical Company. Detailed installation history can be found in the HEIST Lab. Notebook. The NaI scintillator discs were cut and machined to size. Each disc was ground to a constant thickness within 50 μm and all of its surfaces were polished to a bright specular finish. The discs were glued to their lightpipes with a silicone adhesive material (see inset of figure 2.9). This silicone adhesive provides optical coupling between the scintillators and the lightpipes as well as holding the scintillators in place.

The Amperex 2008 was chosen for the photomultipliers because of its good linearity characteristics and its low cost (~$70 per tube for quantity of 100). Six different models of photomultipliers from 3 companies, were tested for linearity, before the procurement of the Amperex 2008 tubes. The results of this testing were reported in the *PM Selection* memo by Koon Lau (dated October 29, 1980). Before we present a summary of the findings, we will discuss briefly saturation of photomultiplier response. Saturation, in this context, occurs when the output current (or charge) no longer holds a linear relationship with the input light level. At any given operating voltage, the output current of a photomultiplier will start to saturate when the input light level is increased above a certain point. This is due to space charge

Figure 2.11

Picture of the complete assembly of the stack lightpiping system. The lightpiping system is shown being supported by the bottom plate of the hermetic can. The top plate and side wall were removed. The inside of the hermetic can was painted black and black painted aluminum foils were employed between layers to minimize inter-layer optical couplings.

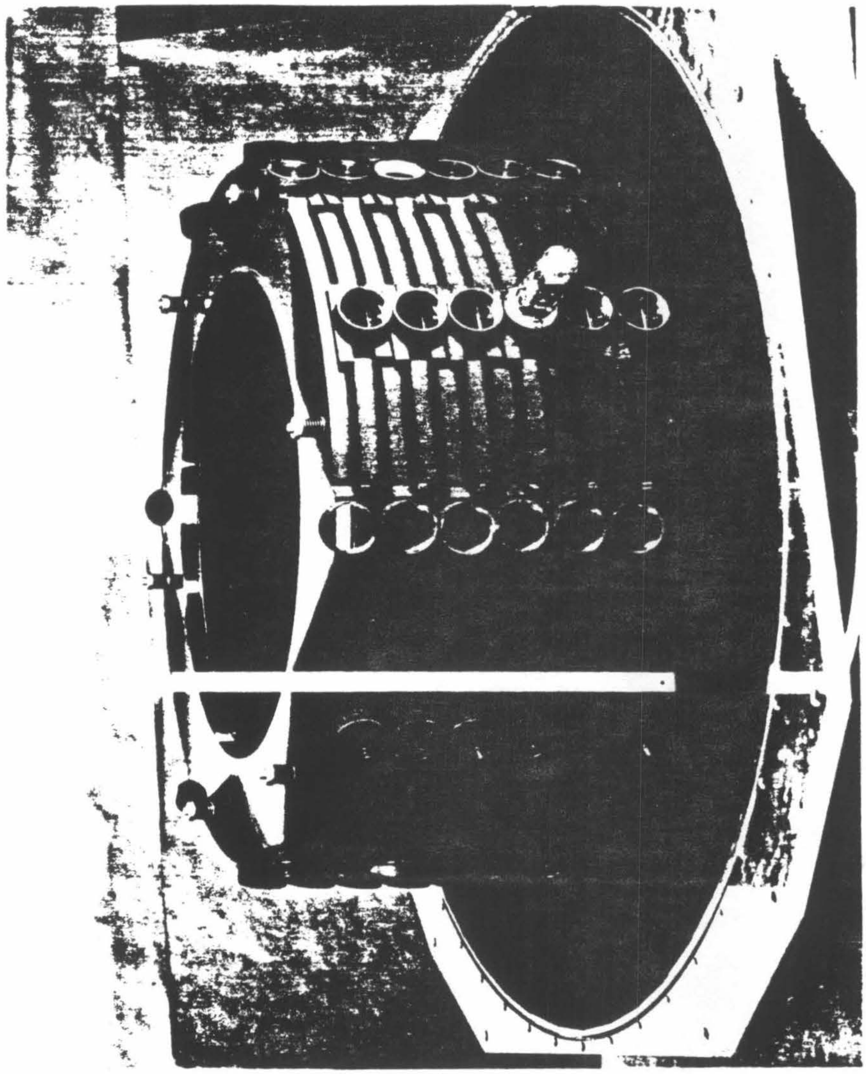

effects in the last few stages of the photomultiplier. At this point, while the output current starts to saturate, if one integrates the total output charge, the integrated charge will still remain linear with the integrated light input. However, at a yet higher light input level, even the integrated charge will start to saturate. Since we are interested in the charge, rather than the current, in this experiment, we are more concerned with the latter type of saturation. These saturation points occur at lower light input levels with higher operating voltages. However, it was found that, to first order, saturation starts at about the same output current or charge level with varying high voltage.

The six models tested were: EMI 9837, EMI 9872B, Amperex 2010, Hammamatsu R1398V, EMI 9843B, and EMI D550. The EMI 9837 had a Venetian Blind dynode structure, whereas the others had a squirrel cage dynode structure. There were two types of squirrel cage structures. The Amperex 2010 and the EMI D550 had linear focus structure and the other three squirrel cage models had a wrapped around structure. The Amperex 2010 was identical to the Amperex 2008 electrically with only differences in the packaging. A light box was used for the measurements. Six LED's, driven by $0.25\mu s$ current pulses, were used as the light source. Since the different models had different photocathode sizes, a 0.88 inch diameter aperture was used in front of tube face to give roughly the same light level for the different tubes. The light intensity was varied by using Kodak neutral density filters. For each photomultiplier, current and charge levels were measured at various light levels. At least two tubes of each kind were tested using this setup. The measurements showed that squirrel cage type tubes had much better linearity characteristics than the Venetian Blind type, which was what the manufacturers indicated. The linear focus structure was found to be better than the wrapped around structure among the squirrel cage models. The Amperex 2010 and EMI D550 were comparable in linearity with the Amperex 2010 showing slight superiority. Twelve Amperex 2008 tubes were then obtained and tested. Test results showed that a typical Amperex 2008 was as good as the Amperex 2010 tubes tested. Saturation of charge did not occur until the output charge level was above 10,000 pico-Coulomb. Two of the twelve had worse than typical saturation characteristics, but even these were very linear when output current was below 7,000 pico-Coulomb. Based on this result, we set the sensitivity of the ADC circuits at 1.22 pico-Coulomb per bin (i.e., a fullscale of 5000 pico-Coulomb), so that we could fully utilize the ADC dynamic range without having to worry about saturation of photomultiplier responses.

Because of the positive results of the photomultiplier test, we decided to use the Amperex 2008 for the stack. Another shipment of tubes was ordered to give us a total of 100 Amperex 2008 tubes. After the glass discs were glued on the photomultiplier faces, gain and linearity measurements were made on each of the 100 tubes. They were then ranked and grouped according to their gains as described in the previous section. Photomultipliers were then installed on the lightpipes with the hermetic can inside a dry glove box (descriptions of the glove box can be found in *A Dry Box For Working With NaI* memo). The photomultipliers were carefully oriented so that the least magnetic-sensitive axis was horizontal. This was done because the horizontal component of the earth's field experienced by the photomultipliers would vary more than the vertical component during the balloon flight. To futher minimize the effect of magnetic field variations, a cylindrical magnetic shield was put around each of the photomultipliers. The magnetic shields were constructed from one layer of 0.004 inch thick

μ-metal (AD-MU-78 from Ad-Vance Magnetics, Inc.). Laboratory tests showed that, with this configuration, the earth's magnetic field would not have any significant effect on the photomultiplier responses. The high voltage distributions on the first 7 stages of the photomultipliers were adjusted for each group of photomultipliers so that the twelve groups had comparable responses for sea-level muons. The high voltages on the last 4 stages were adjusted at the Bevalac, using data from stopping ^{55}Mn ions, such that the maximum response from a slow Ni ion would not go off-scale on any one of the 72 ADC circuits.

The stack of NaI discs was exposed to Bevalac carbon, neon, and argon beams in June 1981 and to a manganese beam in November 1982. The first Bevalac data set only covered less than half of the stack area. Nevertheless, it provided us important information on position resolution. The latter provided data for adjusting the high voltage settings and hopefully would also yield response maps for most of the stack. For both Bevalac runs, multiwire proportional counters were used, in front of the apparatus, to record particle trajectory.

Scintillators have been used in the past to determine the location at which a charged particle traverses them (Arens 1974; Rogers et al. 1974; Zych et al. 1979; and Arens et al. 1979). These position-measuring scintillators (which Arens et al. call "entopistic") utilize the principle that the scintillation light is gathered unequally by the photomultiplier viewing system, depending upon the position at which the light was generated. A fundamental limit of such systems is set by photoelectron statistical fluctuations within the individual photomultipliers viewing the scintillator. Even though this limit is theoretically only one or two millimeters for many of the systems which have been tested, systematic errors of various kinds have limited the actual performance of these systems to about one centimeter accuracy. A 1.73 cm thick, 50 cm diameter, NaI disc was exposed to a beam of 670 MeV/nucleon neon in 1980. We (Buffington, Lau, and Schindler 1981) have shown that a position resolution of less than 3 mm was achievable for neon.

The amount of light detected by a photomultiplier viewing the NaI depends on the amount of scintillation light generated, and the position at which the light was generated. With more than one photomultiplier viewing a scintillator, the first of the two dependences can be eliminated by taking a ratio of different photomultiplier responses. Therefore, ratios of photomultiplier responses only depend on the position at which the light was generated. Figure 2.12a shows such a dependence for the ratio of responses from two photomultipliers on one of the stack scintillators. The photomultipliers are located opposite to each other on the lightpipe (i.e., 180° apart). The data were taken with neon ions going through a 10 cm by 10 cm area at the center of the scintillator disc. One can see from the width of the line that position resolution of less than 1 cm can be achieved.

It was found that the ratio of the responses of two photomultipliers (denoted as R from now) changes by roughly a fixed percentage for a given change in position; that is

$$\frac{\Delta R}{R} \simeq \kappa \cdot \Delta X. \qquad (2.29)$$

Since $\Delta R/R$ is equivalent to $\Delta \log R$ (log is natural log, not the log of base 10), equation (2.29) gives

$$\Delta \log R \simeq \kappa \cdot \Delta X. \qquad (2.30)$$

This says that logR forms a linear relationship with the position, at least in a limited area. Figure 2.12b shows this linear relationship, for the data set of

Figure 2.12

Figures showing the correlations between the position, as measured by a multi-wire proportional counter, and, (a) the ratio of responses from two photomultipliers which are located opposite to each other on the lightpipe (i.e., 180° apart), (b) the natural log of the ratio described in (a). It was found that the log of the ratio forms a linear relationship with the position, at least in a limited area. The slope of the line in figure (b) is 0.048 cm^{-1}. The data were taken with neon ions going through a 10 cm by 10 cm area at the center of a scintillator disc.

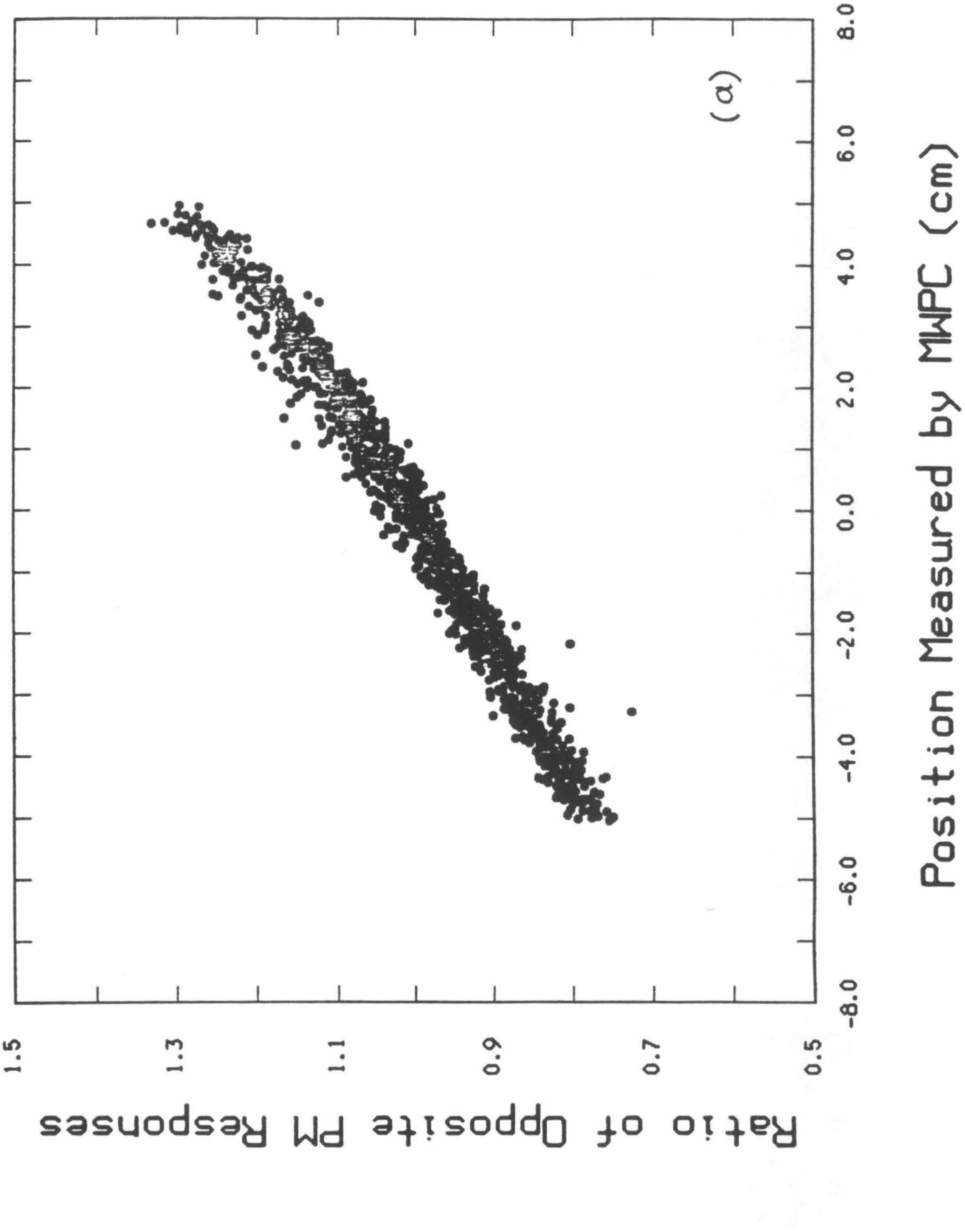
(a)
Ratio of Opposite PM Responses
1.5
1.3
1.1
0.9
0.7
0.5
Position Measured by MWPC (cm)
-8.0
-6.0
-4.0
-2.0
0.0
2.0
4.0
6.0
8.0

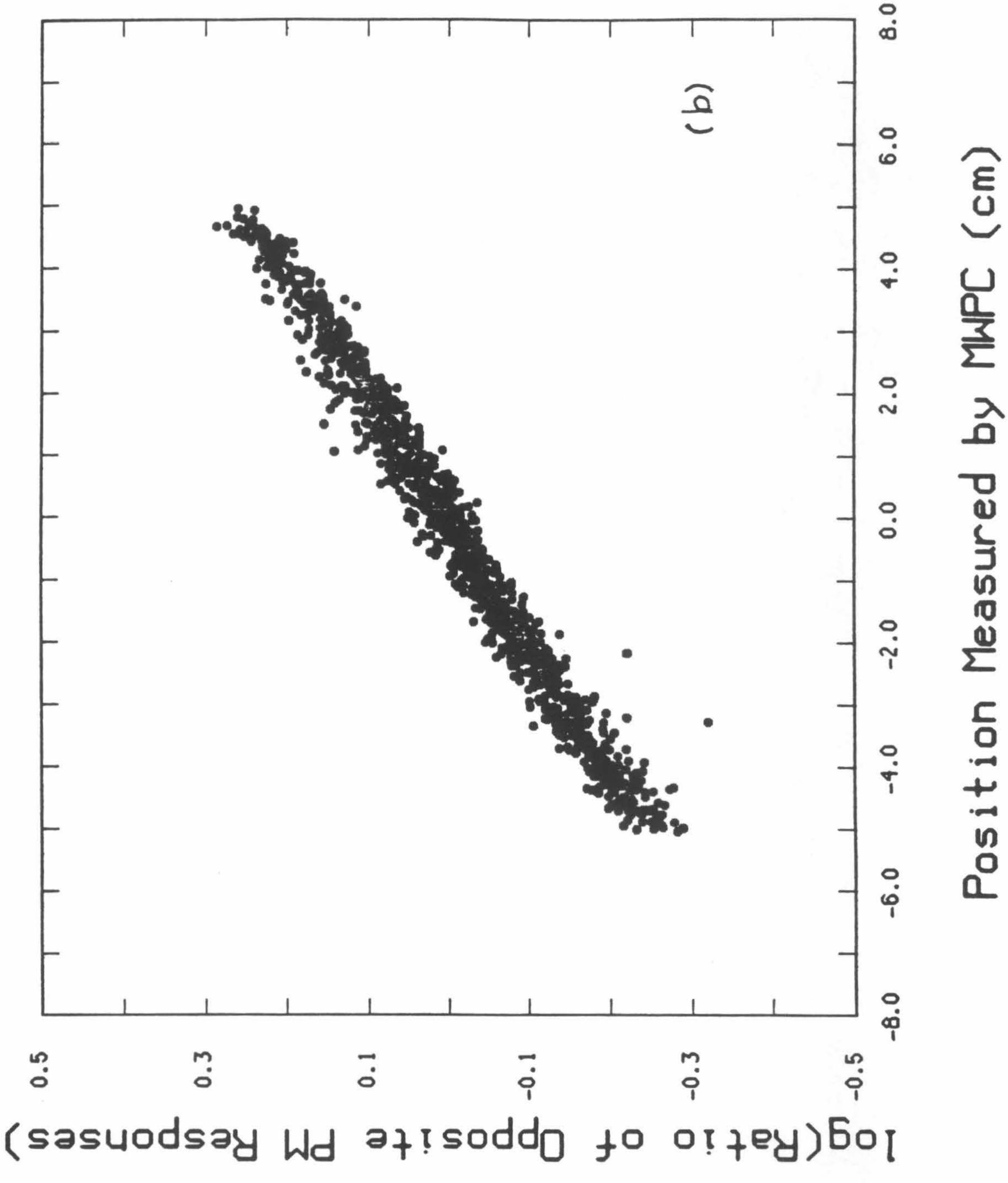
(b)
Position Measured by MWPC (cm)
log(Ratio of Opposite PM Responses)
-8.0
-6.0
-4.0
-2.0
0.0
2.0
4.0
6.0
8.0
0.5
0.3
0.1
-0.1
-0.3
-0.5

figure 2.12a, with κ being 0.048 cm^{-1}. Equation (2.30) also says that the uncertainty in logR (which is the same as the fractional uncertainty in the ratio) is proportional to the uncertainty in position (which is the same as the position resolution). It was found that the uncertainty in logR does not depend on the position to first order. Therefore, the uncertainty in logR can be deduced from a distribution of the difference between logR and $\kappa \cdot X$. Figure 2.13 shows such a distribution for a data set which the data of figure 2.12b is a subset of (this data set only has more events). The distribution is not centered at 0.0 because the ratio, R, is not 1.0 at X = 0.0. This is due to the fact that the gains of the photomultipliers are not balanced exactly, which can be remedied by using software gain corrections. Notice the uncertainty in logR is not affected by the gains; this is one of the nice features of using "log". The distribution has a FWHM of 0.042, and thus a deduced standard deviation of 0.018. With $\kappa = 0.048$, this implies a position resolution of 0.37 cm. However, this position resolution includes other systematic uncertainties such as multi-wire proportional counter position uncertainty, position uncertainty caused by multiple Coulomb scattering, direction uncertainty caused by stochastic beam divergence, etc.

If we compare ratios of photomultiplier responses from two nearby NaI scintillators, instead of comparing a ratio with position measured by a multi-wire proportional counter, some of the systematic uncertainties can be eliminated and others can be reduced in magnitude. In this case, the multi-wire proportional counter position resolution will not be contributing. The multiple Coulomb scattering will be smaller in magnitude because the amount of material, between the two locations in the measurements, will be reduced. The distance between the locations is also reduced, thus reducing the lever arm for both multiple Coulomb scattering and stochastic beam

Figure 2.13

A distribution of the difference between the log of the ratio and 0.048*X. The distribution is for a data set which the data of figure 2.12 is a subset of (this data set only has more events). The distribution is not centered at 0.0 because the ratio, R, is not 1.0 at X = 0.0. This is due to the fact that the gains of the photomultipliers are not balanced exactly. The distribution has a FWHM of 0.042, and thus a deduced standard deviation of 0.018. With a slope of 0.048 in figure 2.12b, this implies a position resolution of 0.37 cm. This position resolution includes other systematic uncertainties such as multiwire proportional counter position uncertainty, position uncertainty caused by multiple Coulomb scattering, direction uncertainty caused by stochastic beam divergence, etc.

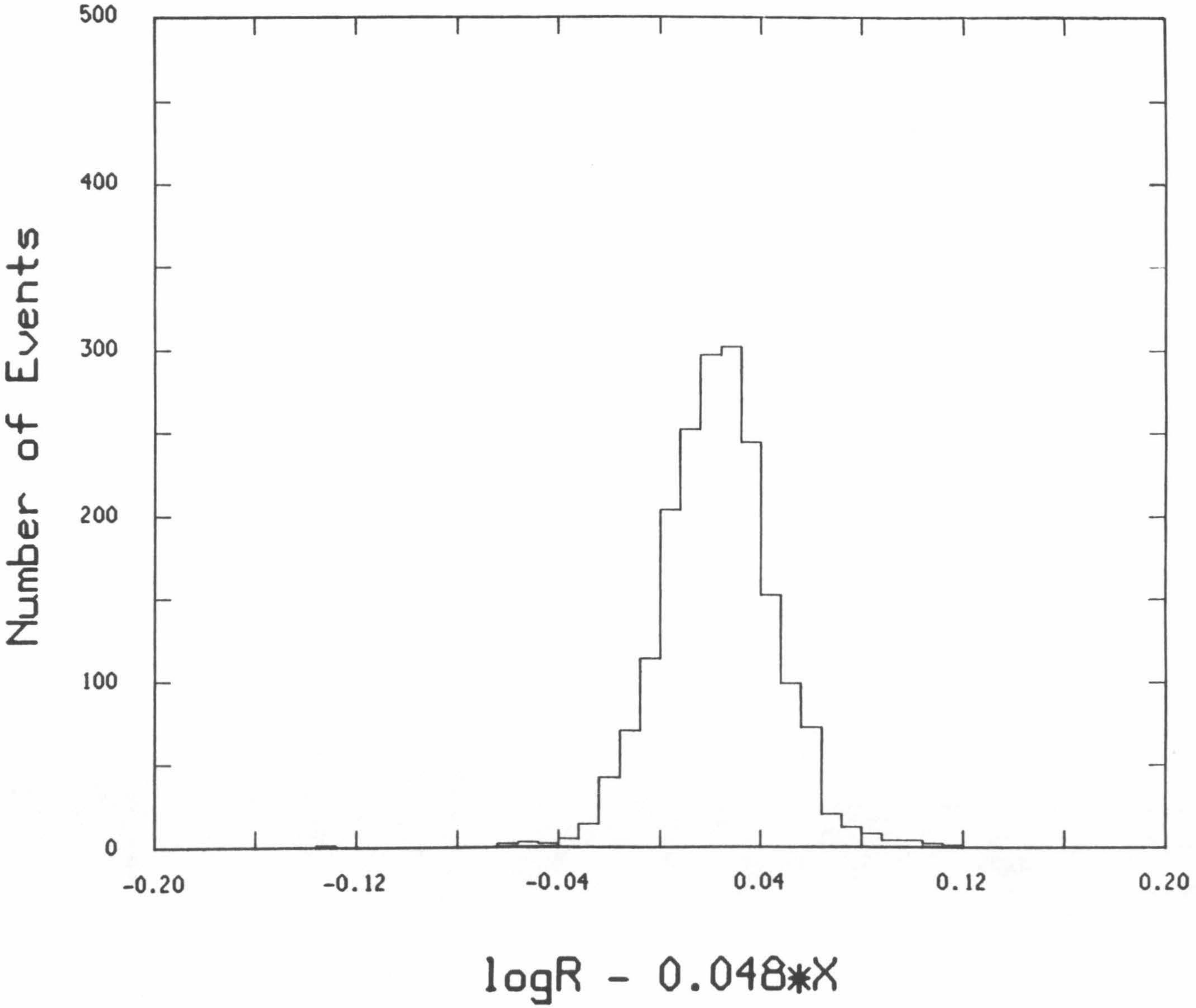
Number of Events
500
400
300
200
100
0
-0.20
-0.12
-0.04
0.04
0.12
0.20
logR - 0.048*X

divergence. Therefore, the ideal case seems to be one in which two adjacent layers of the stack scintillators are used in the analysis. Unfortunately, two adjacent layers do not have their photomultipliers aligned in the same places (as can be seen in figure 2.11). This makes the comparision a little difficult. So, we will go to the next best situation by using two scintillators separated by only one layer. In this case, the other uncertainty contributions are still negligible compared to the intrinsic position resolution of the two layers. The position resolution obtained by this method has contributions from both layers involved, and therefore, is a weighted sum of two position resolutions. The weighting factors are the energy depositions in the respective layers.

Using the method described in the above paragraph, the position resolution of a single NaI scintillator is deduced to be 0.23 cm for neon ions, instead of 0.37 cm. Similar analyses were done with muons and carbon ions. The manganese data show a dependence, on the accelerator particle beam intensity, for the photomultiplier responses. This dependence is different for different photomultipliers. As a result, the ratio of responses from two photomultipliers will have a dependence on the accelerator beam intensity. To minimize this effect, we used one pair of photomultipliers to deduce the position resolution (instead of using the above method). First order corrections to photomultiplier responses were made to reduce the effect of the beam intensity dependence. Uncertainties caused by multiple Coulomb scattering and the multi-wire proportional counter are then subtracted from this deduced resolution. For a pair of photomultipliers on layer 4, we deduced a position resolution of 0.170±.003 cm from the log of the ratio. Uncertainties caused by multiple Coulomb scattering and the multi-wire proportional counter are estimated to be 0.086±.010 cm and 0.070±.010 cm respectively. Therefore, the best estimate of the position resolution is 0.129±.014 cm for manganese. These results are presented in Table 2.1.

The major determining factor of the position resolution is photoelectron statistical fluctuations. The number of photoelectrons should scale with the square of the charge, Z^2, of the incident particle. For particles of the same charge, lower energy particles have more photoelectrons because of the higher dE/dx. On the other hand, with higher dE/dx, we have lower scintillation efficiency. Figure 2.14 shows the position resolution as a function of scintillation output with the dE/dx and scintillation efficiency factors taken into account. The neon data point has relative response of greater than 10 because the neon ions were at relatively low energy (~500 MeV/nucleon). The manganese data point has relative response of less than 25 because of saturation in scintillation efficiency. The muon, carbon, and neon data points fall onto the Z^2 scaling line which suggests that other systematic uncertainties are not important for elements with $Z \leq 10$. The manganese data point suggests that systematics will limit us to ~0.13 cm resolution. Nevertheless, this is good enough for measuring particle trajectory and for correcting position variation of scintillator responses.

The variation of the sum of six photomultiplier responses for a stack layer is less than 1%/cm for most of the area except for areas near a photomultiplier. Combined with a less than 0.2 cm position resolution, this gives a better than 0.2% measurement on the scintillation light. This says that position variations should not be the limiting contributor of the uncertainty in the ΔE measurement. The major contributor of uncertainty in the ΔE measurement is probably going to be the corrections for the scintillation efficiency in the different layers and mapping errors.

The scintillation efficiency was studied using the ^{55}Mn data of November

Table 2.1	
Element	Resolution (cm)
Muon	2.125 ± .117
Carbon	0.351 ± .013
Neon	0.231 ± .008
Manganese	0.129 ± .014

Table 2.1 Position resolution for a 2 cm thick NaI disc.

Figure 2.14

Figure showing position resolution achieved by the NaI scintillators for muon, carbon, neon, and manganese ions. The position resolution is determined by the photoelectron statistical fluctuations. The manganese data point falls out of the Z^2 scaling line suggesting that other systematics will limit the position resolution to ~0.13 cm for a single NaI scintillator disc.

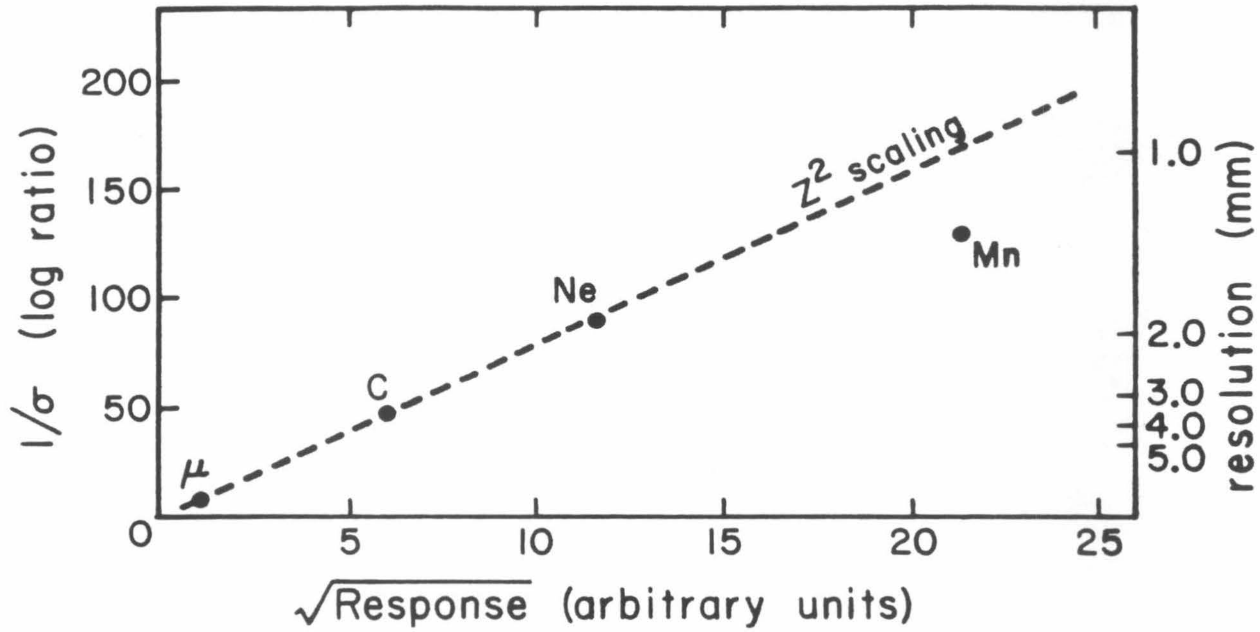
1/σ (log ratio)
200
150
100
50
0
5
10
15
20
25
√Response (arbitrary units)
resolution (mm)
1.0
2.0
3.0
4.0
5.0
μ
C
Ne
Mn
Z² scaling

1982. The gains of the stack photomultipliers were balanced using on-axis events from the front and rear entry exposures. Layer-to-layer gain adjustment was done by fitting the data to an expected Bragg energy deposition curve through the stack. There is good agreement for this adjustment by comparing the front and rear entry data for the middle layers. Values of light output/energy deposition, dL/dE, are then obtained for the final four layers before the ^{55}Mn ions stopped. Figure 2.15 shows the result, together with data from Salamon and Ahlen (1981). The data were normalized so that our layer 1 value for Mn agreed with an extrapolation of their data. Values of dL/dE at smaller values of dE/dx are also obtained from the Bevalac data with 5 cm of polyethylene placed in the beam upstream. This material caused substantial fragmentation of the Mn ions in the beam, and individual charges down to magnesium can be discerned. The observed layer 1 responses are plotted in figure 2.15 versus the calculated values of dE/dx. There appears to be good agreement with the findings of Salamon and Ahlen (1981), and for these charges and values of dE/dx, the saturation in dL/dE depends mainly on dE/dx and very little on the charge Z.

Figure 2.15

Figure showing results from our scintillation efficiency study using ^{55}Mn data, together with data from Salamon and Ahlen (1981). The data was normalized so that our layer 1 value for Mn agreed with an extrapolation of their data. Values of dL/dE at smaller values of dE/dx are also obtained from the Bevalac data with 5 cm of polyethylene placed in the beam upstream. This material caused substantial fragmentation of the Mn ions in the beam, and individual charges down to magnesium can be discerned.

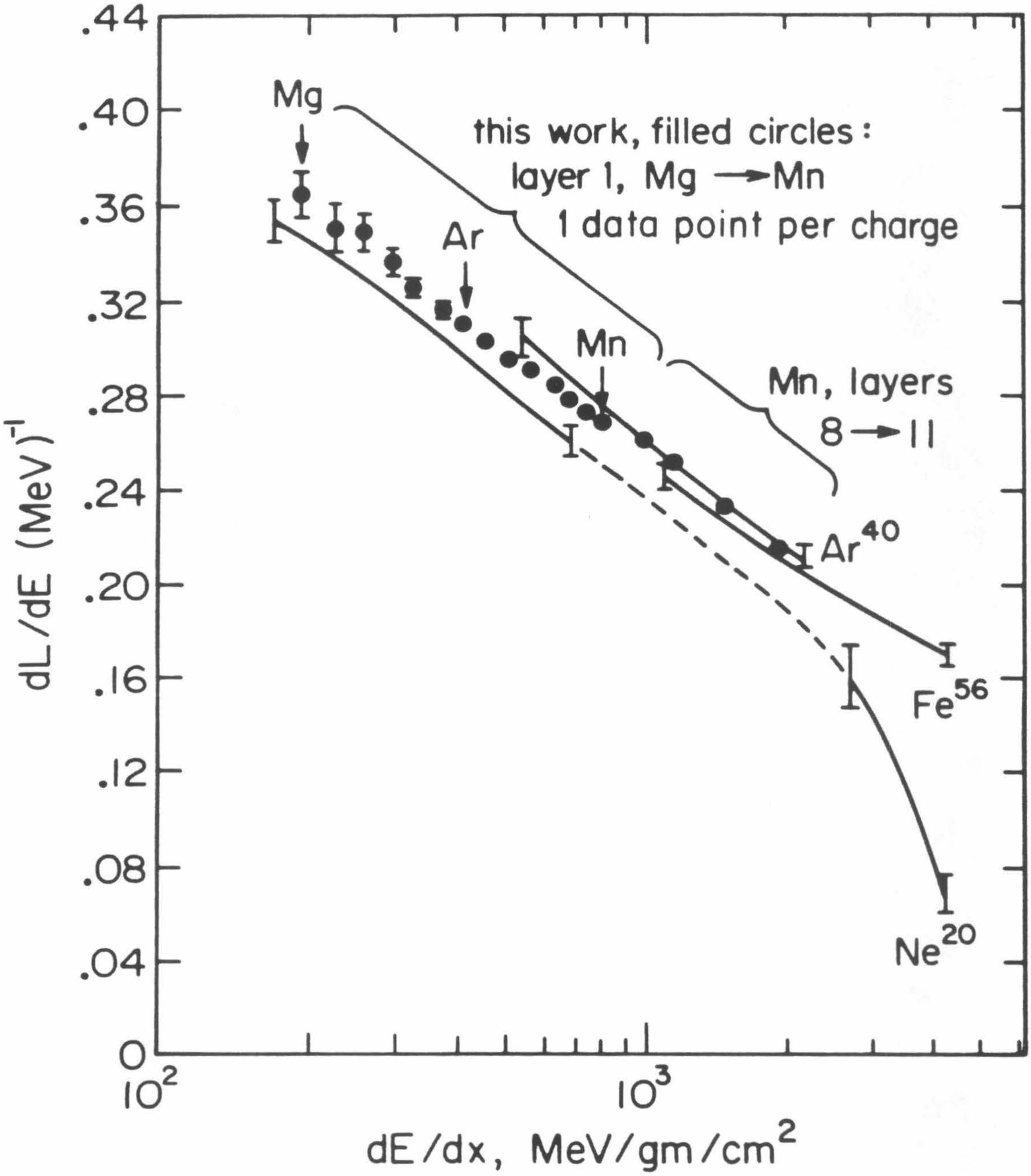
.44
.40
.36
.32
.28
.24
.20
.16
.12
.08
.04
0
10^2
10^3
dL/dE $(\text{MeV})^{-1}$
dE/dx, MeV/gm/cm^2
Mg
Ar
Mn
this work, filled circles:
layer 1, Mg → Mn
1 data point per charge
Mn, layers
8 → 11
Ar^{40}
Fe^{56}
Ne^{20}

2.4. The Plastic Scintillators and Cerenkov Counters

The plastic scintillators and the bottom Cerenkov counter are constructed using readily available items. On the other hand, the top Cerenkov counter uses aerogel as the radiator. There are 48 pieces of aerogel block which were fabricated at the Danish Space Research Institute by Ib Rasmussen. In this section, we will present discussions on the plastic scintillators, the bottom Cerenkov counter, and then the more complex top Cerenkov counter.

Two 1 cm thick, 79 cm diameter, NE110 discs are used for the top and bottom scintillators. All the photomultipliers are held in place with the same type of tube holders used on the stack. These holders were glued onto the edges of the scintillators with no other light-piping system. Thickness contour maps were made with a micrometer. Maximum to minimum variations on a disc is about 0.7 mm. The scintillators were wrapped with one layer of aluminum foil (~25 μm) and four layers of black masking tape (~150 μm per layer). The two plastic scintillators are almost identical. The major difference is that the top scintillator has two timing photomultipliers in addition to the six pulse-height-analyzed photomultipliers. The scintillators have their pulse height-analyzed-photomultipliers aligned with the photomultipliers on the even-numbered layers of the stack.

The bottom Cerenkov counter has a 1.3 cm thick teflon (n = 1.34) radiator and a 1.2 cm thick Pilot 425 (n = 1.49) radiator. They are both 60 cm in diameter. Two radiators, instead of one, are used to extend the energy converage of the bottom Cerenkov counter. The light integration box is viewed by twelve 5-inch photomultipliers.

The top Cerenkov counter consists of a mosaic with 48 aerogel pieces having refractive indices n $\simeq$ 1.1. Silica aerogels have been used as radiators in many Cerenkov counters with refractive indices between 1.015 and 1.055 (Bouffard et al. 1982; Henning et al. 1981). The refractive index of the aerogel material can be increased by heating to a temperature near 900°C (DeBrion et al. 1981). An oven has been constructed at D.S.R.I. for this purpose. As shown in figure 2.16, the radiator is fabricated from aerogel blocks 14cm square and 2 cm thick to form a mosaic 6 cm thick and more than 58 cm in diameter. Triangular pieces fill in the corners. The individual blocks were precision machined to within 50 μm of the desired size using a fly-cutting technique. The mosaic was then pressed together within a light integration box, using an array of small pressure plates around its periphery. The air gaps between the pieces of the mosaic are < 100 μm everywhere.

The raw material consisted of aerogel blocks 19 cm square and 3 cm thick, with n = 1.05, which were recycled from a CERN ISR experiment. The blocks were originally produced by the University of Lund, Sweden (Henning and Svensson 1981). No detailed production history is available. This is unfortunate, as the response of the aerogel to heat treatment varies between production batches far more than the pieces within each batch. The variations are typically $\Delta n < 0.005$ within a batch, but frequently $\Delta n > 0.05$ between batches. Of 85 blocks obtained from the CERN experiment, 48 are employed in constructing the mosaic. The selected blocks are closely matched in groups of three, having indices within 0.005, to ensure uniformity throughout the 6 cm total thickness. Like the bottom Cerenkov light integration box, the light integration box is also viewed by twelve 5 inch photomultipliers.

Preliminary analysis of the 1982 Bevalac calibration data shows that the light produced by passage of a relativistic muon normal to the mosaic yields

Figure 2.16

Schematic diagram showing the placement of individual aerogel blocks to make up the fabricated mosaic.

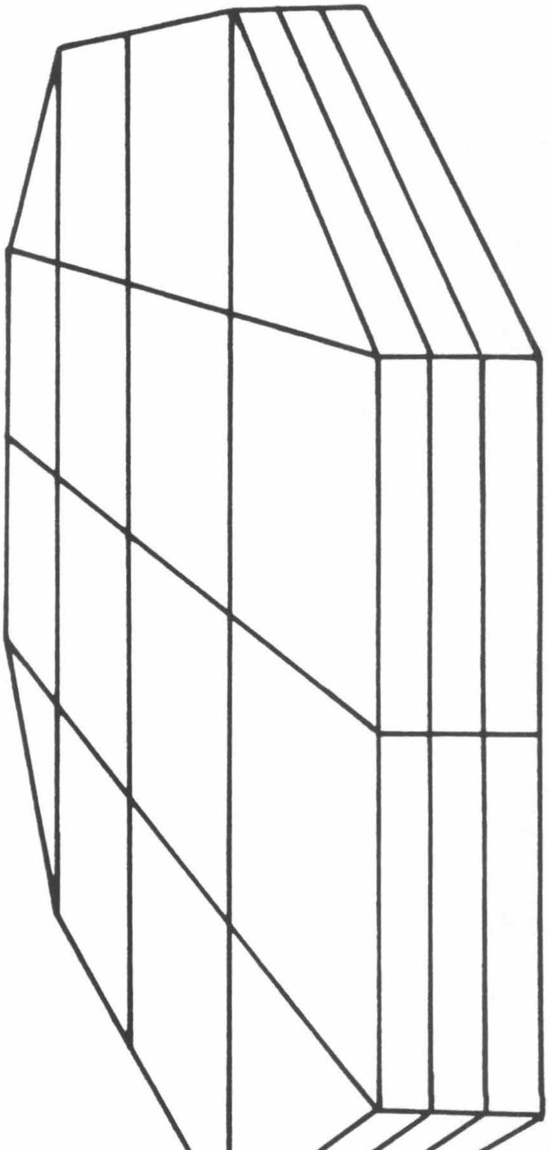

23±4 photoelectrons. The Bevalac calibration data covering ~90% of the counter surface show that >75% of the area has response variations below 2%/cm. If the position can be determined to better than 2 mm at the Cerenkov counter, 2%/cm translates into 0.4% uncertainty in the Cerenkov response. Even for iron particles, the photoelectron statistical fluctuation will be 1% or higher. Therefore, position variation will not make a significant contribution to the uncertainty of the Cerenkov response. More discussion of this analysis is presented by Rasmussen et al. 1983.

The Bevalac calibration data also provides a light collection efficiency map for the top scintillator. The calibration data was obtained with a beam of ^{55}Mn ions with incident $\gamma = 2.75$. With this incident energy, the ^{55}Mn ions stopped in the stack before reaching the bottom Cerenkov counter. As a result, light collection effeciency maps cannot be obtained, using ^{55}Mn data, for the bottom Cerenkov counter and the bottom scintillator. One might attempt to obtain these maps using events which had nuclear interactions in the stack. This requires a great deal of work, and yet might not have enough statistics. However, since we do not have any other data set, further investigation in this area is definitely worth doing. Inflight mapping of detector response for these counters is also possible using relativistic carbon and oxygen particles.

2.5. Summary and More Discussion on Mass Resolution

In the previous sections of this chapter, we have described an instrument designed to resolve isotopes with resolution better than 0.3 a.m.u. for elements from neon through iron. We have discussed some of its capabilities including the trajectory measuring capability of the stack. We have also discussed the fundamental limitations on mass resolution. In this section, we will discuss the other contributions to the uncertainty in the mass measurement; and will show that these contributions do not pose severe limitation on the mass resolution.

For the Cerenkov measurements, photoelectron statistical fluctuations have fundamental limitations on the mass resolution. As discussed in section 2.1, the photoelectron statistical fluctuation for a Cerenkov counter is just the square root of the number of photoelectrons detected. The number of photoelectrons detected is given by equation (2.11) to be $Z^2 \cdot N_{rel} \cdot f$. For Cerenkov counter with $N_{rel} = 30$, $2 \cdot 10^4$ photoelectrons will be detected for relativistic iron particles. Since the instrument is only capable of resolving mass for $f < 0.5$, the maximum number of photoelectrons detected by this Cerenkov counter would be $\sim 10^4$ for any particle of interest. This implies a photoelectron fluctuation of greater than 1%. The top Cerenkov counter with $N_{rel} = 23 \pm 4$ will have even greater fluctuations (in %).

Other contributions to the Cerenkov measurement are temperature dependence of photomultiplier response and position variations of the Cerenkov counter response. The temperature is monitored to ±0.1°C accuracy. With a typical temperature coefficient of 1%/°C for photomultipliers, the temperature uncertainty will cause a ~0.1% uncertainty in the Cerenkov measurement. This contribution is insignificant when it is added in quadrature to the greater than 1% photoelectron fluctuation contribution.

Since the stack provides trajectory information, the position variations can be corrected using a response map. If we use the positions measured by the top 5 layers of the stack to calculate the position of the particle at the top Cerenkov counter, the calculation will have an uncertainty of less than 1 mm for iron particles (since positions are known at each layer to better than 1.5 mm). However, multiple Coulomb scattering also contributes to the uncertainty in this position calculation. We estimate that multiple Coulomb scattering will have an effect of less than 1 mm for iron particles. Therefore, taking account of the multiple Coulomb scattering effect, we still can measure position at the top Cerenkov counter to better than 1.5 mm accuracy for iron particles. With the Cerenkov counter having position variations below 2%/cm (see section 2.4), the position uncertainty would give a less than 0.3% uncertainty in the Cerenkov measurement. This is still small when compared, in quadrature, to the greater than 1% photoelectron fluctuation contribution.

As described in section 2.4, the top Cerenkov counter consists of a mosaic with 48 aerogel pieces. These aerogel pieces are closely matched in index of refraction to ensure uniformity throughout the thickness of the radiator. However, there are significant variations in the index among the 16 groups even though the 3 pieces in each group are matched in index. This causes two major problems. First, the position variations might be greater than 2%/cm for areas near the boundaries of the groups. Second, if a particle goes through more than one group of aerogel blocks, the respective pathlengths in each of the groups traversed by the particle are very uncertain. To avoid these problems, we will reject events (during data analysis) with calculated trajectories crossing or near (within 2 mm) one of the boundaries. This results in a geometry factor loss of roughly 30%, assuming an isotropic flux.

For the ΔE measurement, we have shown that photoelectron statistical fluctuations make a negligible contribution to the uncertainty. With a similar analysis to the one on the Cerenkov measurement, we can show that corrections on the temperature dependence of the ΔE measurement do not make a significant contribution to the mass uncertainty.

Another factor in the ΔE uncertainty is position variations in detector responses. For one NaI scintillator, even with a 2%/cm response gradient and a 0.2 cm position resolution, we can get an accuracy of 0.4% for this measurement. With a minimum of 5 layers used in the total ΔE measurement, the accuracy for total ΔE should be better than 0.2%. Thus, by equation (2.6), this gives a mass uncertainty of about 0.1 a.m.u. for iron isotopes. For lower charge elements, the position resolution will not be as good; and thus the uncertainty in ΔE will be larger. However, the requirement on the ΔE accuracy will be less stringent. The two effects offset each other to give roughly the same mass uncertainty. Taking into account saturation in scintillation efficiency, the mass uncertainty due to the ΔE measurement should actually be lower for lower charge elements.

In the preceding paragraph, the position variations in detector responses were assumed to be mapped perfectly. In reality, the maps will have finite accuracies and will thus contribute to the uncertainty of the ΔE measurement. The position variations in detector responses are usually mapped with high energy charged particles at an accelerator facility. The accuracy of a response map will undoubtly depend on the number of particles used in the mapping process, the coverage (or the lack of) on the detector by these particles, and the computational method used in generating the map. Our detectors were mapped with high energy manganese particles at the Lawrence Berkeley Laboratory Bevalac. The mapping data are still being analyzed at the present time. Nevertheless, preliminary results show that the energy resolution of the NaI stack will be sufficient to achieve the desired mass resolution.

In this chapter, we have discussed the Cerenkov-ΔE-Cerenkov mass measurement technique and the mass uncertainty contributions associated with this method. We have described the design and construction of an instrument which is based on the Cerenkov-ΔE-Cerenkov technique. We have also presented a method of measuring position using NaI scintillators. Accelerator calibration data showed that a position resolution of ~0.13 cm can be achieved for Mn ions. We have also shown that position variation in response will dominate the uncertainty in the ΔE measurement. For the Cerenkov measurements, we have shown that photoelectron statistical fluctuations dominate the uncertainties in the Cerenkov measurements. In figure 2.17, we show the mass resolution as a function of incident Lorentz factor for the isotopes ^{20}Ne, ^{28}Si, and ^{56}Fe. According to this figure, our instrument, HEIST, should be capable of resolving mass to about 0.3 amu or better for elements ranging from neon to nickel at energies of about 2 GeV/nucleon.

Figure 2.17

Mass resolution calculated for ^{20}Ne, ^{28}Si, and ^{56}Fe incident at 30°. The solid curves are for particles which stop in the NaI stack and the dotted curves are for particles which penetrate the stack. If a particle penetrates the stack with residual energy below the threshold of the bottom Cerenkov counter, no mass uncertainty will be calculated. If a particle penetrates the stack with residual energy above the threshold of Pilot 425 and below the threshold of teflon, only the Pilot 425 radiator contribution will be calculated for the bottom Cerenkov counter. In the calculation, we assume that N_{rel} of equation (2.11) is 23 for the aerogel radiator, 15 for the teflon radiator, and 15 for the Pilot 425 radiator. If a particle penetrates the stack with residual energy above the thresholds of both teflon and Pilot 425, a composite index of 1.355 is used. We also assume that the ΔE measurement contributes 0.1 amu to the mass uncertainty.

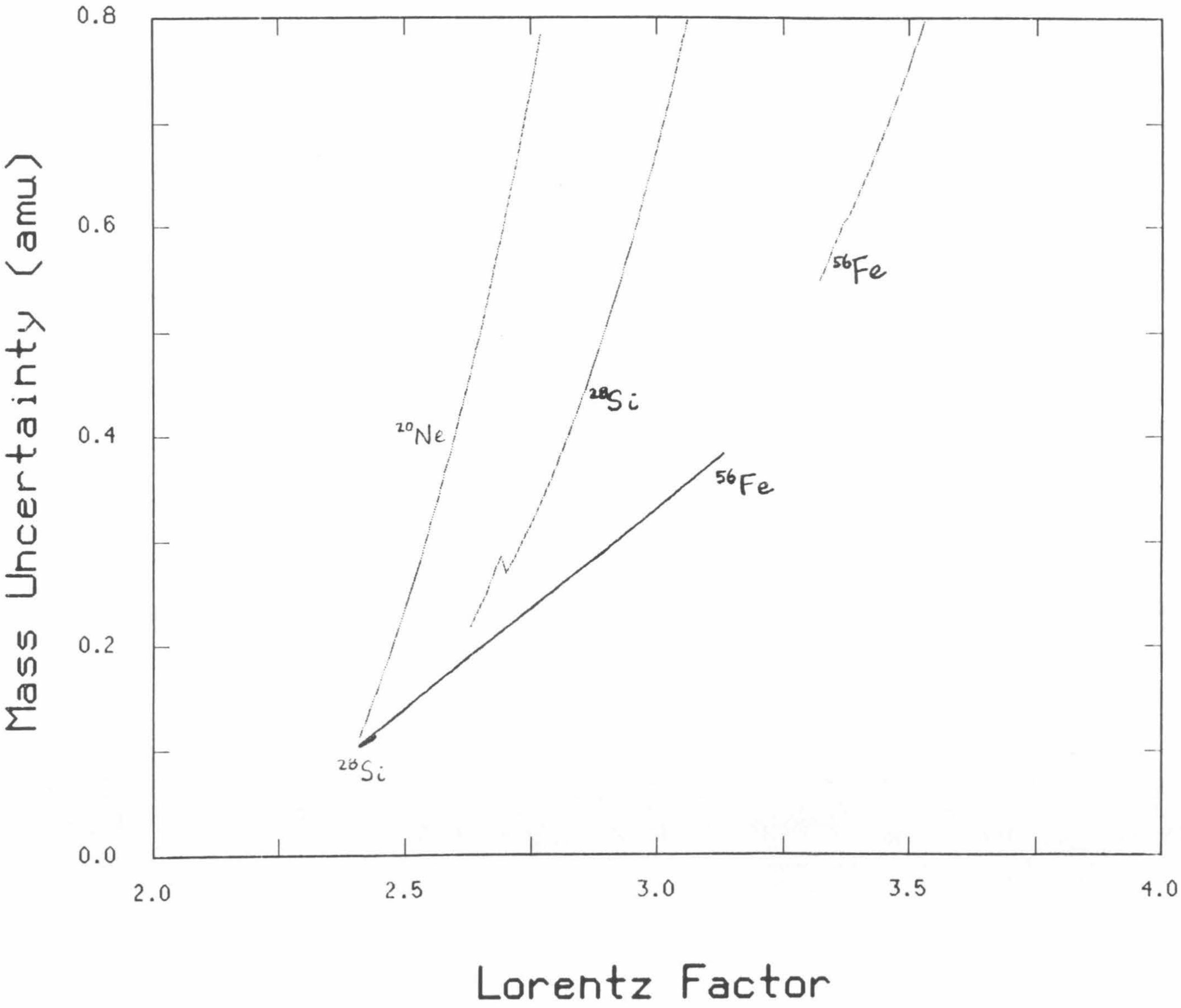
Mass Uncertainty (amu)
Lorentz Factor
0.0
0.2
0.4
0.6
0.8
2.0
2.5
3.0
3.5
4.0
^{20}Ne
^{28}Si
^{56}Fe
^{28}Si
^{56}Fe

Chapter 3

Fragmentation Studies

Cosmic ray composition studies rely heavily on semi-empirical estimates of the cross-sections for the nuclear fragmentation reactions which alter the composition during propagation through the interstellar medium. In many cases the errors in these cross-section estimates result in significant uncertainties in cosmic ray source abundances or in propagation model parameters derived from observed abundances. To reduce these uncertainties, direct measurement of a wide range of nuclear fragmentation reactions would be desirable. In addition to measurements of key cross-sections which strongly influence the interpretation of particular cosmic ray data, other cross-section data are useful since they can be used as the basis for refining the semi-empirical formulae.

Accelerator calibrations of cosmic ray detectors provide a possible source of data for testing semi-empirical cross-section estimates. We have analyzed two sets of data obtained during calibrations in which ^{40}Ar and ^{56}Fe were fragmented in CH_2 targets, and have compared the observed isotope yields with those expected on the basis of the semi-empirical formulae. In this chapter we report on some of the differences between the measured and calculated yields.

We will first present a discussion of the importance of fragmentation cross-sections in section 1 of this chapter. Analysis and results on the ^{40}Ar and ^{56}Fe fragmentation studies are presented in sections 2 and 3. Section 4 gives a summary of the fragmentation studies.

3.1. Importance of Fragmentation Cross-Sections in Cosmic Rays Studies

The cross-sections of high-energy nuclear reactions are of considerable astrophysical interest. They are necessary for deducing cosmic-ray source abundances, inferring cosmic-ray propagation and confinement parameters, and many other areas of cosmic rays studies. We will discuss the importance of fragmentation cross-sections in some of these areas.

A good knowledge of cross-sections is essential for the determination of the mean path length in interstellar matter and the confinement time of cosmic rays in galactic magnetic fields before leaking out from the galaxy due to random walk of magnetic field lines and/or scattering by magnetic irregularities. The cosmic-ray path length distribution function can be estimated from various secondary/primary ratios such as ^{3}He/He, (Li+Be+B)/(C+N+O), and (Cl through Mn)/Fe. Here the secondaries are assumed to be the products from fragmentation reactions of the primaries with the interstellar medium, with negligible source contributions. To deduce the path length from these ratios, some knowledge of fragmentation cross-sections is necessary. Uncertainties in the fragmentation cross-sections will result in an uncertainty in the deduced path length. The path length distribution is essential for checking the various theories of cosmic-ray propagation and leakage from the Galaxy. Many of the secondary nuclei produced by cosmic ray fragmentation are unstable toward nuclear decay. Unstable isotopes with short (compared to the confinement time) half-lives may be treated as if their stable daughter(s) had been produced directly. On the other hand, isotopes with half-lives comparable to the cosmic ray confinement time can be used as clocks for measuring the confinement time. Radioactive isotopes such as ^{10}Be, ^{26}Al, ^{36}Cl, and ^{54}Mn are such cosmic clocks. However, in order to deduce the confinement time from the measured abundances, the production cross-sections for these isotopes must be known.

Fragmentation cross-sections are also necessary for other areas of cosmic rays studies. For example, they are useful for determining the production rates of various isotopes in meteorites or on the lunar surface due to bombardment by cosmic rays and high-energy solar particles. They are also useful for explaining the abundances of Li, Be, and B in the solar system.

One of the most important objectives in cosmic rays studies is to obtain the abundances of cosmic rays at their sources. Source abundances have important implications for the nucleosynthesis process occurring in the stars that ultimately produce the galactic cosmic rays. In particular, as pointed out by Woosley (1976), the isotopic composition of iron in primary cosmic rays carries valuable information about the site (or sites) of its production. In addition, because elements such as neon, magnesium, and silicon each has more than one relatively abundant isotope and because they may be produced by several nucleosynthetic processes, the isotopic abundances of these elements carry a great deal of information about the nucleosynthetic history of cosmic rays.

The observed cosmic-ray composition is modified from the source composition by passage through $\sim$6 gm/cm^2 of interstellar matter. This grammage is comparable to the interaction mean-free path of the nuclei involved so that a considerable fraction of them will interact and produce secondary nuclei. For the isotopes that are most abundant in the cosmic ray source, this secondary production will not greatly modify the relative abundances. However, for the less abundant isotopes, this secondary production will dominate over any residual source component at the observation site.

Therefore, propagation calculations must be performed to obtain the source abundances from the observed abundances. As pointed out by Hinshaw and Wiedenbeck (1983), as the resolution and statistical accuracy of cosmic ray element and isotope observations continue to improve, the contributions from the observational errors to the uncertainties of the deduced cosmic ray source abundances are becoming less significant. Consequently, source abundance errors are, in many cases, now dominated by uncertainties in the propagation calculations. The most important uncertainty in most cases is that due to errors in the partial cross-sections for the production of secondary nuclei by fragmentation reactions in the interstellar medium. In many cases, these uncertainties are significant enough that they forbid any meaningful measurement of source abundances for some of the isotopes. For example, Hinshaw and Wiedenbeck (1983) have found that the propagation errors do not presently permit a significant determination of a finite source abundance for the elements F, Cl, or Mn.

A formalism was developed by Stone and Wiedenbeck (1979) for deriving cosmic ray source abundances from observed local abundances using a essentially secondary nuclide such as ^{21}Ne, as a tracer of spallation production of associated nuclides, such as ^{20}Ne and ^{22}Ne, during propagation. Using this formalism, a significant reduction in the uncertainty in the calculated source abundance ratio can be realized if measurements are available for the ratios of production cross-sections. In other words, this formalism has reduced the necessity of measuring the partial cross-sections to only measuring the *relative* partial cross-sections for production of the tracer and the associated nuclides.

To properly interpret cosmic ray data, knowledge of a wide range of fragmentation cross-sections is necessary. Unfortunately, until recently, beams of high energy heavy nuclei have not been available and cross-sections have been deduced from the inverse process where stationary heavy nuclei have been bombarded by high energy protons. These measurements are tedious, and in spite of great effort by several groups, only a fraction of the relevent cross-sections have been measured. Using these cross-sections as a basis, a set of semi-empirical cross-section formulae covering all of the relevent reactions for the cosmic ray propagation problem, both elemental and isotopic, have been developed by Silberberg and Tsao (1973a,b and 1977a,b). In general, the uncertainties are about ±30% on both the elemental and isotopic cross-sections (Silberberg et al., 1983). This is inadequate to serve some of the present data on cosmic ray composition being obtained from balloon and satellite instruments. To reduce these uncertainties, laboratory measurement of a wide range of nuclear fragmentation reactions would be desirable. In addition to measurements of key cross-sections which strongly influence the interpretation of particular cosmic ray data, other cross-section data are also useful. Any systematic difference between the measurements and the semi-empirical estimates can be used as the basis for refining the semi-empirical formulae.

3.2. Fragmentation of ^{40}Ar

We have analyzed a set of data obtained during a calibration in which ^{40}Ar was fragmented in a CH_2 target. Observed isotope yields are compared with those expected on the basis of the Monte Carlo calculations. Although the fragmentation cross-sections of ^{40}Ar do not have great astrophysical significance, they do provide information for testing the semi-empirical formulae and parameters. Preliminary results of this work have been reported at the 18th International Cosmic Ray Conference (Lau, Mewaldt, and Wiedenbeck, 1983). In this section, we will report our work in more detail and improved results for K isotopes will be presented.

3.2.1. Experimental Setup

The experimental data reported here were obtained at the Lawrence Berkeley Laboratory Bevalac accelerator in April, 1981 during the calibration of a set of detectors for a cosmic ray mass spectrometer. Figure 3.1 shows a schematic diagram of the experimental setup. A 287 MeV/amu ^{40}Ar beam exited the Bevalac vacuum and impinged on a CH_2 target. The thickness of the CH_2 target was 1.75 inch (4.10 g/cm^2) at the beginning of the run and was changed to 0.75 inch (1.75 g/cm^2) during the later part of the run. A variable thickness Cu absorber, located ~10m upstream from the target, was used to "tune" the energy of the beam so as to adjust the ^{40}Ar stopping point. Because the Cu absorber is located far away from the detector stack, most of the fragmentation products form the interactions in the Cu will not be analyzed by the detectors. For our data set, the Cu thickness ranged from 0 to 2.20 g/cm^2. Excluding the interactions in the Cu, the interaction energy ranges from 90 MeV/amu to 280 MeV/amu with an average interaction energy of 208 MeV/amu. The detector stack was located ~2m downstream of the target behind a thin multiwire proportional counter

Figure 3.1

Schematic diagram of the experimental setup (not to scale) showing an ^{40}Ar nucleus breaking up into heavy (H) and light (L) fragments.

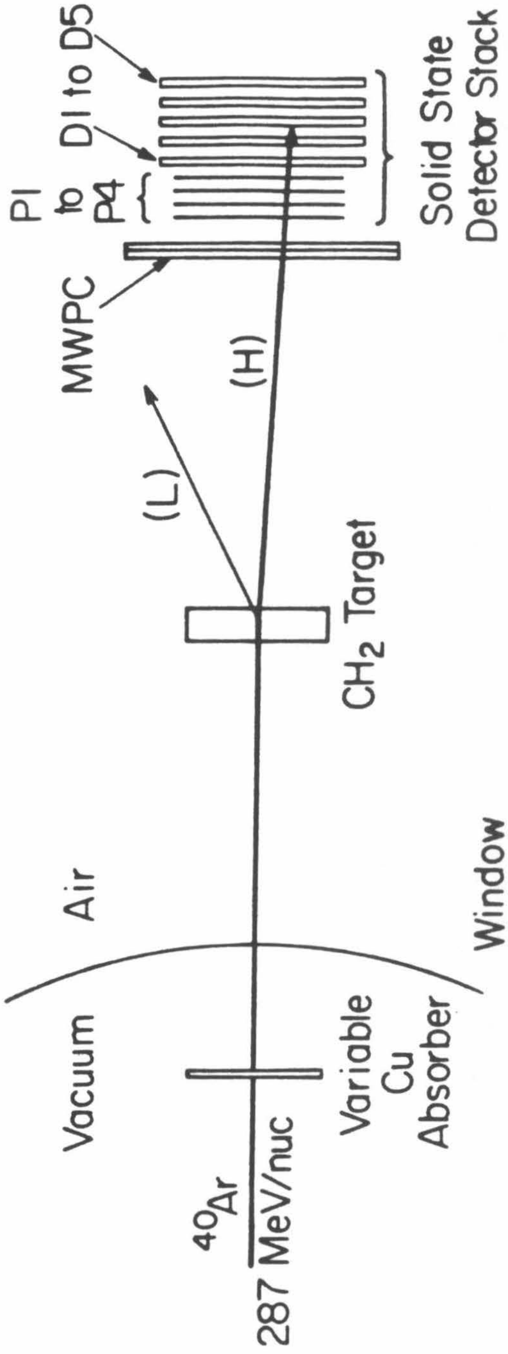
287 MeV/nuc
^{40}Ar
Vacuum
Variable
Cu
Absorber
Window
Air
CH_2 Target
(L)
(H)
MWPC
P1
to
P4
D1 to D5
Solid State
Detector Stack

(MWPC) used to select for analysis those events within the central 20 cm^2 of the detector stack. Table 3.1 is a list of the detectors which comprise the detector stack. The first four solid state detectors were thin (<0.11 g/cm^2 total) and were not used in the present analysis. The CH_2 target constituted the majority of the grammage in front of the D1 detector. Detectors D1 to D5 were large area Si(Li) devices, each 3 mm thick, except for D3, which was 5 mm thick.

Because the experimental setup was designed primarily for detector calibration purposes, there are some limitations to its use for cross-section measurements. There was no absolute measure of the number of ^{40}Ar hitting the target. In addition, because of the target thickness, the energy at which the interactions occurred is not well defined. Finally, fragments emitted at large angles to the beam were not detected; the data are limited to those within ~1° of the beam direction. On the other hand, with its excellent mass resolution, these data appear to be appropriate for measuring ***relative*** fragmentation yields. We have therefore adopted an analysis approach that takes advantage of this capability.

3.2.2. Analysis and Results

The outputs of detectors D1 to D4 were used to determine the charge (Z) and mass (M) of all heavy fragments stopping in D2 through D4. The technique for determining mass is similar to the dE/dx-E technique discussed by Stone (1974). For non-relativistic particles, the range-energy relationship can be approximated by a power law. The range, R, of a particle with charge Z, mass M, and total kinetic energy E, can be written as

$$R = \kappa \cdot \frac{M}{Z^2} \cdot \left[\frac{E}{M}\right]^{\alpha} \qquad (3.1)$$

Table 3.1

Detector	Detector Type	Nominal Thickness (μm of Si)	Dead Layer[a] (μm of Si)
M1	sb[b]	115	11
M2	sb	115	11
M3	sb	115	11
M4	sb	115	11
D1	Li-D[c]	3146	23
D2	Li-D	3123	24
D3	Li-D	4821	194
D4	Li-D	3121	25
D5	Li-D	3117	15

[a] deadlayer includes the air gap for each detector.

[b] surface-barrier detector

[c] Lithium-drifted detector

Table 3.1 Detector type, thickness, and dead layer thickness of the detectors which comprise the detector stack.

where κ is a proportionality constant and α is the index of the power law relationship. If the total energy E is measured by more than one detector, then the total energy can be separated into two parts : ΔE, the energy loss in the first detector, and E', the residual kinetic energy. In this case, another range-energy equation can be written

$$R - L = \kappa \cdot \frac{M}{Z^2} \cdot \left(\frac{E'}{M} \right)^{\alpha} \tag{3.2}$$

where L is the thickness of the ΔE device.

With only two equations and three unknowns (R, Z, M), the solution will not be unique. However, knowing that the mass M has to be close to twice the charge $2 \cdot Z$, we can determine R, Z, and M from equations (3.1) and (3.2). Instead of solving for Z and M one at a time, we will solve for another quantity which will give information on both. Rewriting the mass M as

$$M = 2 \cdot Z + \Delta M \tag{3.3}$$

equations (3.1) and (3.2) give

$$Z \cdot \left(1 + \frac{\Delta M}{2 \cdot Z} \right)^{\frac{\alpha-1}{\alpha+1}} = \left(\frac{\kappa}{L \cdot 2^{\alpha-1}} \right)^{\frac{1}{\alpha+1}} \cdot \left(E^{\alpha} - E'^{\alpha} \right)^{\frac{1}{\alpha+1}}. \tag{3.4}$$

The left hand side of equation (3.4) is the quantity we are looking for which gives information on both Z and M. Let's call this quantity Z' so that

$$Z' = \left(\frac{\kappa}{L \cdot 2^{\alpha-1}} \right)^{\frac{1}{\alpha+1}} \cdot \left(E^{\alpha} - E'^{\alpha} \right)^{\frac{1}{\alpha+1}} \tag{3.4'}$$

and Z' can be approximated as follows

$$Z' = Z \cdot \left(1 + \frac{\Delta M}{2 \cdot Z} \right)^{\frac{\alpha-1}{\alpha+1}} \approx Z \cdot \left[1 + \frac{\alpha-1}{\alpha+1} \cdot \frac{\Delta M}{2 \cdot Z} \right]$$

$$\approx Z + \frac{1}{2} \cdot \frac{\alpha-1}{\alpha+1} \cdot \Delta M \tag{3.5}$$

For $\alpha = 1.78$,

$$Z' \approx Z + 0.14 \cdot \Delta M. \tag{3.5'}$$

For isotopes with $M = 2 \cdot Z$, Z' is the same as Z; and for isotopes with higher mass, Z' will be slightly higher. When ΔM is large (>6), Z' will run into the next charge. However, the yields for the high ΔM isotopes are so small that this does not create a problem for us.

Equations (3.1) and (3.2) can also be used to calculate the range of the particle (where R is measured from the beginning of the ΔE detector)

$$R = \frac{L \cdot E^{\alpha}}{E^{\alpha} - E'^{\alpha}}. \tag{3.6}$$

To use one range scale for particles stopping at different places in the detector stack, the range, R, is redefined as the distance from the beginning of detector D1 to where the particle stopped. Thus equation (3.6) becomes

$$R = R_o + \frac{L \cdot E^{\alpha}}{E^{\alpha} - E'^{\alpha}}. \tag{3.6'}$$

Figure 3.2 shows a cross plot of Z' and R for particles stopped in the detector D2, which demonstrates that Z' carries information on both Z and M. The normalization of the tracks can be done by adjusting the proportionality constant κ (this plot is not perfectly normalized). The flatness (slopes) of the tracks can be adjusted by adjusting the index α. Here α is 1.78. Notice that $Z = 19$ events can be seen on this plot. The tracks are not straight at the beginning of the range. This is caused by the finite dead layer thickness between D1 and D2. This effect will be worse when the dead layer is thicker which is the case between D3 and D4.

Figure 3.2

Cross plot of Z′ and R as calculated from equations (3.4) and (3.6) for particles stopped in detector D2. The normalization of the tracks can be done by adjusting the proportionality constant κ (this plot is not perfectly normalized). The flatness (slopes of the tracks) of the tracks can be adjusted by adjusting the index α. Here α is 1.78. Notice that Z = 19 events can be seen on this plot. The tracks are not straight at the beginning of the range. This is caused by the finite dead layer thickness between D1 and D2. We have defined R = 0 at the front of D1 detector.

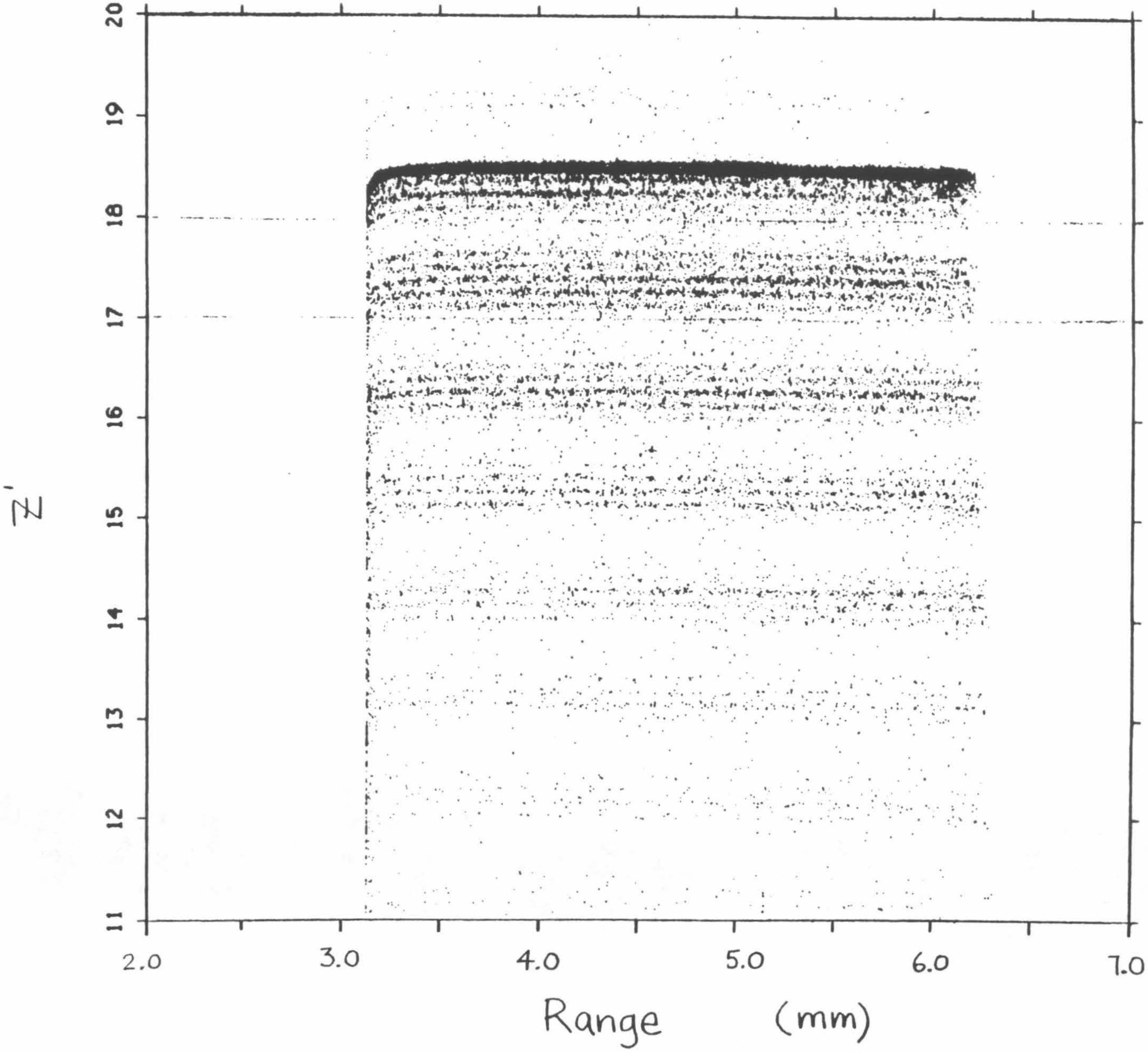
Z'
20
19
18
17
16
15
14
13
12
11
2.0
3.0
4.0
5.0
6.0
7.0
Range (mm)

3.2.2.1. Dead Layer Correction

In order to maximize the utilization of the detectors, we would like to make the tracks straight at the beginning of the range. One way to make this correction is to estimate the amount of undetected energy loss in the dead layer ΔE_d. Consider the situation shown in figure 3.3. We can write down three range-energy relations using equation (3.1). For the residual energy detector, we have

$$R' = \kappa \cdot \frac{M}{Z^2} \cdot \left[\frac{E'}{M}\right]^{\alpha}. \tag{3.7}$$

Starting from the beginning of the dead layer, we have

$$R' + D = \kappa \cdot \frac{M}{Z^2} \cdot \left[\frac{E' + \Delta E_d}{M}\right]^{\alpha} \tag{3.8}$$

where D is the thickness of the dead layer; and from the beginning of the ΔE detector, we have

$$R' + L = \kappa \cdot \frac{M}{Z^2} \cdot \left[\frac{E' + \Delta E_d + \Delta E}{M}\right]^{\alpha}. \tag{3.9}$$

We would like to eliminate all the unknowns (R', M, Z, etc.) from equations (3.7) through (3.9) and get an expression with only ΔE_d and other known or measured quantities. Solving equations (3.7) through (3.9) simultaneously, we get

$$\frac{D}{L} = \frac{(E' + \Delta E_d)^{\alpha} - E'^{\alpha}}{(E' + \Delta E_d + \Delta E)^{\alpha} - E'^{\alpha}}. \tag{3.10}$$

If we let $E' + \Delta E_d + \Delta E = E$, we can rewrite equation (3.10) as

$$F(E) = \frac{D}{L} \cdot E^{\alpha} + \left(1 - \frac{D}{L}\right) \cdot E'^{\alpha} - (E - \Delta E)^{\alpha} = 0. \tag{3.11}$$

We can solve equation (3.11) for E using the Newton-Ralphson method (see

Figure 3.3

Schematic configuration for the dead layer correction. The undetected energy loss in the dead layer, ΔE_d, is estimated from the measured energy losses E′ and ΔE using equation (3.11).

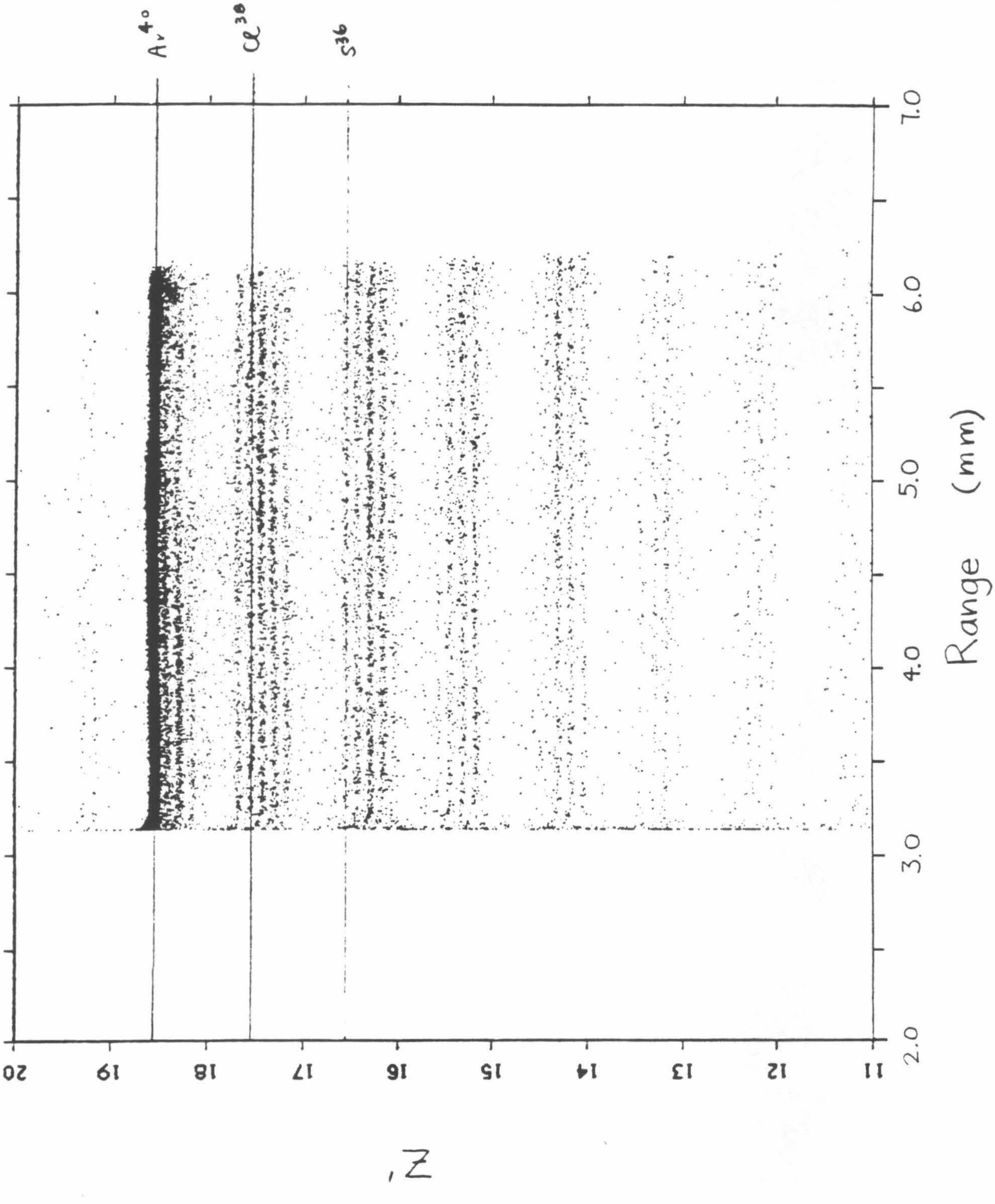
Ar⁴⁰
Cl³⁸
S³⁶
Range (mm)
2.0
3.0
4.0
5.0
6.0
7.0
Z'
20
19
18
17
16
15
14
13
12
11

for example Dahlquist, 1974). This quantity E is the total energy which includes the energy loss within the dead layer. This quantity is used as E in both equations (3.4') and (3.6') and the quantity $(E-\Delta E)$ is used as E' in these equations. Figure 3.4 shows a cross plot of Z' and R for particles which stopped in detector D2 with the dead layer correction applied. This correction is more significant when the thickness of the dead layer is large.

Now we have corrected for the energy deficit in the ΔE detector. However, there is another energy deficit if the particle penetrates the active part of the residual energy detector and yet does not have enough energy loss to trigger the next detector. If we ignore this energy deficit and calculate R and Z', both calculated values will be smaller than they should be. The greater the energy deficit, the greater effect it will have on these calculated values. We can see evidence of these penetrating events in figure 3.4; it is particularly obvious at the end of range for the ^{40}Ar track. We call this effect "foldback". There is no easy way to distinguish these events from the lower mass events stopping earlier in the detector. To eliminate "foldback" events, we restrict the range, R, on the $R-Z'$ plot so that no "foldback" event will be included in our analysis. The cost of doing this is loss of analysis range in addition to the range which we have already lost due to the dead layers of the detectors. Nevertheless, this is much better than introducing misidentified events in our analysis. Table 3.2 gives the analyzable range of our analysis. Events which stopped outside of the analyzable range were not included in our analysis. There were $262\mu m$ (between D2 and D3) and $998\mu m$ (between D3 and D4) of range not analyzed between detectors. The number of particles, which stopped in each of these non-analyzed ranges, was estimated for each of the isotopes from the range profile of that particular isotope.

Figure 3.4

Cross plot of Z′ and R for particles stopped in detector D2 with the dead layer correction applied.

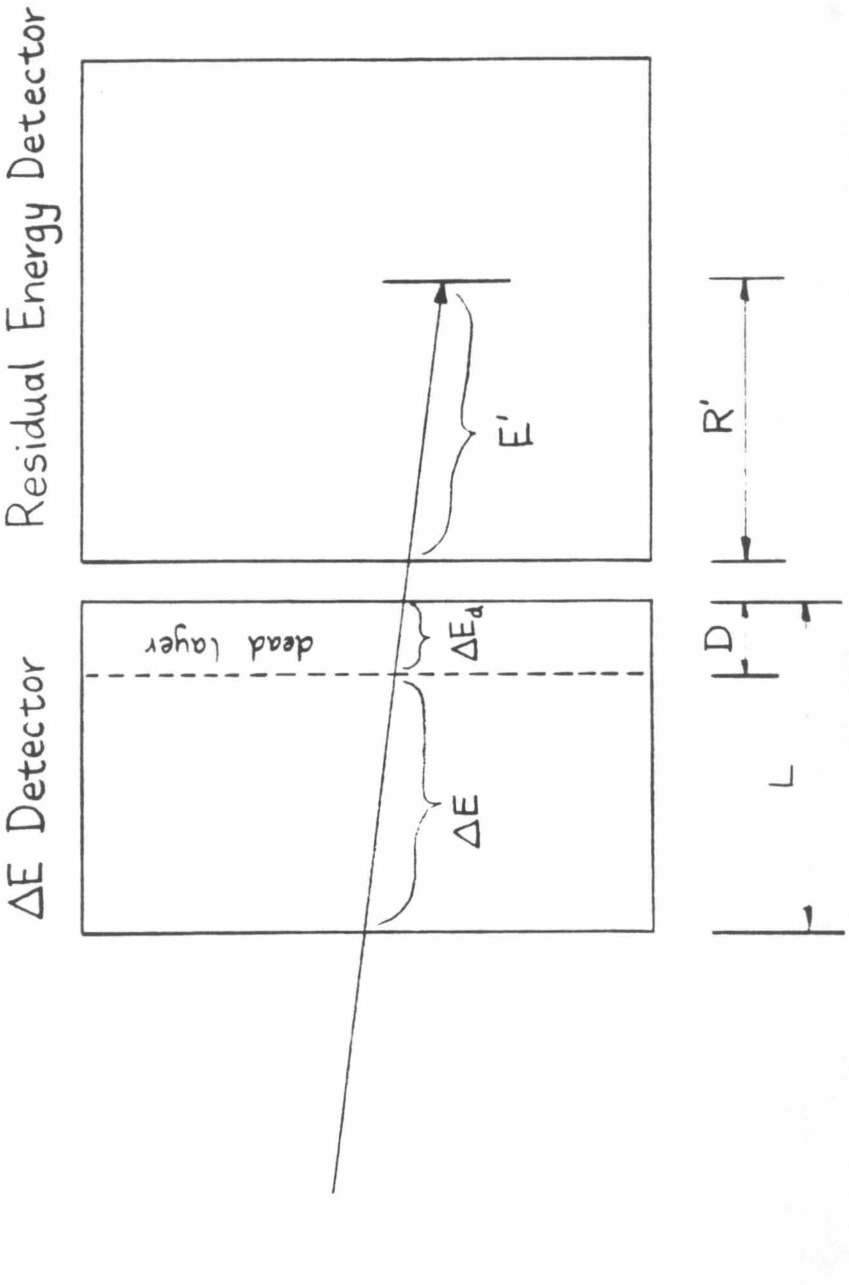
Residual Energy Detector
ΔE Detector
dead layer
E'
ΔE_d
ΔE
R'
D
L

Table 3.2

Range for Detectors D2 through D4 (μm)

Detector	Available		Analyzable	
	min.	max.	min.	max.
D2	3146	6269	3200	6038
D3	6269	11090	6300	10152
D4	11090	14211	11150	13976

Table 3.2 Available and analyzable range for detectors D2 through D4.

3.2.2.2. Range Correction

Notice in figure 3.4 that the range calculation is not perfect (the isotope tracks do not terminate at the same place) because the range-energy relationships do not follow Z^2/A exactly. We have put in a Z dependent scale factor in our analysis so that the end of range comes out to where it should be for all the isotope tracks. The range is scaled so that the isotope tracks stop at the maximum range (as listed in Table 3.2) less the dead layer (as listed in Table 3.1), for each of the detectors. This is done to make the analysis range the same for all the isotopes.

3.2.2.3. Mass Consistency Check

For particles stopping in detectors D3 and D4, more than one Z' can be calculated. For example, if the particle stopped in D3, one Z' can be calculated using D2 as the ΔE detector and another Z' can be calculated using D1 as the ΔE detector. Similarly, particles stopping in D4 can have two Z's calculated, one using D3 and the other one using D2 as the ΔE detector. In our analysis, whenever two Z's can be calculated, we required the two Z's to agree within 1%. For $Z = 18$ particles, this translates into approximately 0.18 charge unit, or 1.3 amu. This mass consistency requirement rejected about 3% of the events in our analysis. Most of these rejected events were those which interacted in the detector stack. Note that there is no mass consistency check for events stopping in detector D2.

3.2.2.4. Data Set Selection

For our analysis, we have selected subsets of the data where almost all fragments of interest stopped in the detectors which give good mass analysis (D2 through D4). When the data was taken, the thickness of the Cu absorber was systematically varied with time to obtain a distribution of ranges for the non-interacted ^{40}Ar particles within the detector stack. Therefore, we can select the data to have the non-interacted ^{40}Ar particles stopping in a particular range by specifying the time interval which the data was taken. By selecting the range of the non-interacted ^{40}Ar particles, we are indirectly specifying the restrictions on the range of the other isotopes. Before the selection criteria on the ^{40}Ar can be specified, we need to know the relationships of the range of the different isotopes as a function of the range of non-interacted ^{40}Ar. Figure 3.5 shows this kind of relationship for ^{28}Si, ^{31}Si, ^{30}P, ^{35}P, ^{33}S, ^{37}S, ^{35}Cl, ^{39}Cl, ^{39}K, and ^{40}K. In deriving these relationships, we assume that the fragments have the same energy per nucleon as the primary particle right after the interaction, and that range scales as A/Z^2. In figure 3.5, each plot shows the possible range of the isotope with the two lines being the limiting cases. One limiting case has the ^{40}Ar beam particles interacting upstream at the front the Cu absorber. The other limiting case has the ^{40}Ar beam particles interacting just before they entered detector D1.

In this study, we will compare the observed and calculated yields of the elements ranging from Mg to K ($12 \leq Z \leq 19$). It is impossible to choose one subset of the data with all of the fragments of interest stopping in the detectors D2 through D4. We will select three data subsets: data subset 1 will have all the fragments of Mg through S ($12 \leq Z \leq 16$) stopping in D2 through D4, data subset 2 will have all the fragments of P through Cl ($15 \leq Z \leq 17$) stopping in D2 through D4, and data subset 3 will have all the fragments of S through K ($16 \leq Z \leq 19$) stopping in D2 through D4. To select the data subsets, we will look at the isotopes with longest and shortest ranges in each of the data subsets. In data subset 1, the isotope with the longest range is ^{28}Mg. However, if all of the Mg and Al fragments are required to

Figure 3.5

The range of isotopes (a) ^{28}Si and ^{31}Si, (b) ^{30}P and ^{35}P, (c) ^{33}S and ^{37}S, (d) ^{35}Cl and ^{39}Cl, and (e) ^{39}K and ^{40}K as a function of the non-interacted ^{40}Ar particles. Each plot shows the possible range of the isotope with the two lines representing the limiting cases. One limiting case has the ^{40}Ar beam particles interacting upstream at the front end of the Cu absorber. The other limiting case has the ^{40}Ar beam particles interacting just right before they entered detector D1.

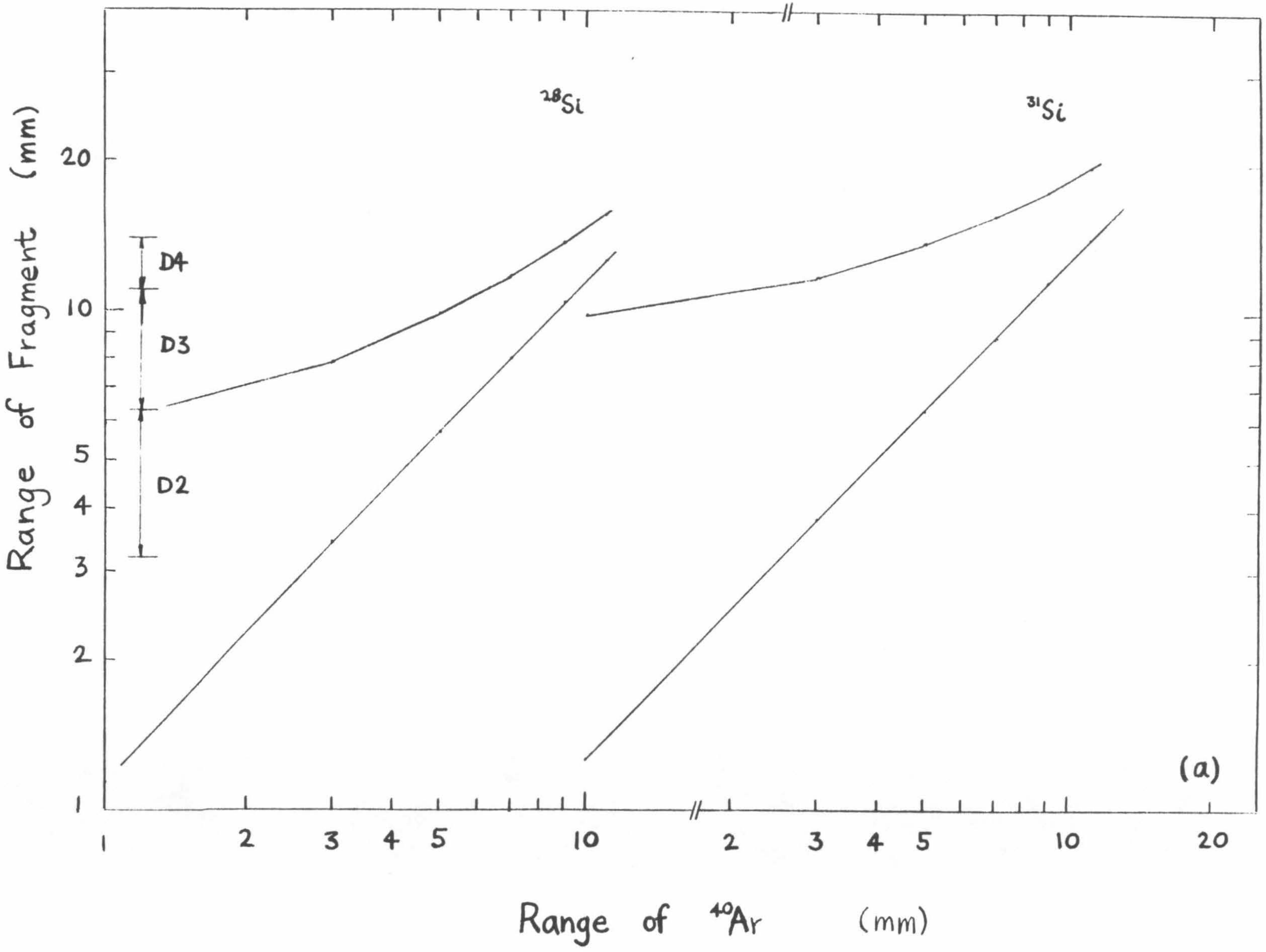
^{28}Si
^{31}Si
D4
D3
D2
(a)
Range of Fragment (mm)
1
2
3
4
5
10
20
Range of ^{40}Ar (mm)
1
2
3
4
5
10
2
3
4
5
10
20

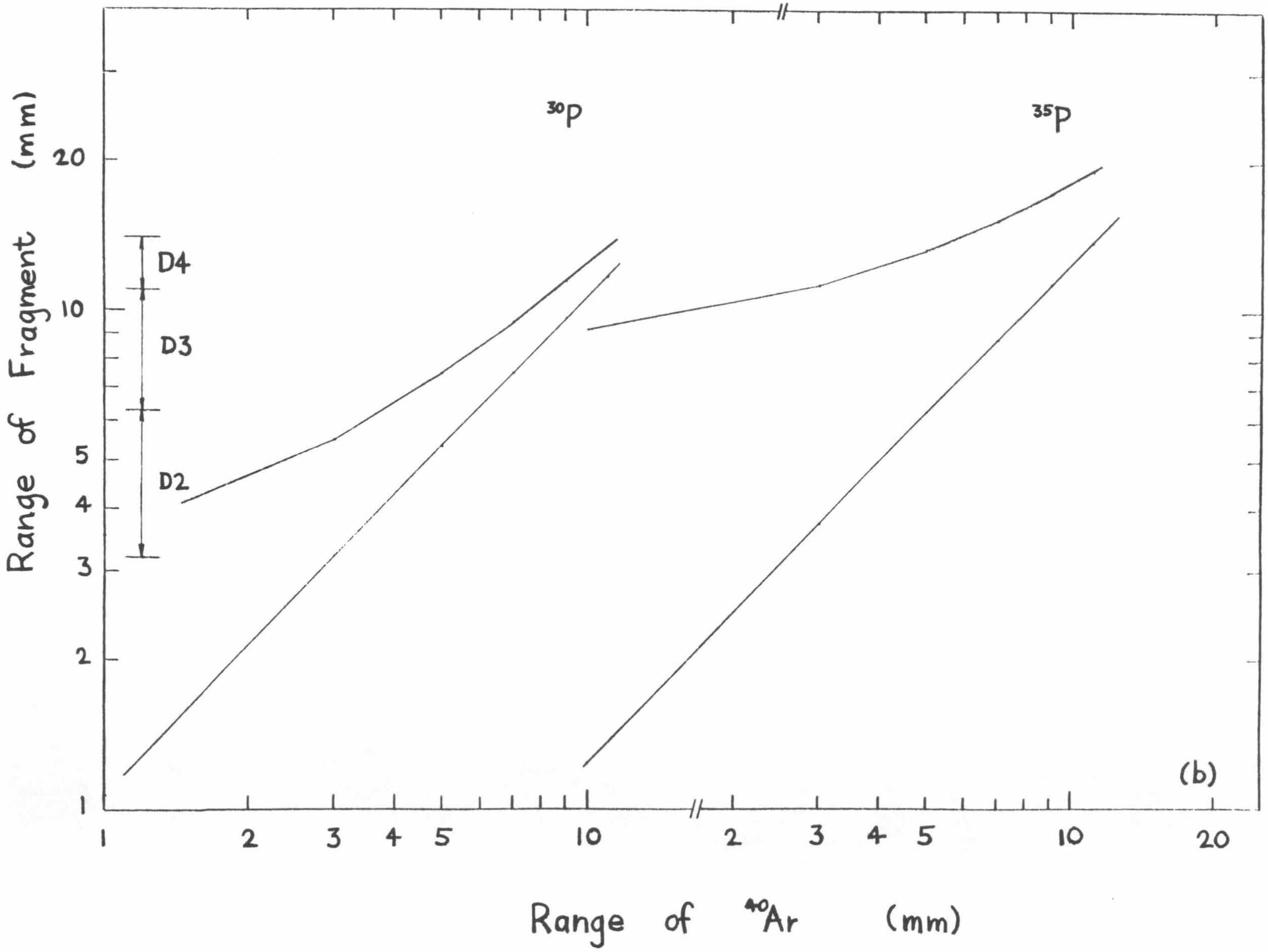

^{30}P
^{35}P
D4
D3
D2
(b)
Range of Fragment (mm)
1
2
3
4
5
10
20
1
2
3
4
5
10
2
3
4
5
10
20
Range of ^{40}Ar (mm)

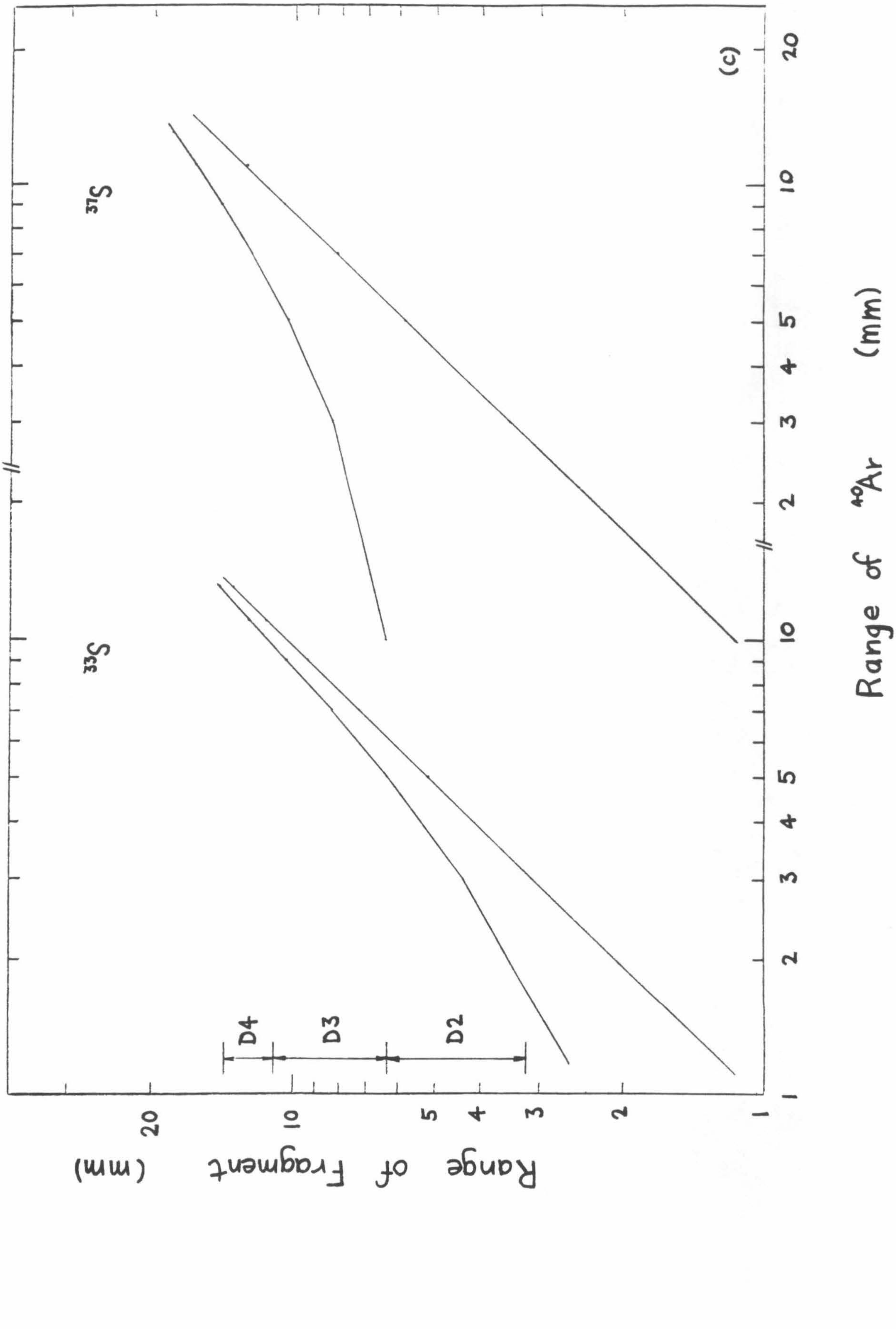
(c)
^{37}S
^{33}S
D4
D3
D2
1
2
3
4
5
10
20
Range of Fragment (mm)
1
2
3
4
5
10
2
3
4
5
10
20
Range of ^{40}Ar (mm)

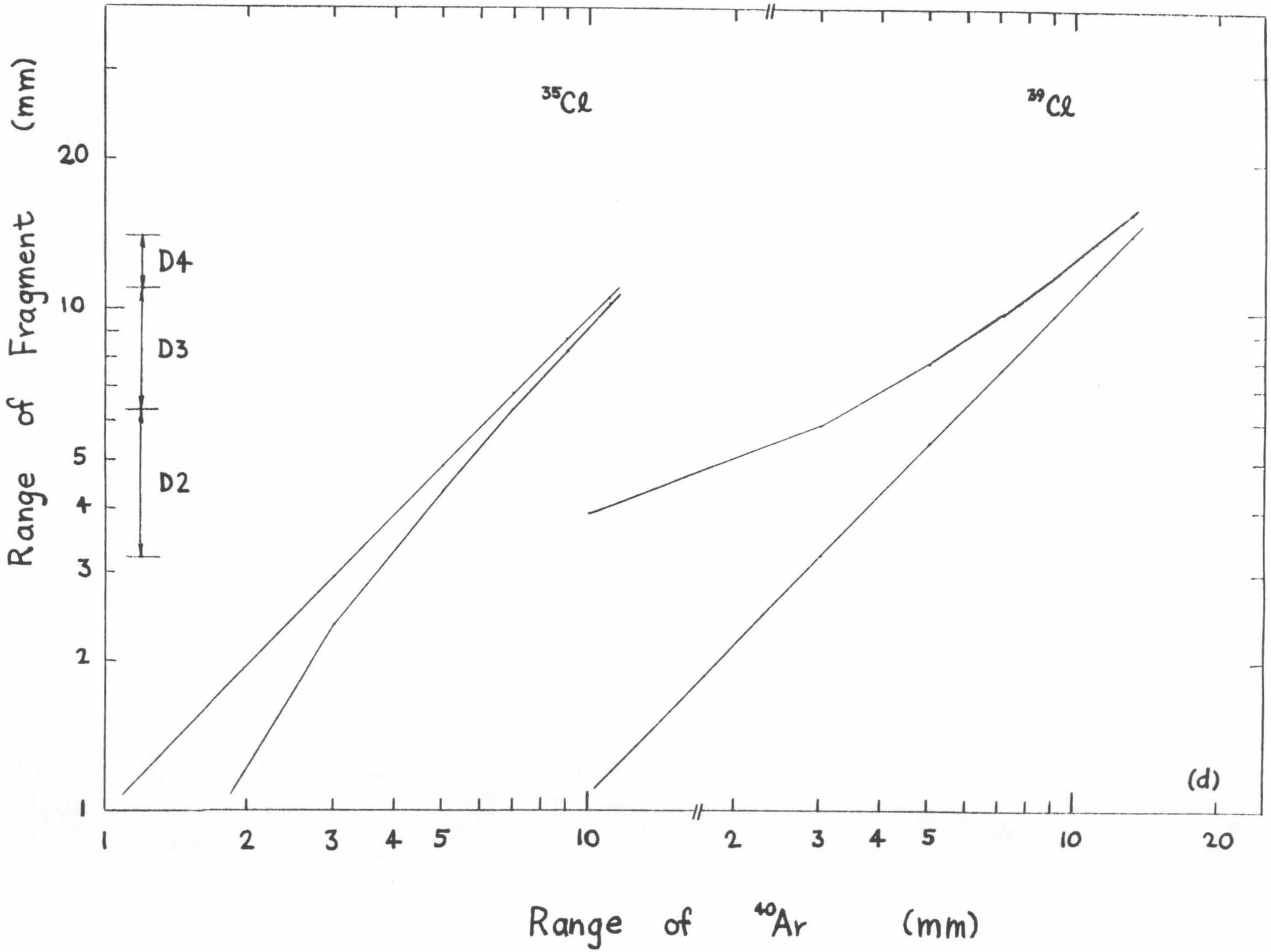
^{35}Cl
^{39}Cl
D4
D3
D2
(d)
Range of Fragment (mm)
1
2
3
4
5
10
20
Range of ^{40}Ar (mm)
1
2
3
4
5
10
2
3
4
5
10
20

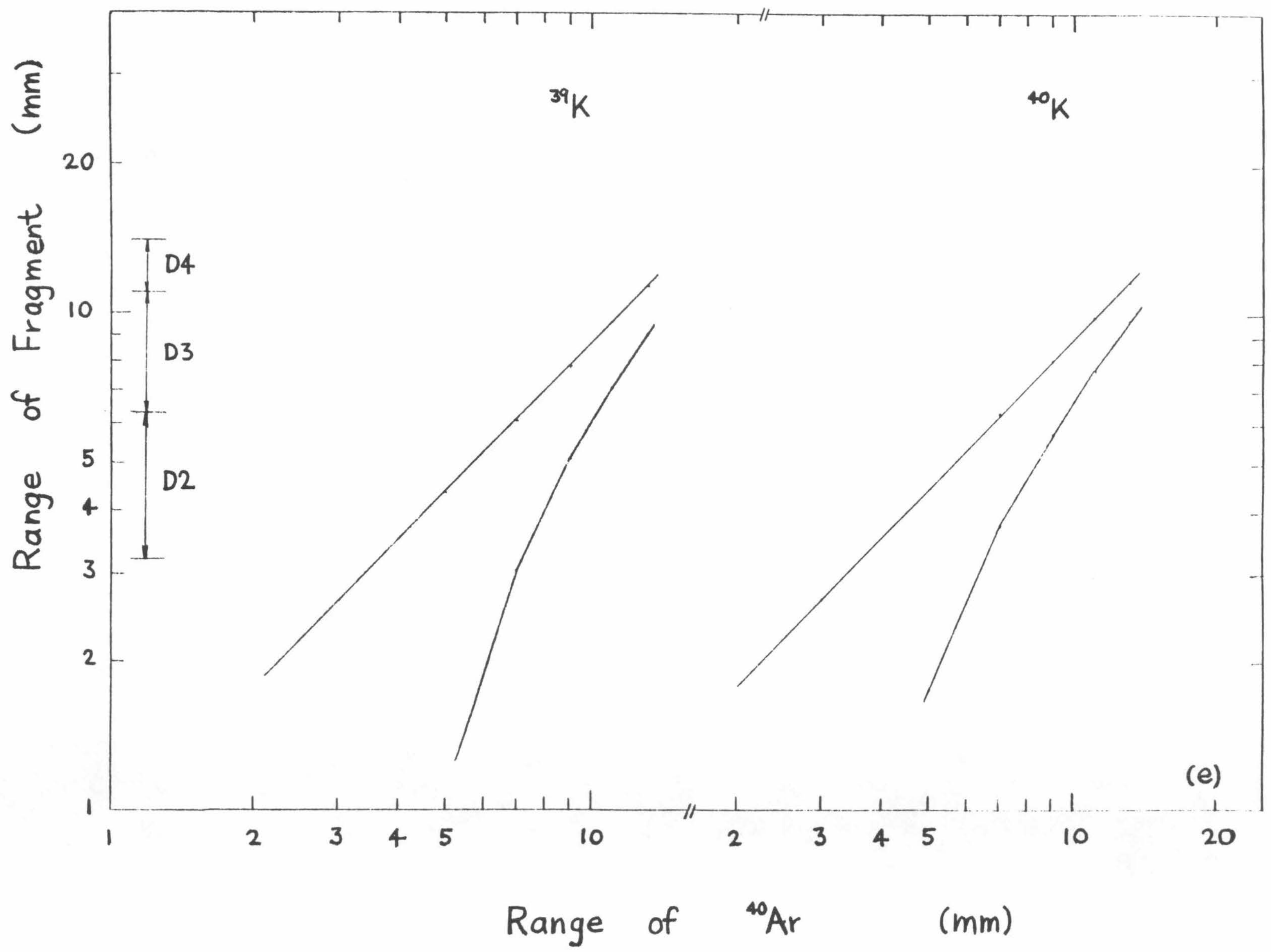
Range of Fragment (mm)
20
10
5
4
3
2
1
D4
D3
D2
^{39}K
^{40}K
(e)
1
2
3
4
5
10
2
3
4
5
10
20
Range of ^{40}Ar (mm)

stop within the analyzable range, the restrictions on the ^{40}Ar beam particles will be very stringent. Instead, ^{31}Si will be used to obtain the restriction on the ^{40}Ar range; and the observed yields of the Mg and Al fragments will be corrected based on the fractions of events, which are predicted by the Monte Carlo calculation to stop beyond the analyzable range of D4. Using figure 3.5a, the ^{40}Ar beam particles must stop with range less than 5200μm if we want all ^{31}Si fragments to stop before exiting D4. The isotope with the shortest range is ^{33}S (ignoring ^{32}S since it does not have a significant contribution). Using figure 3.5c, the ^{40}Ar beam particles must stop with range greater than 3100μm if we want all ^{33}S fragments to stop after they entered D2. Using this analysis we have restricted the first data subset to have the ^{40}Ar beam particles to stop with range greater than 3100μm and less than 5200μm. Doing similar analysis (using ^{35}P and ^{35}Cl for the second data subset and using ^{37}S and ^{39}K for the third data subset), the ^{40}Ar beam particles were restricted to have, range greater than 3900μm and less than 5600μm for the second data subset, and range greater than 7100μm and less than 8600μm for the third data subset.

3.2.2.5. Observed Isotope Yields

Mass and charge distributions, for particles stopping in a particular detector, can be obtained from a "mass" (Z') histogram of that detector with the dead layer correction and range restriction mentioned above. Such histograms can then be used to obtain the relative yields of the different isotopes from the fragmentation of ^{40}Ar. Figure 3.6 shows such a histogram which gives charge and mass distributions of elements from Ne through K stopping in detector D3 (this histogram contains all the range 3 data in the entire data set). Note that up to seven isotopes of each element can be identified. The observed mass resolution (rms) is ≤0.2 amu.

Figure 3.6

Mass histogram (for events stopped in detector D3) showing charge and mass distributions of elements from Ne through K resulting from the breakup of ^{40}Ar. The mass (in amu) of selected isotopes is labeled. The observed mass resolution (rms) is ≤ 0.2 amu. The ^{40}Ar peak extends to >12,000 events/bin. Note the ^{39}K and ^{40}K events to the right of the ^{40}Ar.

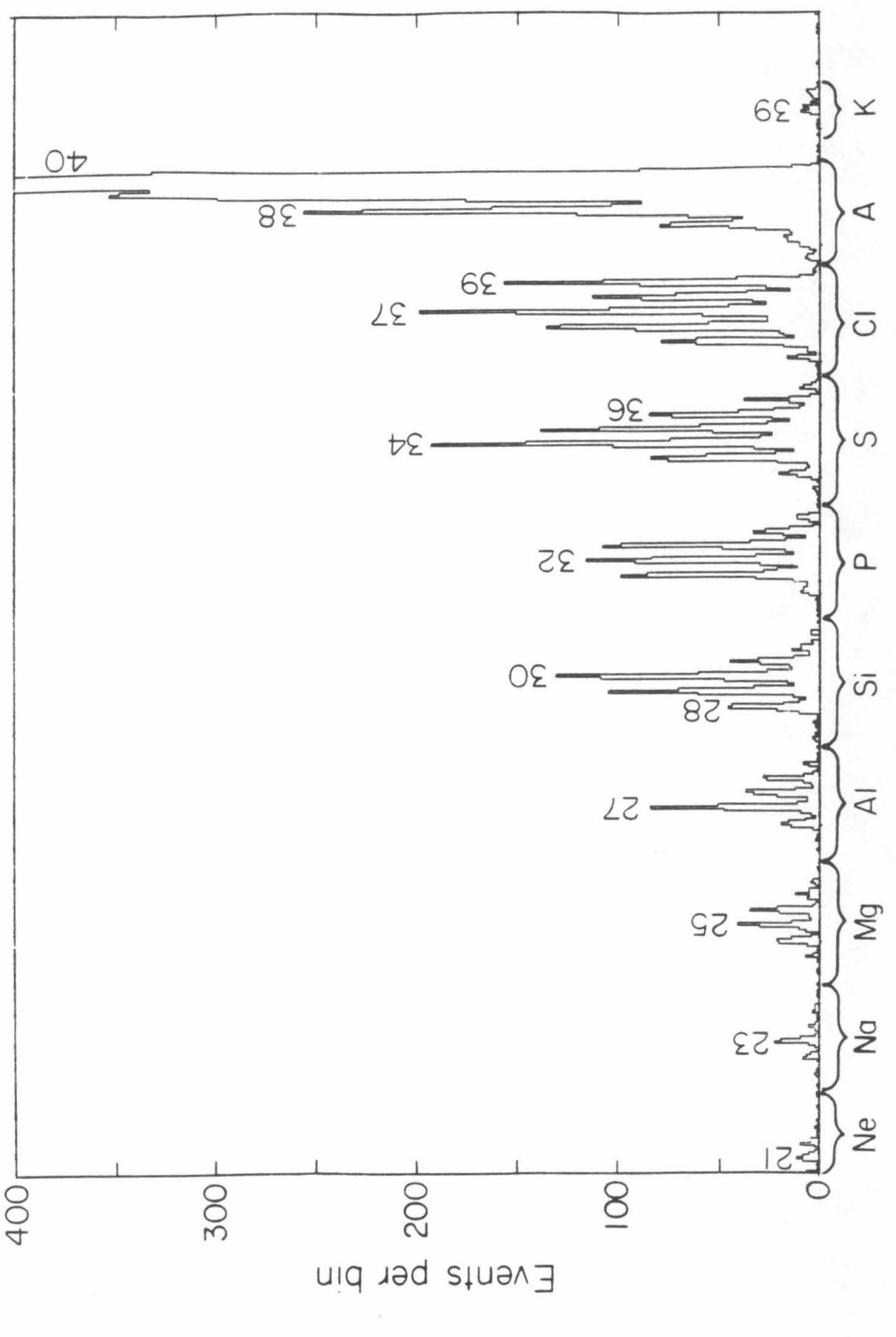
Events per bin
0
100
200
300
400
Ne
Na
Mg
Al
Si
P
S
Cl
A
K
21
23
25
27
28
30
32
34
36
37
39
38
40
39

The number of fragments observed for each isotope is obtained from "mass" histograms similar to the one shown in figure 3.6. "Mass" histograms were generated for each of the detectors (D2 through D4) and for each of the data subsets. The number of each of the isotopes is obtained by counting the number of events which fall into the ±0.5 amu mass range from the peak. This method is acceptable for most of the isotopes (with exception of the Ar isotopes) because of the good mass resolution. For the Ar isotopes, this is not acceptable, because the number of ^{40}Ar is so high, and an alternative method was used in which yields of the Ar isotopes are obtained by a least-squares fit with gaussian distributions to the "mass" histograms.

From the mass histograms, we can obtain the numbers of isotopes which stopped in the range where mass analysis is permitted. However, this excludes 262 μm between D2 and D3, and 998 μm between D3 and D4, due to dead layers and the "foldback" effect. In order to estimate the number of events, for each isotope, which stopped in the non-analyzable ranges, we plot the range distributions of each isotope in all three detectors. The number of isotopes, which stopped in the range not covered by the three range distributions, is estimated by drawing smooth curves to connect the three distributions.

Tables 3.3a-c gives the observed isotope yields for the three data subsets. The tables contain the measured isotope yields along with the estimates for fragments which stopped in the non-analyzed ranges. The uncertainties in the "total" columns contain statistical uncertainties only. Before comparing the observed yields with the calculated yields, the three observed yield tables (3.3a-c) should be consolidated into one single observed yield table. This can be done by normalizing the three data subsets. The second data subset will be normalized to the first data subset using the total

Table 3.3a

Isotope	Analyzable Range	Non-anal. Range [a]	Total	Element Total
^{38}S	11	--	11±3	1249±37
^{37}S	50	2	52±7	
^{36}S	147	10	157±13	
^{35}S	241	32	273±18	
^{34}S	404	45	449±22	
^{33}S	223	13	236±16	
^{32}S	71	--	71±8	
^{35}P	18	--	18±4	672±27
^{34}P	58	1	59±8	
^{33}P	151	11	162±13	
^{32}P	213	16	229±16	
^{31}P	159	11	170±13	
^{30}P	32	2	34±6	
^{32}Si	26	3	29±6	561±25
^{31}Si	66	11	77±9	
^{30}Si	199	18	217±15	
^{29}Si	153	12	165±13	
^{28}Si	68	5	73±9	
^{30}Al	9[b]	1	11±4[c]	273±18
^{29}Al	38	5	43±7	
^{28}Al	63	12	75±9	
^{27}Al	99	13	112±11	
^{26}Al	28	4	32±6	
^{27}Mg	12[b]	2	16±5[c]	170±14
^{26}Mg	44[b]	6	52±8[c]	
^{25}Mg	60	9	69±9	
^{24}Mg	29	4	33±6	

[a] Estimated number of fragments which stopped in the non-analyzed range (262 μm between D2 and D3, and 998 μm between D3 and D4).

[b] lower limit -- some of the fragments stopped beyond the analyzable range of the detector D4.

[c] Corrections are applied (to obtain the total yields), based on the fraction of events, predicted by the Monte Carlo calculation, which stop beyond the analyzable range of D4. For ^{30}Al, ^{27}Mg, and ^{26}Mg, the sums of columns 2 and 3 are divided by factors of 0.93, 0.89, and 0.96 respectively to give the total numbers in column 4.

Table 3.3a Observed isotope yields of the first data subset along with the estimates for fragments which stopped in the non-analyzed ranges. Uncertainties are statistical only and are based on the square root of the number of events observed.

Table 3.3b

Isotope	Analyzable Range	Non-anal. Range[a]	Total	Element Total
^{39}Cl	198	26	224±16	1243±36
^{38}Cl	199	23	222±16	
^{37}Cl	344	16	360±19	
^{36}Cl	253	--	253±16	
^{35}Cl	154	--	154±12	
^{34}Cl	24[b]	--	30±6[c]	
^{38}S	7	--	7±3	813±30
^{37}S	35	1	36±6	
^{36}S	90	4	94±10	
^{35}S	150	22	172±14	
^{34}S	259	38	297±18	
^{33}S	144	12	156±13	
^{32}S	51	--	51±7	
^{35}P	10	--	10±3	468±22
^{34}P	37	3	40±7	
^{33}P	109	5	114±11	
^{32}P	148	15	163±13	
^{31}P	108	10	118±11	
^{30}P	21	2	23±5	

[a] Estimated number of fragments which stopped in the non-analyzed range (262 μm between D2 and D3, and 998 μm between D3 and D4).

[b] lower limit -- some of the ^{34}Cl stopped beyond the analyzable range of detector D4.

[c] A correction is applied (to obtain the total yields), based on the fraction of events, predicted by the Monte Carlo calculation, which stop beyond the analyzable range of D4. The sum of columns 2 and 3 is divided by a factor of 0.80 to give the total number in column 4.

Table 3.3b Observed isotope yields of the second data subset along with the estimates for fragments which stopped in the non-analyzed ranges. Uncertainties are statistical only and are based on the square root of the number of events observed.

Table 3.3c

Isotope	Analyzable Range	Non-anal. Range [a]	Total	Element Total
^{40}K	16	1	17±4	41±7
^{39}K	22	2	24±5	
^{39}Ar	458	53	511±24	1004±33
^{38}Ar	291	34	325±19	
^{37}Ar	119	7	126±12	
^{36}Ar	36	6	42±7	
^{39}Cl	144	40	184±15	1087±36
^{38}Cl	118	40	158±15	
^{37}Cl	257	65	322±20	
^{36}Cl	238	37	275±18	
^{35}Cl	116	9	125±12	
^{34}Cl	22	1	23±5	
^{38}S	6	--	6±2	697±29
^{37}S	19	4	23±5	
^{36}S	74	15	89±10	
^{35}S	121	26	147±13	
^{34}S	218	42	260±18	
^{33}S	112	20	132±12	
^{32}S	36	4	40±7	

[a] Estimated number of fragments which stopped in the non-analyzed range (262 μm between D2 and D3, and 998 μm between D3 and D4).

Table 3.3c Observed isotope yields of the third data subset along with the estimates for fragments which stopped in the non-analyzed ranges. Uncertainties are statistical only and are based on the square root of the number of events observed.

number of S and P fragments. There are 1921 and 1281 fragments of S and P in the first and second data subsets respectively. Therefore, the results of the second data subset should be scaled by a factor of 1.500 to normalize them to the first data subset. Similarly, the third data subset will be normalized to the second data subset using the total number of Cl and S fragments. There are 2056 and 1784 fragments of Cl and S in the second and third data subsets respectively. Therefore, the results of the third data subset should be scaled by a factor of 1.152 to normalize them to the second data subset. In other words, the results of the third data subset can be scaled by a factor of 1.728 to normalize them to the first data subset. These normalized observed yields will be presented later along with the calculated yields.

3.2.2.5.1. Comparison with Viyogi et al.

Viyogi et al. (1978) measured the isotope distributions for peripheral reactions induced by ^{40}Ar at 213 MeV/nucleon. We have compared their observed relative isotope yields (deduced from their measured cross-sections) of the elements Mg through S with our results. Their observed yields were normalized to ours using the total number of events in each of the five cases. Figure 3.7 shows the comparisons. Their measurements were done with a 400 mg/cm^2 thick carbon target. Even though their target is different from ours (we calculate that >40% of our interactions are with H), the comparisons show excellent agreement for the relative isotope yields between the two sets of measurements. This suggests that the relative isotope yields do not depend strongly on the target material.

Figure 3.7

Comparision of our observed isotope yields with the isotope distributions measured by Viyogi et al. (1978) for the elements (a) S, (b) P, (c) Si, (d) Al, and (e) Mg. Their measurements were made with 213 MeV/nucleon ^{40}Ar beam bombarded with a carbon target with a thickness of 400 mg/cm^2. Their observed relative yields are deduced from their measured cross-sections and are normalized to our observed yields using the total number of events in each case. Even though their target is different from ours, the comparisions show excellent agreement for the two sets of measurements.

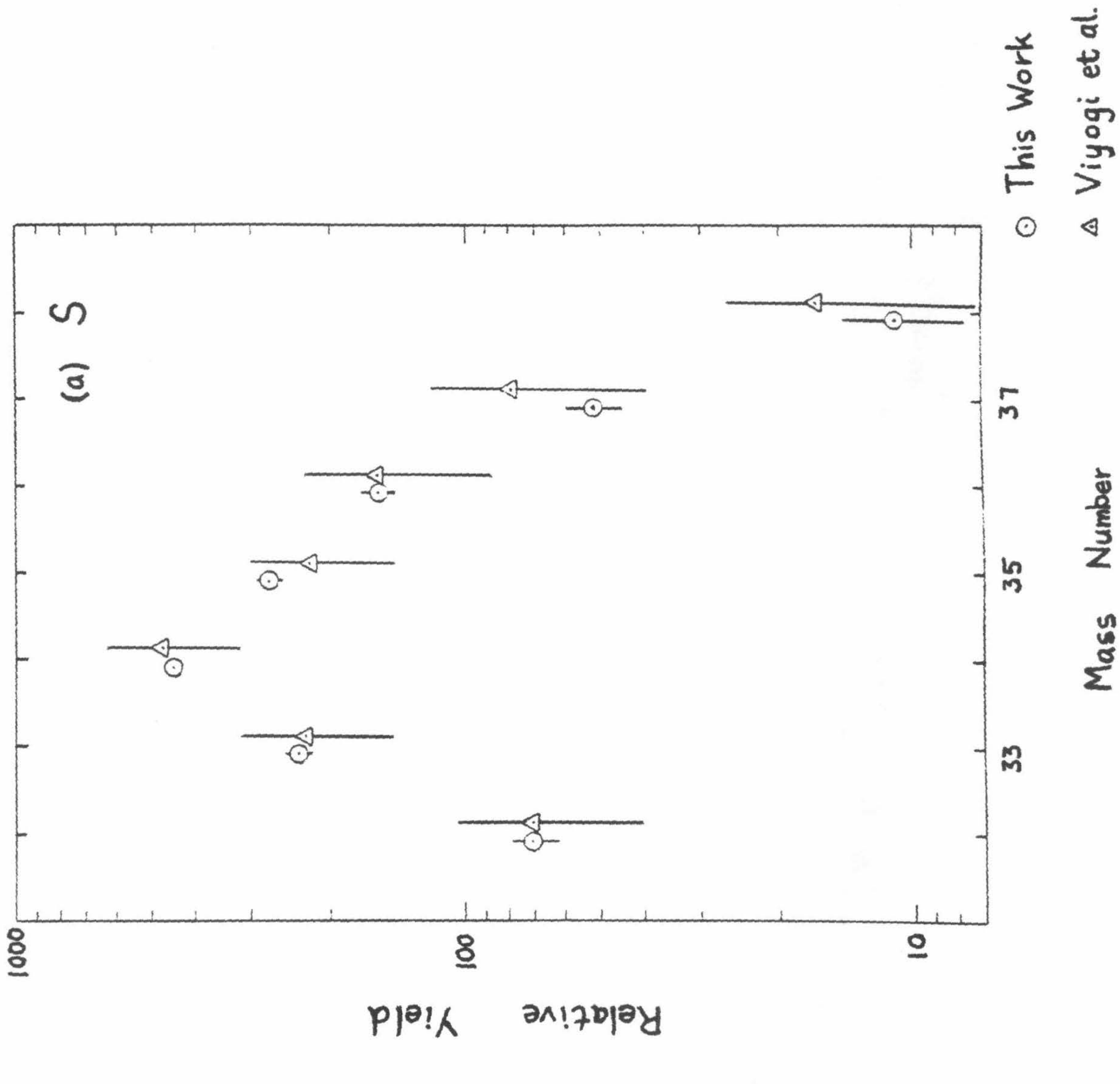
(a) S
Relative Yield
1000
100
10
33
35
37
Mass Number
⊙ This Work
△ Viyogi et al.

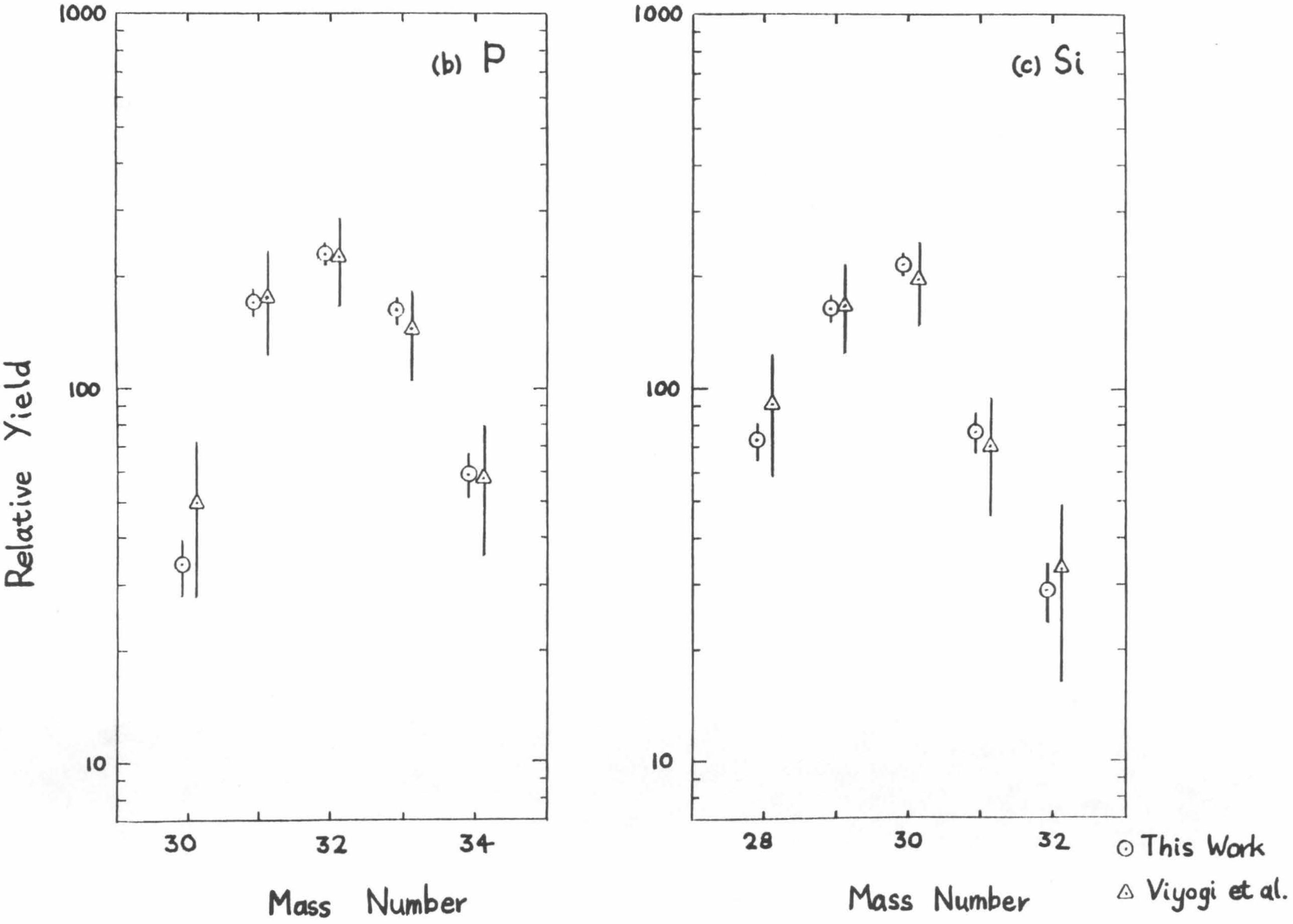
(b) P
(c) Si
Relative Yield
1000
100
10
30
32
34
28
30
32
Mass Number
Mass Number
⊙ This Work
△ Viyogi et al.

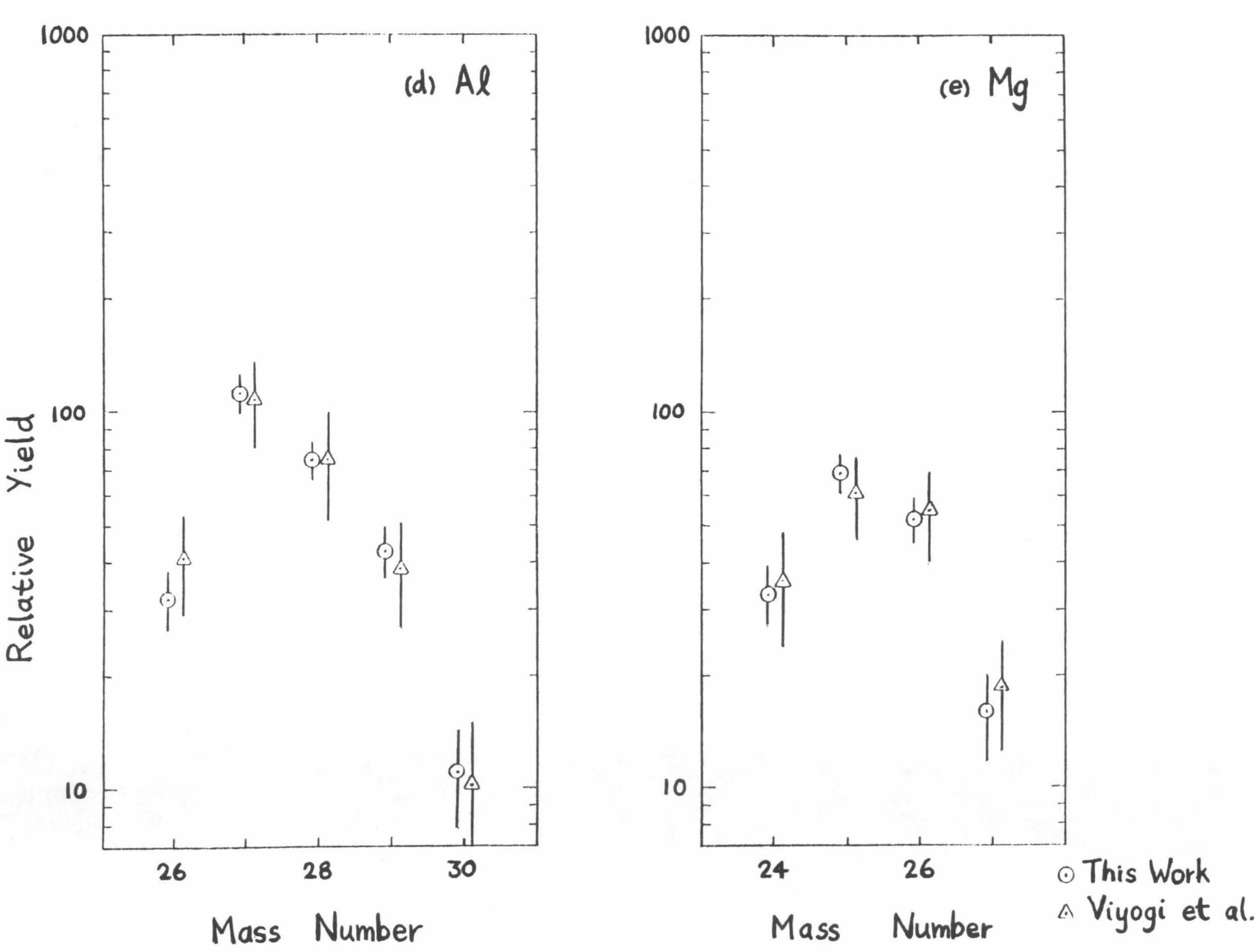
(d) Al
(e) Mg
Relative Yield
1000
100
10
26
28
30
24
26
Mass Number
Mass Number
⊙ This Work
△ Viyogi et al.

3.2.3. Comparison with Calculation

The measured isotope yields presented in Table 3.3 were observed with a thick CH_2 target. The ^{40}Ar beam particles interacted in the target (or even outside the target) at various energies. In addition, the detector geometry is strongly biased against fragments emitted at angles $> 1°$. As a result, we did not have a direct measure of the absolute value of the interaction cross-sections. However, we can still test the semi-empirical cross-sections of Silberberg and Tsao with our observed isotope yields if we model the experimental setup and if we assume that the relative yields are not strongly angular dependent.

The isotope yields expected on the basis of the Silberberg and Tsao semi-empirical formulae were calculated using a Monte Carlo calculation. The Monte Carlo propagation program was developed by Dr. Mark Wiedenbeck at the University of Chicago and modified by us to run on a VAX at the Caltech computing center. Beam particles (^{40}Ar) simulated in the calculation were followed, taking into account ionization energy loss, as they traversed the stack of materials. The experimental setup was modelled and the thickness of the Cu absorber was varied (from 0.16 to 2.20 g/cm^2) in the calculation. Table 3.4 gives a list of the materials modelled in the Monte Carlo simulation. Distances the beam particles traversed before undergoing a nuclear interaction were generated using the total cross-section formula by Hagen (1976). The heaviest fragment nucleus produced in each interaction was assumed to proceed forward with nearly the velocity of the fragmenting nucleus, while all lighter fragments were ignored. The relative probabilities of producing the various possible fragments were calculated from the Silberberg and Tsao cross-section formulae (1973a,b and 1977a,b).

A large number ($> 10^6$) of ^{40}Ar nuclei simulated in this calculation were

Table 3.4

Slab Description	Thickness (g/cm^2)	Material Assumed (and mass fractions)
Variable Absorber	0.00-2.20	Cu (1.000)
Air	0.13	N (.745), O (.229), Ar (.026)
CH_2 Target	1.75-4.10	H (.143), C (.857)
Beam Spreader[a]	0.22-1.08	Al (1.000)
Air	0.32	N (.745), O (.229), Ar (.026)
MWPCs	0.013	H (.013), C (.192), O (.103), Ar (.692)
Telescope Window	0.0034	Al (1.000)
M1-M4	0.107	Si (1.000)
D1	0.733	Si (1.000)
D2	0.728	Si (1.000)
D3	1.123	Si (1.000)
D4	0.727	Si (1.000)
D5	0.728	Si (1.000)

[a] The beam spreader was used so that a monoenergetic beam which goes through it will have a distribution of energy for the exiting particles. It consists of aluminum rods glued on a piece of aluminum plate and the distribution of aluminum thickness is modelled in the Monte Carlo calculation. The beam spreader was not used when data subsets 1 and 2 were taken.

Table 3.4 The list of materials modelled in the Monte Carlo calculation.

followed. The Monte Carlo calculation was done so that the non-interacting ^{40}Ar range distribution resembles the observed one. Since our experiment did not provide absolute measure of the number of ^{40}Ar hitting the target, it is not possible for us to compare the absolute yields. Instead, the calculated yields will be normalized to the observed yields using the total number of fragments of the elements P, S, and Cl. The differences between observed and calculated yields reflect inaccuracies in the Silberberg and Tsao formulae. According to our calculations, most of the observed fragments are produced in a single interaction (the contributions from multiple interactions range from ~5% for Cl to ~25% for Mg), and ~92% of the interactions occur in the CH_2 target. Of the interactions in the CH_2, 46% involve collisions with H nuclei. Furthermore, cross-sections for collisions with C are thought to scale from the cross-sections on H as mentioned in Chapter 1. Thus our comparison of observed and calculated yields should provide a rather direct test of the accuracy of the Silberberg and Tsao cross-sections for predicting relative yields for the inclusive reactions $^{40}\mathrm{Ar} + {}^{1}\mathrm{H} \rightarrow (Z,A) + X$.

Table 3.5 lists the calculated relative yields along with the observed yields. The calculated yields for the three data subsets are listed in columns 3 through 5. These three columns of calculated yields are consolidated into one set of calculated yields. The method used for normalizing the three data subsets is the same as the one used for normalizing the three sets of observed yields. The third set of calculated yields is normalized to the second set using the total number of Cl and S fragments. There are 45997 and 13567 fragments of Cl and S in the second and third sets of calculated yields respectively. Therefore, the results of the third set should be scaled by a factor of 3.390 to normalize them to the second set. Simiarly, the second set of calculated yields is normalized to the first set using the

Table 3.5

Isotope	Observed Yield[a]	Calculated Yields				Norm. Calc. Yield[c]	Observed to Calc. Ratio[d]
		Set 1	Set 2	Set 3	Norm.[b]		
$^{40}\mathrm{K}$	29.4±7	--	--	136	2357	31.4	0.94±.24
$^{39}\mathrm{K}$	41.5±9	--	--	142	2461	32.8	1.27±.30
$^{38}\mathrm{K}$	<1.86	--	--	69	1196	15.9	<0.13
$\mathrm{K}_{\mathrm{total}}$	70.9±12	--	--	347	6014	80.1	0.89±.16
$^{39}\mathrm{Ar}$	883.1±41	--	--	3589	62208	828.4	1.07±.05
$^{38}\mathrm{Ar}$	561.7±33	--	--	2692	46660	621.3	0.90±.06
$^{37}\mathrm{Ar}$	217.8±21	--	--	1075	18633	248.1	0.88±.09
$^{36}\mathrm{Ar}$	72.6±12	--	--	172	2981	39.7	1.83±.33
$\mathrm{Ar}_{\mathrm{total}}$	1735.2±57	--	--	7528	130482	1737.5	1.00±.03
$^{39}\mathrm{Cl}$	318.0±26	--	2929	1004	17402	231.7	1.37±.12
$^{38}\mathrm{Cl}$	273.1±26	--	5943	1681	29137	388.0	0.70±.07
$^{37}\mathrm{Cl}$	556.5±35	--	6876	1925	33366	444.3	1.25±.08
$^{36}\mathrm{Cl}$	475.3±31	--	7454	2119	36729	489.1	0.97±.07
$^{35}\mathrm{Cl}$	216.0±21	--	3067	869	15062	200.6	1.08±.11
$^{34}\mathrm{Cl}$	39.7±9	--	532	152	2635	35.1	1.13±.27
$\mathrm{Cl}_{\mathrm{total}}$	1878.6±62	--	26801	7750	134331	1788.8	1.05±.04
$^{38}\mathrm{S}$	11±3	298	52	18	298	4.0	2.75±.77
$^{37}\mathrm{S}$	52±7	2615	434	118	2615	34.8	1.49±.20
$^{36}\mathrm{S}$	157±13	14739	2896	854	14739	196.3	0.80±.07
$^{35}\mathrm{S}$	273±18	26942	5317	1561	26942	358.8	0.76±.05
$^{34}\mathrm{S}$	449±22	37049	7228	2308	37049	493.3	0.91±.04
$^{33}\mathrm{S}$	236±16	12835	2516	724	12835	170.9	1.38±.09
$^{32}\mathrm{S}$	71±8	3825	753	234	3825	50.9	1.39±.16
$\mathrm{S}_{\mathrm{total}}$	1249±37	98303	19196	5817	98303	1309.0	0.95±.03

[a] The observed yields of the elements Mg through S are from data subset 1. The observed yields of the elements Cl through K are from data subset 3 and are normalized to data subset 1 as explained in the text. The normalization factor is 1.728.

[b] The three sets of calculated yields are normalized with respect to each other in the same way the three sets of observed yields are normalized. The yields of the elements Mg through S are from set 1. The yields of the elements Cl through K are from set 3 and are normalized to set 1. The yields of set 3 are first normalized to set 2 using the total number of Cl and S fragments (a normalization factor of 3.390) and then from set 2 to set 1 using the total number of S and P fragments (a normalization factor of 5.112). The overall normalization factor is 17.333.

c,d see next page

Table 3.5 The calculated isotope yields as predicted by the Monte Carlo simulations.

Table 3.5 (continued)

Isotope	Observed Yield[a]	Calculated Yields				Norm. Calc. Yield[c]	Observed to Calc. Ratio[d]
		Set 1	Set 2	Set 3	Norm.[b]		
$^{35}\mathrm{P}$	18±4	999	198	--	999	13.3	1.35±.30
$^{34}\mathrm{P}$	59±8	4617	904	--	4617	61.5	0.96±.13
$^{33}\mathrm{P}$	162±13	15825	3106	--	15825	210.7	0.77±.06
$^{32}\mathrm{P}$	229±16	17316	3399	--	17316	230.6	0.99±.07
$^{31}\mathrm{P}$	170±13	11099	2168	--	11099	147.8	1.15±.09
$^{30}\mathrm{P}$	34±6	2852	567	--	2852	38.0	0.89±.16
P_{total}	672±27	52708	10342	--	52708	701.9	0.96±.04
$^{32}\mathrm{Si}$	29±6	3628	--	--	3628	48.3	0.60±.12
$^{31}\mathrm{Si}$	77±9	8346	--	--	8346	111.1	0.69±.08
$^{30}\mathrm{Si}$	217±15	16745	--	--	16745	223.0	0.97±.07
$^{29}\mathrm{Si}$	165±13	8456	--	--	8456	112.6	1.47±.12
$^{28}\mathrm{Si}$	73±9	3916	--	--	3916	52.1	1.40±.17
Si_{total}	561±25	41091	--	--	41091	547.1	1.03±.05
$^{30}\mathrm{Al}$	11±4	1351	--	--	1351	18.0	0.61±.22
$^{29}\mathrm{Al}$	43±7	5875	--	--	5875	78.2	0.55±.09
$^{28}\mathrm{Al}$	75±9	8147	--	--	8147	108.5	0.69±.08
$^{27}\mathrm{Al}$	112±11	7884	--	--	7884	105.0	1.07±.11
$^{26}\mathrm{Al}$	32±6	2801	--	--	2801	37.3	0.86±.16
Al_{total}	273±18	26058	--	--	26058	347.0	0.79±.05
$^{27}\mathrm{Mg}$	16±5	3333	--	--	3333	44.4	0.36±.11
$^{26}\mathrm{Mg}$	52±8	8889	--	--	8889	118.4	0.44±.07
$^{25}\mathrm{Mg}$	69±9	6545	--	--	6545	87.2	0.79±.10
$^{24}\mathrm{Mg}$	33±6	4174	--	--	4174	55.6	0.59±.11
Mg_{total}	170±14	22941	--	--	22941	305.6	0.56±.05

a,b see previous page

c The calculated yields (column 6) are normalized to the observed yields (column 2) using the total number of P, S, and Cl fragments.

d The ratio of the observed yield (column 2) to the normalized calculated yield (column 7) for each of the isotopes.

Table 3.5 (continued) The calculated isotope yields as predicted by the Monte Carlo simulations.

total number of S and P fragments. There are 151011 and 29538 fragments of Cl and S in the first and second sets of calculated yields respectively. Therefore, the results of the second set should be scaled by a factor of 5.112 to normalize them to the first set. In other words, the results of the third set can be normalized to the first set by scaling them with a factor of 17.33 Column 6 of Table 3.5 lists the consolidated set of calculated yields. The yields of the elements Mg through S are from data set 1; whereas the yields of the elements Cl through K are from data set 3 and are normalized to data set 1. The calculated yields of column 6 are then normalized to the observed yields using the total number of P, S, and Cl fragments. Finally, the last column of Table 3.5 gives the ratios of the observed yields (column 2) to the calculated yields (column 7).

Figure 3.8 shows the observed isotope yields (column 2 of Table 3.5) along with the calculated isotope yields (column 7). Notice that the observed yield of ^{39}Cl is higher than that of ^{38}Cl by more than 15%. On the other hand, the calculated yield of ^{39}Cl is lower than that of ^{38}Cl by more than 40%. This suggests that the semi-empirical formulae underestimates the effects of the peripheral reaction for the production of ^{39}Cl.

The observed yields of ^{40}K and ^{39}K are consistent with those expected from the Monte Carlo calculation. However, we observed no ^{38}K at all whereas the Monte Carlo calculation predicted about 16. The 84% upper limit for observing no event is only 1.86 and thus the observation is a statistically significant one. Note that ^{38}K has 19 neutrons, one less than the magic number 20; this implies that the production of ^{38}K involves the removal of a neutron from a complete nuclear shell. The Silberberg and Tsao formulae do not take into account nuclear shell structure. This might be the explanation for the discrepancy between the observed and calculated yields

Figure 3.8

A comparison of measured and calculated fragmentation yields, normalized to the same total yield of $15 \leq Z \leq 17$ fragments. The experimental uncertainties are statistical only.

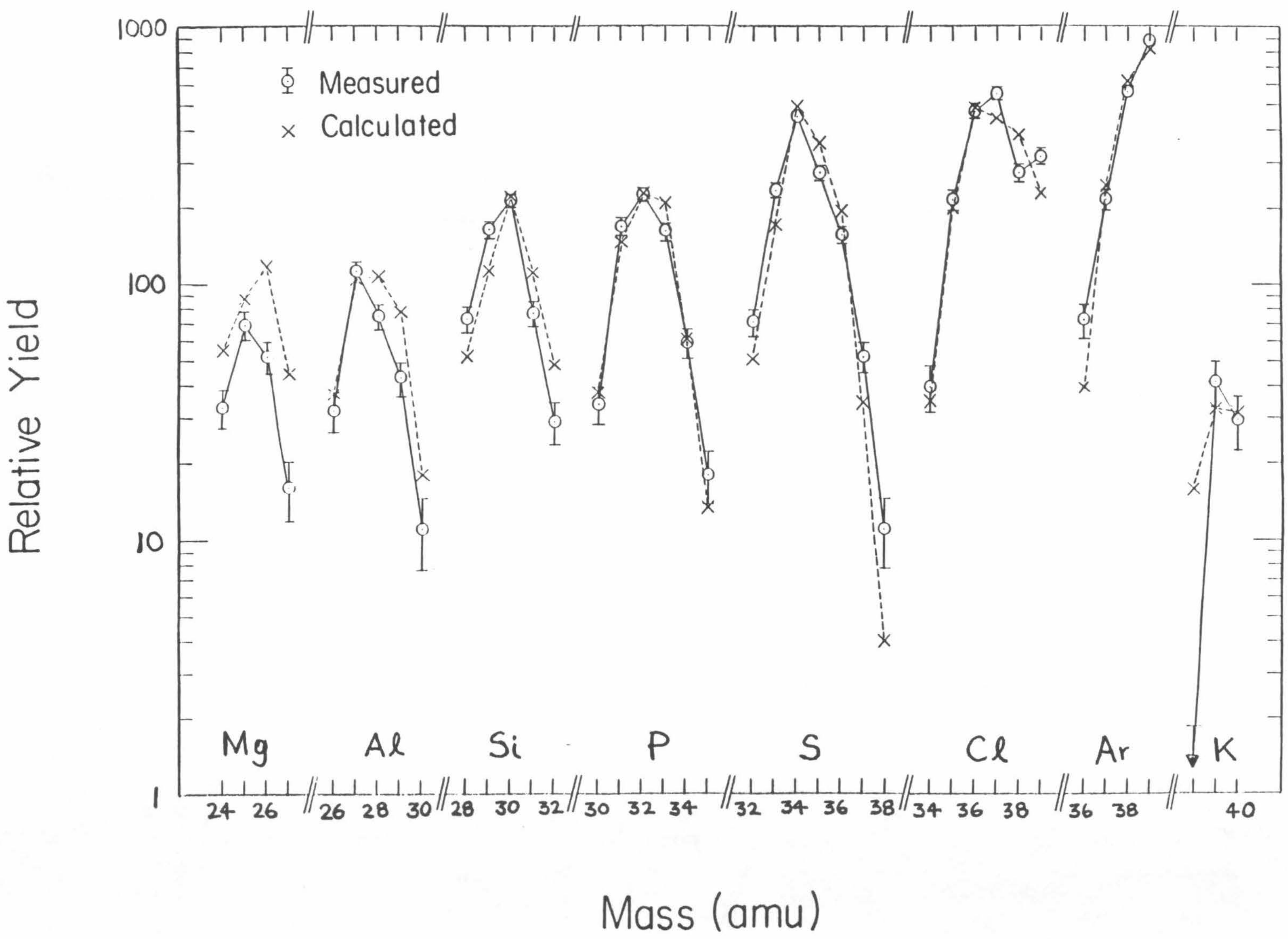
Measured
Calculated
Relative Yield
1000
100
10
1
Mg
Al
Si
P
S
Cl
Ar
K
24 26
26 28 30
28 30 32
30 32 34
32 34 36 38
34 36 38
36 38
40
Mass (amu)

of ^{38}K.

Another noticeable difference between the observed and calculated yields is that of the element yields of Al and Mg. With our normalization between the calculated and observed yields, the observed element yields of Al and Mg are significantly lower than the calculated ones; whereas the observed yields are consistent with the calculated ones for the other elements. This could be due to some of the limitations of our experimental setup. Our analysis only includes events within the central 20 cm^2 of the detector stack. As a result, fragments emitted at large angles (> 1°) were not analyzed by the solid state detector stack. We have studied the angle distributions of the fragments using the MWPC (shown in figure 3.1) which extends (in angle) beyond the detector stack. Comparison of angle distributions of two data subsets, one subset contains mostly Cl, S and some P fragments and the other contains mostly Al, Mg and some lower charge fragments, shows that the fraction of events accepted by our analysis is reduced by ~50% for the lower charge group compared to the higher charge group (note that this ~50% reduction is averaged over the fragments of Al, Mg and some other lower charge elements, which means that this reduction is probably not as great for Al). However, the MWPC does not have good enough charge resolution to give us angle distributions of the individual elements; and it is also difficult to estimate, to good accuracy, the number of fragments not detected by the stack of solid state detectors. Due to these reasons, we cannot make quantitative corrections to our observed yields of Al and Mg, and compare the isotope yields individually.

If the fraction of yields observed for Na, Mg, and Al is indeed ~50% lower than that for P, S, and Cl, this might result from a Z-dependent effect which did not affect the yield of isotopes in an element. However, another possibility is that there is a smooth mass dependent bias of ~5% per amu in our data sample. This would affect the yield of isotopes within an element such that the yield of the heaviest isotope of an element might be overestimated by ~10%, while that of the lightest isotope is underestimated by ~10%. In most cases, the magnitude of this possible effect is smaller than the statistical uncertainties of the measurement, but it does represent a possible systematic error in our data sample that should be kept in mind. The magnitude of this possible mass dependent effect can also be estimated by studying the observed to calculated element ratios in Table 3.5. We have fitted the observed to calculated ratios (R) in Table 3.5 as a linear function of the element mean mass (m_m) and found that $R = 0.127 + 0.024 \cdot m_m$. This implies a 2.4% per amu effect.

The isotope yields in Table 3.5 are presented in Table 3.6 as fractional yield of the individual element. The isotope fractions for the isotopes of Mg through Cl are plotted (in Gaussian probability scale) in figure 3.9. For the elements Mg through P, both the observed and calculated yields fit very well to straight lines; in other words, the mass distributions are Gaussian -- in agreement with the semi-empirical model (see Chapter 1). For the element S, the calculated mass distribution fits very well to a Gaussian distribution whereas the observed mass distribution seems to deviate from a Gaussian distribution. For the element Cl, both the observed and calculated mass distributions seem to deviate from Gaussian distributions. The deviations of the higher mass isotopes from the Gaussian distributions of the lower mass isotopes are the result of increases in cross-sections due to peripheral reactions (as discussed in Chapter 1). In both the cases of S and Cl, the semi-empirical formulae seem to underestimate the yield from peripheral reactions. If we ignore the isotopes affected by peripheral reactions, the slopes

Table 3.6

Isotope	Fraction of Element	
	Observed	Calculated
^{40}K	0.415±.080	0.392±.026
^{39}K	0.585±.080	0.409±.026
^{38}K	--	0.199±.021
^{39}Ar	0.509±.017	0.477±.006
^{38}Ar	0.324±.016	0.357±.006
^{37}Ar	0.125±.011	0.143±.004
^{36}Ar	0.042±.007	0.023±.002
^{39}Cl	0.169±.013	0.130±.004
^{38}Cl	0.146±.012	0.217±.005
^{37}Cl	0.296±.015	0.248±.005
^{36}Cl	0.253±.015	0.273±.005
^{35}Cl	0.115±.011	0.112±.004
^{34}Cl	0.021±.005	0.020±.002
^{38}S	0.009±.003	0.003±.000
^{37}S	0.042±.006	0.027±.001
^{36}S	0.126±.010	0.150±.001
^{35}S	0.218±.012	0.274±.001
^{34}S	0.359±.014	0.377±.002
^{33}S	0.189±.012	0.130±.001
^{32}S	0.057±.007	0.039±.001

Table 3.6 Observed and calculated isotope fractions.

Table 3.6 (continued)

Isotope	Fraction of Element	
	Observed	Calculated
^{35}P	0.027±.006	0.019±.001
^{34}P	0.088±.011	0.088±.001
^{33}P	0.241±.017	0.300±.002
^{32}P	0.341±.019	0.328±.002
^{31}P	0.253±.017	0.211±.002
^{30}P	0.050±.009	0.054±.001
^{32}Si	0.052±.010	0.088±.001
^{31}Si	0.137±.015	0.203±.002
^{30}Si	0.387±.022	0.408±.002
^{29}Si	0.294±.020	0.206±.002
^{28}Si	0.130±.015	0.095±.001
^{30}Al	0.040±.013	0.052±.001
^{29}Al	0.158±.024	0.225±.003
^{28}Al	0.275±.029	0.313±.003
^{27}Al	0.410±.032	0.303±.003
^{26}Al	0.117±.021	0.107±.002
^{27}Mg	0.094±.024	0.145±.002
^{26}Mg	0.306±.038	0.388±.003
^{25}Mg	0.406±.041	0.285±.003
^{24}Mg	0.194±.033	0.182±.003

Table 3.6 (continued) Observed and calculated isotope fractions.

Figure 3.9

Observed and calculated mass distributions for the elements Mg through Cl. The mass distributions are shown in Gaussian probability scale for the fraction of isotopes within an element with mass greater than that indicated by the horizontal axis. For example, for the observed Mg distribution, the fraction shown at 24 amu is the fraction of observed Mg isotopes which have mass greater than 24 amu.

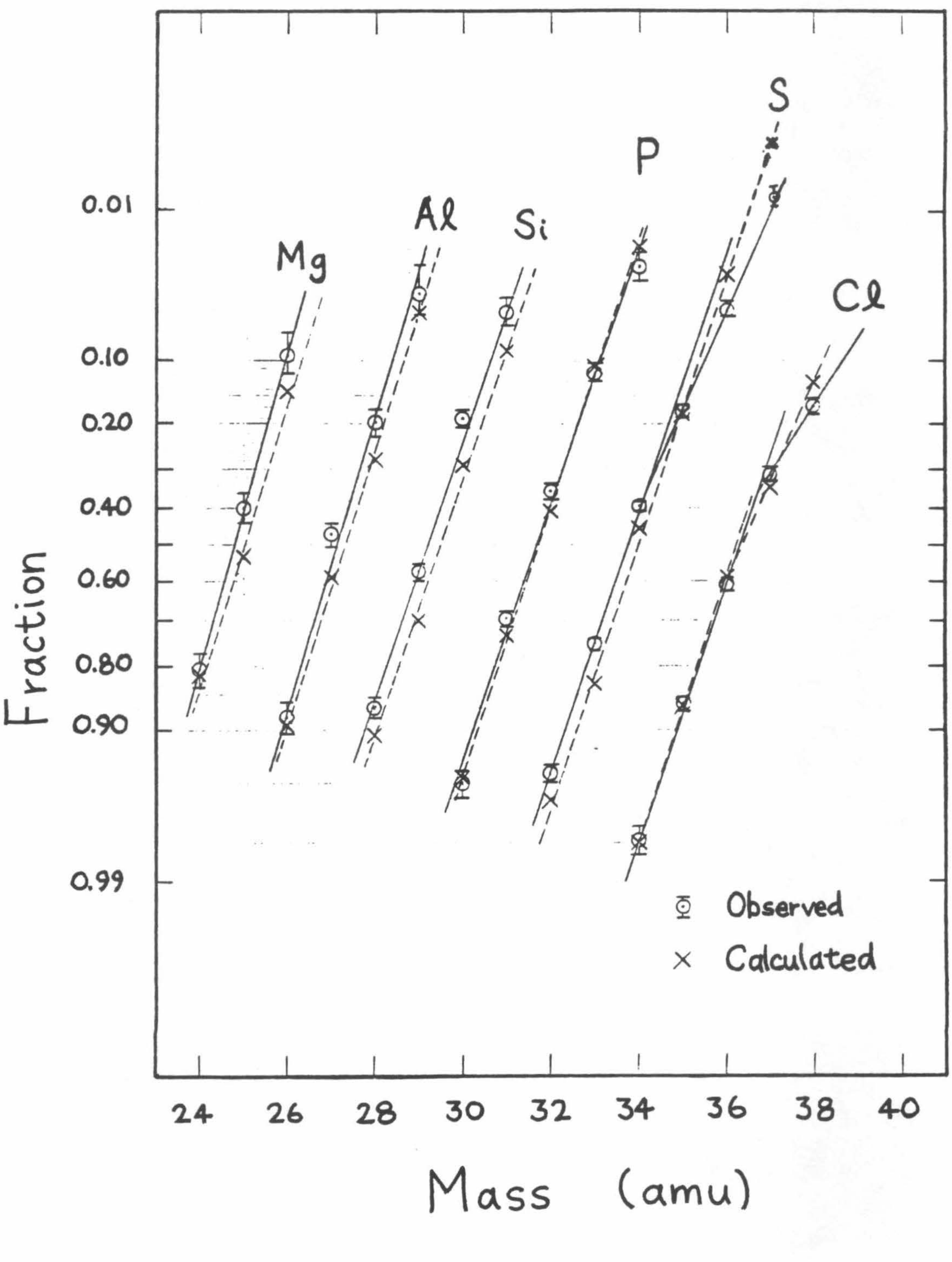
Fraction
0.01
0.10
0.20
0.40
0.60
0.80
0.90
0.99
Mg
Al
Si
P
S
Cl
Observed
Calculated
24
26
28
30
32
34
36
38
40
Mass (amu)

of the fitted lines suggest that the width (standard deviation) of the observed mass distribution is narrower than the calculated for Mg and gradually becomes wider than the calculated for Cl as the charge of the element increases. The medians of the observed distributions are lower than those of the calculated ones by 0.2 amu to 0.3 amu for the elements Mg, Al, Si, and S (however, note that the median of S is influenced by the high mass tail). Note that this effect is in the opposite direction to that expected if there were indeed a mass dependent systematic effect in our efficiency for detecting light fragments.

We have also studied the ratio between the observed and calculated isotope fractions of individual nuclides with $12 \leq Z \leq 18$ for which at least 40 events were collected in the experiment. Figure 3.10 shows the distribution of this ratio for 26 nuclides. The distribution has an rms spread of 25%. Notice that this rms spread is comparable to the claimed accuracy of the Silberberg and Tsao formulae. However, one should also note that the Silberberg and Tsao claimed accuracy is for absolute cross-sections and our comparison is done with isotope fractions.

We summarize the findings on the ^{40}Ar fragmentation study as follows. We have compared our measured isotope yields of the elements Mg through S with those measured by Viyogi et al. and found that the two sets of measurements are consistent with each other. This suggests that the relative isotope yields within an element do not depend strongly on the material of the target. We have compared the observed and calculated yields for the elements Si through K. We found the observed relative elemental yields consistent with the calculation although perhaps some of this agreement is fortuitous, since the observed yields of Mg and Al are significantly lower than expected. The observed relative isotope fractions agree with the calculated

Figure 3.10

Distribution of the ratio of calculated to measured isotope fractions for isotopes of Mg through Ar. This distribution only includes isotopes which have at least 40 events collected in the experiment.

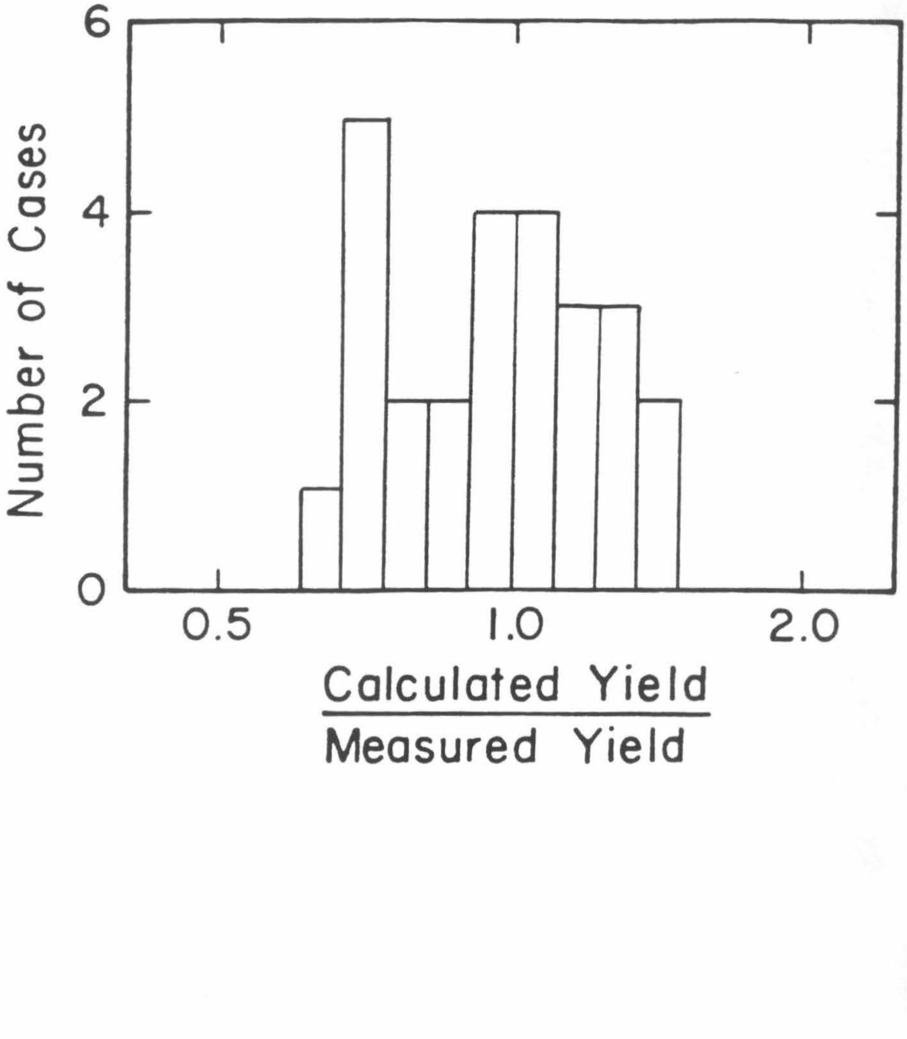
6
4
2
0
Number of Cases
0.5
1.0
2.0
Calculated Yield
Measured Yield

ones with a mean accuracy of 25%. Noticeable differences were observed for the cases of ^{39}Cl and ^{38}K. For the elements Mg and Al, the observed yields are significantly lower than the calculated ones. This is likely the result of some of the limitations of our experimental setup. Comparisons of the observed and calculated mass-yield distributions show that, for the elements Mg, Al, Si, and S, the medians of the observed mass-yield distributions are lower than expected from the calculation. In addition, the observed mass distributions of S and Cl show a greater yield from peripheral reactions than expected from the calculation. Although the widths of the observed distributions are consistent with the calculation, a systematic trend can be seen.

3.3. Fragmentation of ^{56}Fe

Fragmentation cross-sections of ^{56}Fe are important for cosmic ray studies because ^{56}Fe is the most abundant isotope with $Z > 14$. We have analyzed a set of data obtained during a calibration in which ^{56}Fe was fragmented in a CH_2 target. Observed isotope yields are compared with those expected on the basis of the Monte Carlo calculations. In this section, we report the findings of the comparison between observed and calculated yields. In the next section, we will compare the findings of this study with the findings of the ^{40}Ar fragmentation study.

3.3.1. Experimental Setup

This set of data was obtained at the Lawrence Berkeley Laboratory Bevalac accelerator in April, 1978 during the pre-flight calibration of the Heavy Isotope Spectrometer Telescope (HIST). HIST was carried into space on ISEE-3 in August of 1978 and provided high-resolution measurements of both solar energetic particles and galactic cosmic rays. A beam of 583 MeV/amu ^{56}Fe was used during the calibration. The experimental setup was very similar to the one shown in figure 3.1. The HIST detector stack was in the position of the solid state detector stack shown in figure 3.1. Figure 3.11 shows a schematic diagram of the HIST detector stack. It consists of eleven silicon solid-state particle detectors arranged to form a particle telescope. Table 3.7 is a list of the detectors that comprise HIST. Detectors M1 through D3 are silicon surface-barrier solid-state detectors. Detectors D4 through D9 are Li-drifted detectors with a central detection area and an annular guard ring (shaded in figure 3.11), which is used as an active anticoincidence shield. The nominal detection areas for the detectors are 470 mm^2 for M1 and M2, 580 mm^2 for D1, 830 mm^2 for D2 and D3, and 910 mm^2 for detectors D4 through D9. A description of HIST can be found in Althouse

Figure 3.11

Schematic diagram (to scale) of the Heavy Isotope Spectrometer Telescope (HIST). The shaded areas of detectors D4 to D9 are annular guard rings used as an active anti-coincidence shield.

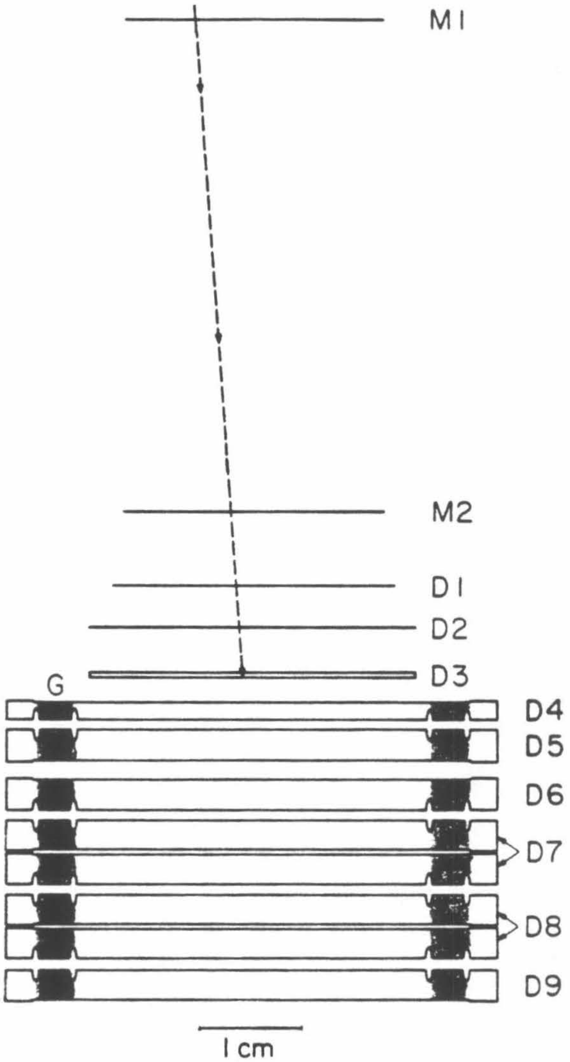
M1
M2
D1
D2
D3
G
D4
D5
D6
D7
D8
D9
1 cm

Table 3.7

Detector	Detector Type	Nominal Thickness (μm of Si)	Dead Layer (μm of Si)
M1	sb-Mdet[a]	50	--
M2	sb-Mdet	50	--
D1	sb[b]	90	--
D2	sb	150	--
D3	sb	500	--
D4	Li-D[c]	1700	45
D5	Li-D	3000	56
D6	Li-D	3000	57
D7a	Li-D	3000	65
D7b	Li-D	3000	75
D8a	Li-D	3000	55
D8b	Li-D	3000	64
D9	Li-D	3000	66

[a] surface-barrier detector--"matrix detector"

[b] surface-barrier detector

[c] Lithium-drifted detector

Table 3.7 Detector type, thickness, and dead layer thickness of HIST detectors.

et al. (1978). M1 and M2 are position-sensitive matrix detectors which allow the determination of particle trajectories. Two multiwire proportional counters were also employed in this experimental setup. However, they were not used in the analysis because trajectory measurements were already provided by M1 and M2. A 583 MeV/amu ^{56}Fe beam exited the Bevalac vacuum and impinged on a 2.25 inch (5.26 g/ cm^2) thick CH_2 target. As in the case of the ^{40}Ar fragmentation run, a variable thickness Cu absorber was utilized to "tune" the energy of the beam and most of the interactions which occurred in the Cu were not analyzed by the detectors.

Since the experimental setup was similar to the one described in section 3.3.1, the limitations discussed in that section are also applicable here. Nevertheless, with the good mass resolution, this data provides measurement of the *relative* fragmentation yields.

3.3.2. Analysis and Results

The outputs of detectors D3 to D8 were used to determine the mass of fragments stopping in D5 through D8. The mass determination algorithm has been described by Spalding 1983. The technique is similar to the one used in the ^{40}Ar analysis (i.e., the ΔE-E′ technique). Instead of using the power law approximation for the range-energy relationship, the proton range table of Janni (1966) was used in the computation with A/Z^2 scaling. With Spalding's algorithm, we have two equations and three unknowns (Z, M, and E), as in the Ar fragmentation analysis. In this case, however, we solve for the mass M, instead of the effective charge (Z′), described by equation (3.5). In the calculation, an integer charge Z was assumed and only events with calculated masses near those of stable isotopes were considered as solutions. Events with calculated masses which are not near any stable isotope were considered as isotopes of other charges. Throughout the entire operating range of HIST, unique solutions for mass and charge are always possible.

In our analysis, two masses were calculated for each event. In general, for a particle stopping in detector N, the first mass, mass1, was calculated using detector (N-1) as the ΔE detector and detector N as the E' detector. The second mass, mass2, was calculated using detector (N-2) as the ΔE detector, and detector N and detector (N-1) combined as the E' detector.

3.3.2.1. Corrections to Calculated Mass

As pointed out by Spalding, in order to calculate the mass using the ΔE-E' technique, the range energy relation must be known to sufficient accuracy. Unfortunately, published tables of the range energy relations are insufficiently accurate for our purposes and have systematic errors of the order of a few percent. As a result, the calculated mass has typical errors of the order of 5 amu for Fe events. Thus a correction scheme was developed by Spalding to correct each calculated mass, separately. This is the correction scheme we adopted in our mass calculations and we will describe it here.

In each range the preliminary calculated mass was plotted vs. E1, the energy in the stopping detector. Figure 3.12 shows an example of this type of plot, for mass1 of iron in Range 7 (i.e., iron particles stopping in D7). The approximate form of mass1 vs. E1 for the principle isotope of an element was then fitted by hand to the plot by a series of line segments. This approximate form of the preliminary calculated mass, g(E1), was then used to correct the calculated mass of each particle with the equation

$$M(\text{corrected}) = M(\text{preliminary}) \cdot \frac{M_o}{g(E1)} \qquad (3.12)$$

where M_o is the mass in amu of the principal isotope. A separate g(E1) was

Figure 3.12

A scatter plot of mass1 vs. E1, the energy in the stopping detector, for iron particles stopping in D7. The calculated mass, mass1, was computed using D6 as the ΔE detector and D7 as the E′ detector. The approximate form of mass1 vs. E1 for the principle isotope (^{56}Fe) was then fitted by hand by a series of line segments. This approximate form of the preliminary calculated mass, g(E1), was then used to correct the calculated mass of each particle with equation (3.12).

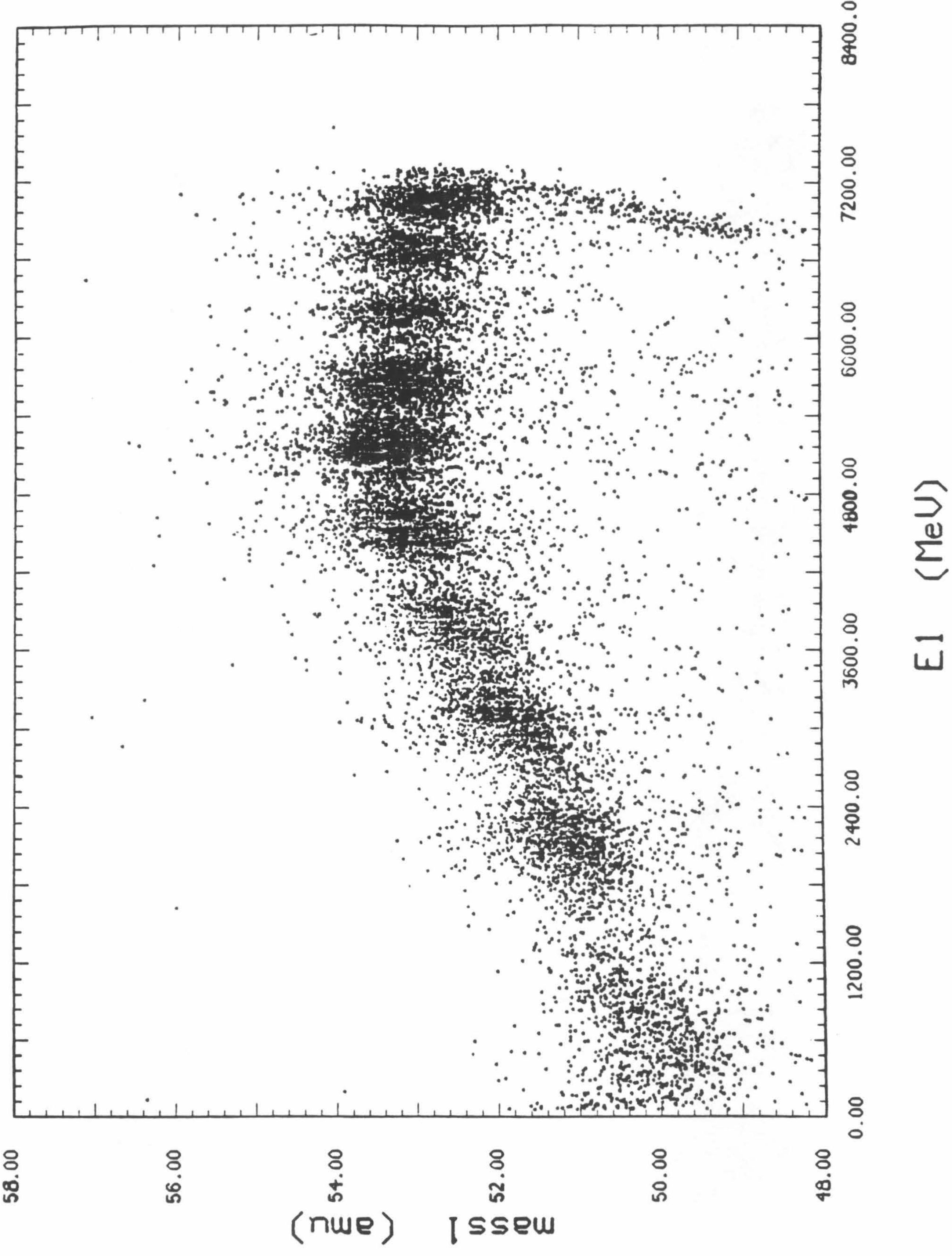
mass1 (amu)
58.00
56.00
54.00
52.00
50.00
48.00
E1 (MeV)
0.00
1200.00
2400.00
3600.00
4800.00
6000.00
7200.00
8400.00

used for each of the calculated masses (mass1 and mass2) of each of the elements we analyzed. This same correction factor was then assumed to apply to all isotopes of that element.

With the correction described by equation (3.12), we have achieved mass resolutions of 0.44 amu and 0.34 amu for mass1 and mass2 respectively for iron events in Range 7. With these two independent mass measurements, we expected to achieve a combined mass resolution of 0.27 amu for the weighted sum of the two masses. However, when the weighted sum was calculated, it only gave a mass resolution of 0.32 amu. It was discovered that the calculated masses depended on the distance of the particle from the center of the detector. Figure 3.13 shows such a dependence for mass1 in Range 7. This is believed to be the result of deficiencies in the detector thickness maps that were used to "correct" the detector's nominal thicknesses in calculating the mass of each event. The thickness maps were obtained by mapping the energy loss profile of 1.9 GeV/nucleon Ar passing through a stack of several detectors. There were more delta-rays generated by these high energy Ar than by the lower energy particles in this analysis. These delta-rays also had higher energy and longer range. For edge events (i.e., far from the center), about half of the delta-rays made in the immediate upstream material were not detected. As a result, the deduced detector thickness would be smaller as compared to the center events where nearly all the delta-rays made in upstream matter were detected. When these thickness maps were used in the mass calculation, the calculated mass would be higher for events near the edge than for events near the center of the detectors. This problem was resolved by applying correction functions to the calculated masses similar to the ones described in the previous paragraph; however, the correction this time was a function of the distance from

Figure 3.13

A scatter plot of mass1 vs. the distance of the particle from the center of the detector.

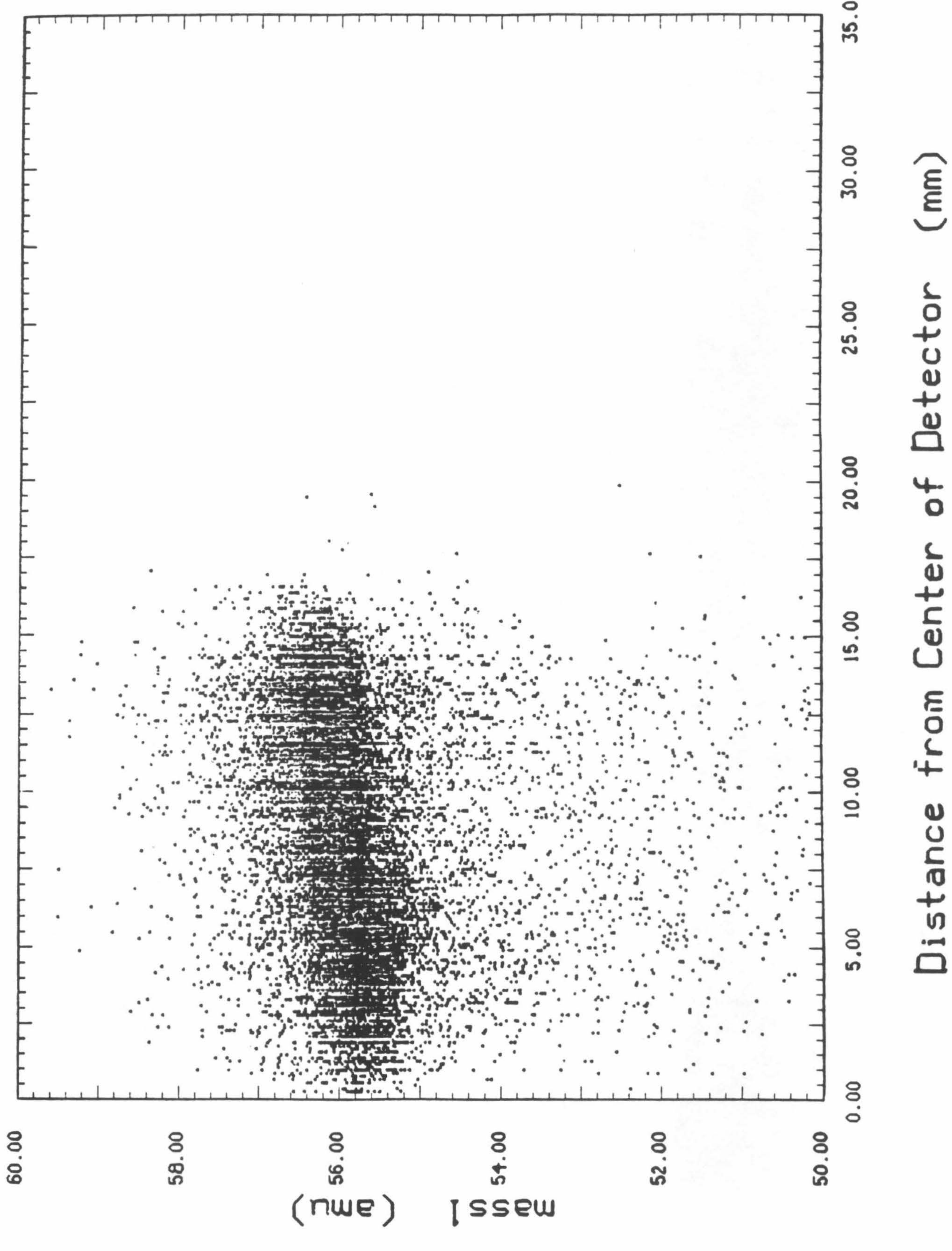
mass1 (amu)
60.00
58.00
56.00
54.00
52.00
50.00
Distance from Center of Detector (mm)
0.00
5.00
10.00
15.00
20.00
25.00
30.00
35.00

the center of the detector, instead of the energy E1. The same corrections were applied to all events. After these corrections were applied, the mass resolutions for Range 7 were improved to 0.36 amu and 0.34 amu for mass1 and mass2 respectively (the radial correction was small for mass2 and did not improve the mass resolution significantly). Figure 3.14 shows the mass distribution of the weighted sum of the two calculated masses, mass1 and mass2, for iron particles stopping in D7. A mass resolution slightly greater than 0.25 amu was achieved which was consistent with the value expected based on the 0.36 amu and 0.34 amu mass resolutions for mass1 and mass2.

Using the weighted sum of the two calculated masses, with the above corrections applied, we have achieved mass resolution of 0.21, 0.25, 0.23, and 0.34 amu for iron particles stopping in D8, D7, D6, and D5 respectively.

3.3.2.2. Background and "Foldback" Events Rejections

To reject background events, we required consistency between the two calculated masses. For each of the ranges (from 5 through 8), we plotted the distribution of the ratio of the two calculated masses for each of the elements. For Mn events stopped in D7, the mass ratio distribution has a standard deviation of about 0.012, which translates into 0.6 amu. Based on the 0.36 amu and 0.34 amu mass resolutions for mass1 and mass2, one would expect the standard deviation for this ratio distribution to be about 0.010. The degradation of the standard deviation is due to contribution from the tails of the ratio distribution. The events in the tails of the ratio distribution are mostly events which interacted in D5 or D6. The standard deviations are 0.010, 0.012, 0.010, and 0.017, for the ratio distribution of events stopping in D8, D7, D6, and D5 respectively. Events with calculated mass ratios more than 3 standard deviations away from the mean of the mass ratio distribution were rejected in our analysis. Less than 4% of the

Figure 3.14

Mass distribution of the weighted sum of mass1 and mass2 for iron particles stopping in D7. A mass resolution slightly greater than 0.25 amu was achieved which was very close to the value expected (slightly less than 0.25 amu) based on the 0.36 amu and 0.34 amu mass resolutions for mass1 and mass2.

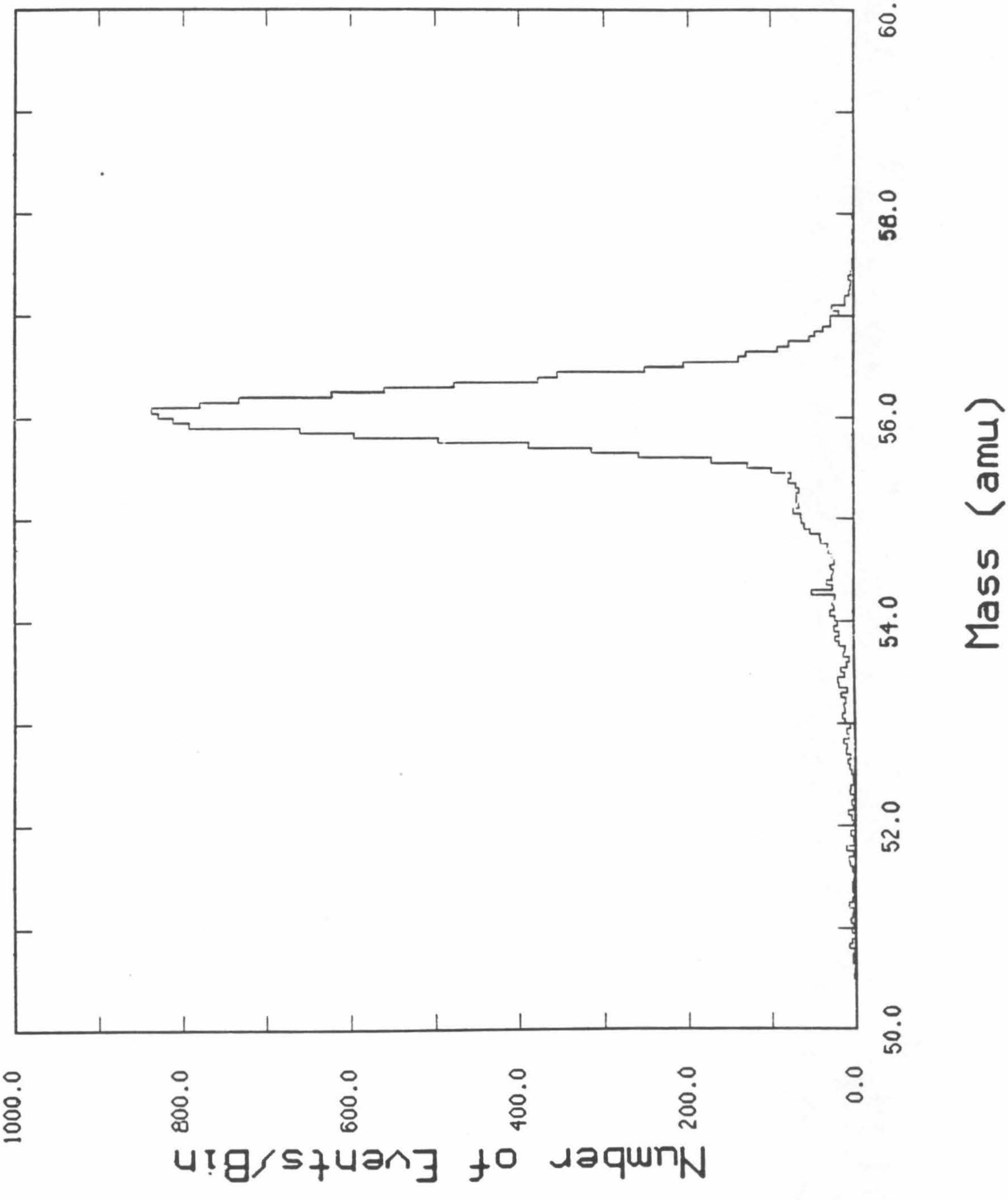
Number of Events/Bin
1000.0
800.0
600.0
400.0
200.0
0.0
50.0
52.0
54.0
56.0
58.0
60.0
Mass (amu)

events were rejected by this consistency test.

The range (in μm of Si) of each of the particles was also calculated so that we could eliminate the "foldback" events, as discussed in the ^{40}Ar fragmentation study (section 3.2.2.1). The range of a particle was defined as the distance from the top of detector D3 to where the particle stopped in the detector stack and was measured in units of μm of Si. Figure 3.15 shows a plot of the calculated mass vs. the calculated range for iron particles stopping in detector D6. "Foldback" events can be observed and the "foldback" in this case extends back for ~300μm. This means that in order to eliminate the "foldback" events, we must also throw away the good events which stopped in the last 300μm of the active layer of the detector. Nevertheless, this is better than accepting events with incorrect calculated masses.

One can also notice in figure 3.15 that the mass resolution is slightly degraded for events which stopped near the top of D6. In general, events stopped near the top of the E′ detector have slightly worse mass resolution as compared to events which stopped further in the E′ detector. As a result, events which stopped in the first 100 μm of the E′ detector are not included in our analysis.

Table 3.8 gives the analyzable range of our analysis. Events which stopped outside of the analyzable range were not included in our analysis. There were 100μm (between D5 and D6), 500μm (between D6 and D7), and 800μm (between D7 and D8) of range not analyzed between detectors. The number of particles which stopped in each of these non-analyzed ranges was estimated using measurements made in 500μm segments of detectors before and after the non-analyzed range. This estimate of missing particles was done for each of the isotopes.

Figure 3.15

A scatter plot of the calculated mass vs. calculated range for iron particles stopping in detector D6. The range of a particle was defined as the distance from the top of detector D3 to where the particle stopped in the detector stack and was measured in microns of Si. "Foldback" events can be observed and the "foldback" extends back ~300 micron. The tracks at the bottom portion of the plot are Mn events, in this case analyzed with an assumed Z of 26.

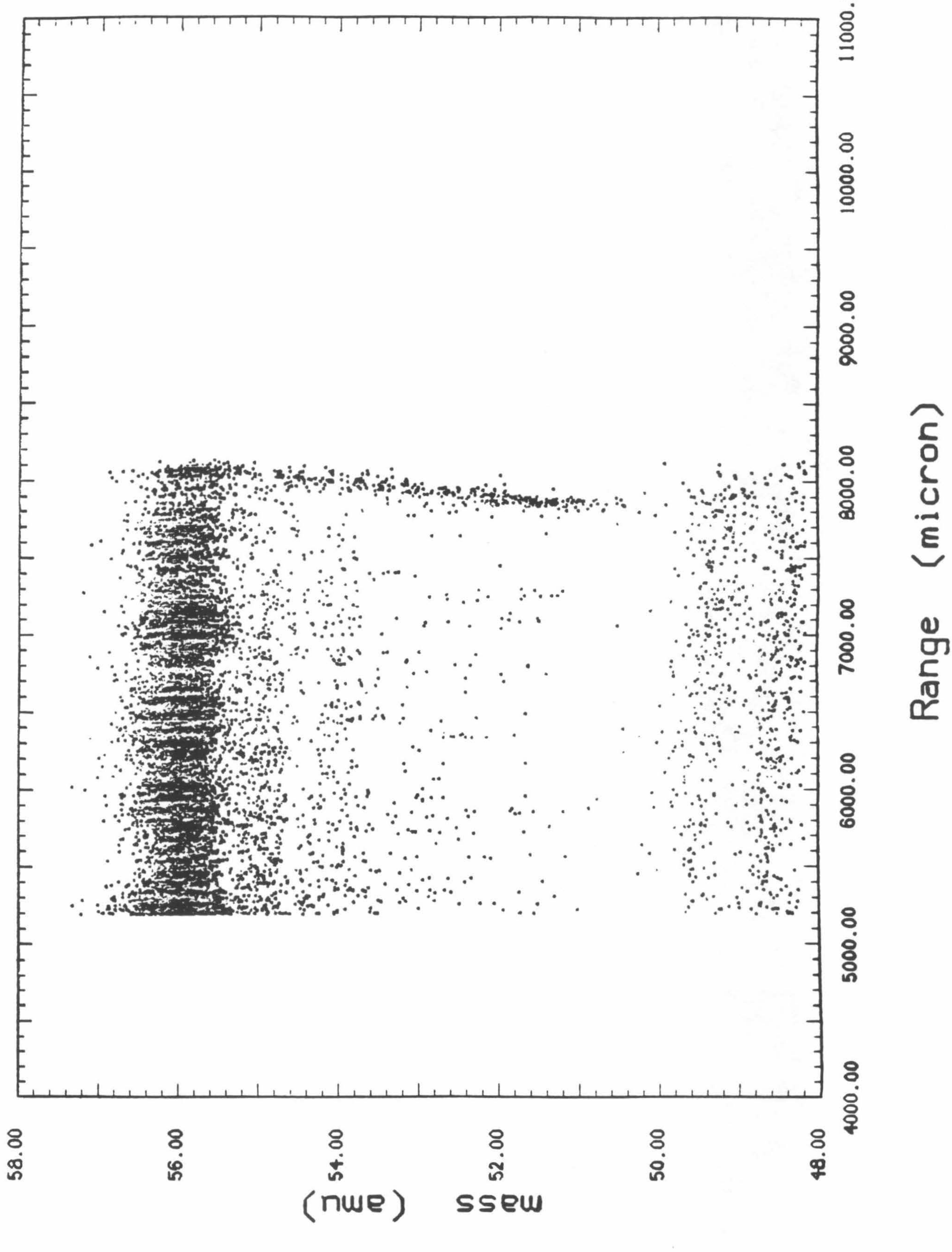
mass (amu)
58.00
56.00
54.00
52.00
50.00
48.00
Range (micron)
4000.00
5000.00
6000.00
7000.00
8000.00
9000.00
10000.00
11000.0

Table 3.8

Range for Detectors D5 through D8 (μm)

Detector	Available		Analyzable	
	min.	max.	min.	max.
D5	2200	5200	2300	5200
D6	5200	8200	5300	7800
D7	8200	14200	8300	13500
D8	14200	20200	14300	19500

Table 3.8 Available and analyzable range for detectors D5 through D8 of HIST. Range is measured from the top of detector D3.

3.3.2.3. Data Set Selection

When the HIST calibration data was taken, the thickness of the Cu absorber was systematically varied with time to obtain a distribution of ranges for the non-interacted ^{56}Fe beam particles within the HIST detector stack. Therefore, we can select the data to have the non-interacted ^{56}Fe particles stopping in a particular range by specifying the time interval which the data was taken. Before we can obtain the observed relative yields for comparison with the Monte Carlo calculation, we have to select a subset or subsets of the data so that the isotopes of interest stopped in detectors D5 through D8. By selecting the range of the non-interacted ^{56}Fe particles, we are indirectly specifying the restrictions on the range of the other isotopes. Before putting any limits on the ^{56}Fe range, we studied the relationships of the range of the different isotopes as a function of the range of non-interacted ^{56}Fe. In deriving these relationships, we assume that the fragments have the same energy per nucleon as the primary particle right after the interaction, and that range scales as A/Z^2. Figure 3.16 shows this kind of relationship for ^{49}Cr, ^{54}Cr, ^{51}Mn, ^{55}Mn, ^{53}Fe, and ^{55}Fe. Each plot shows the possible range of the isotope with the two lines being the limiting cases. One limiting case has the ^{56}Fe beam particles interacting upstream at the front end of the Cu absorber. The other limiting case has the ^{56}Fe beam particles interacting just before they entered detector D3.

In this study, we will compare the observed and calculated yields of the Cr, Mn, and Fe fragments. It is possible to choose a subset of the data with all of the fragments of interest stopping in detectors D5 through D8. However, this would put quite a restriction on our data selection (since the range of the Fe fragments is quite different from the range of the Cr fragments) and would yield a very small data subset. Instead we will select two

Figure 3.16

The range of isotopes (a) ^{49}Cr and ^{54}Cr, (b) ^{51}Mn and ^{55}Mn, and (c) ^{53}Fe and ^{55}Fe as a function of the non-interacted ^{56}Fe particles. Each plot shows the possible range of the isotope with the two lines being the limiting cases. One limiting case has the ^{56}Fe beam particles interacting upstream at the front end of the Cu absorber. The other limiting case has the ^{56}Fe beam particles interacting just before they entered detector D3.

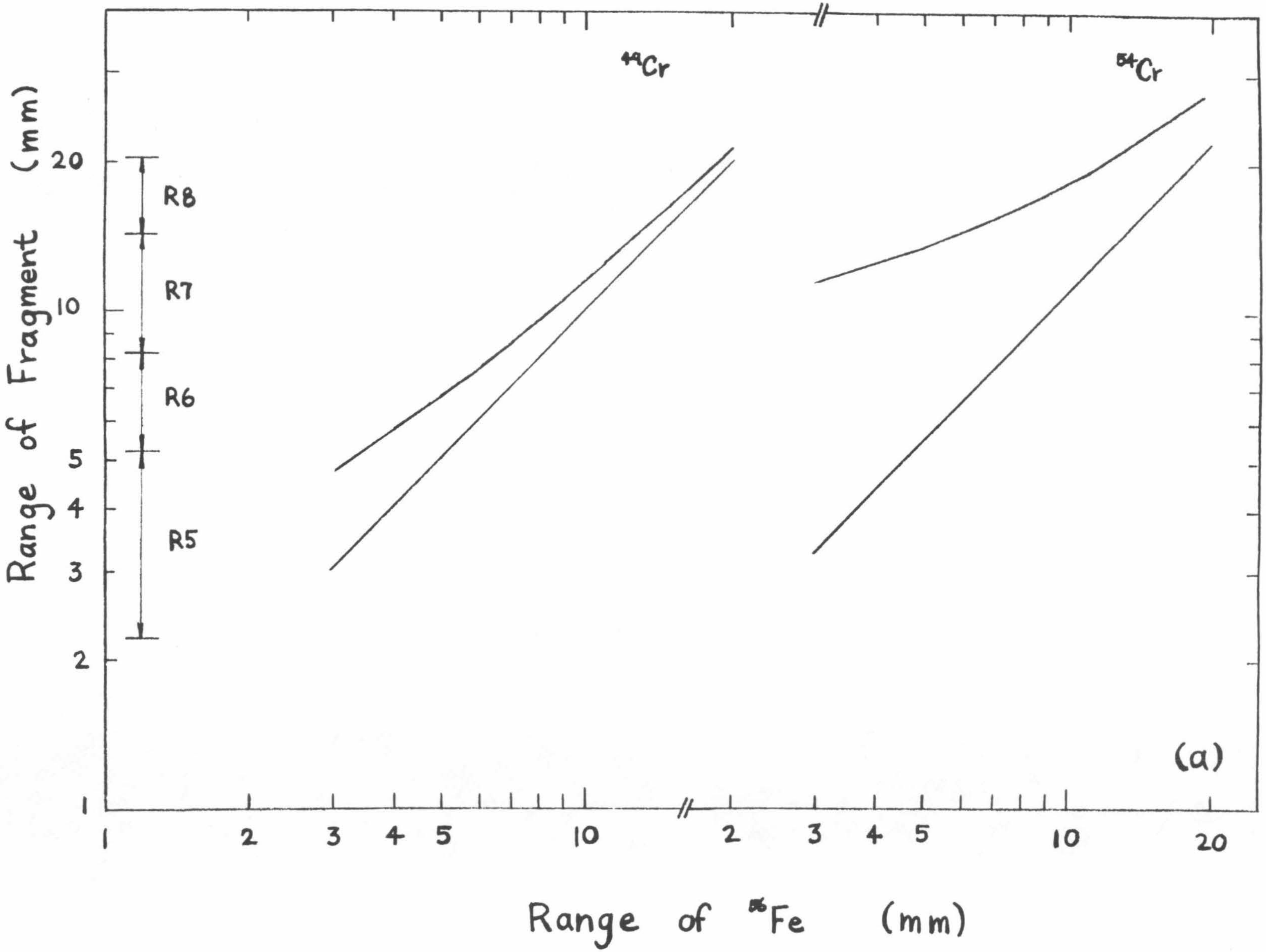
^{49}Cr
^{54}Cr
(a)
R8
R7
R6
R5
Range of Fragment (mm)
1
2
3
4
5
10
20
Range of ^{56}Fe (mm)
1
2
3
4
5
10
2
3
4
5
10
20

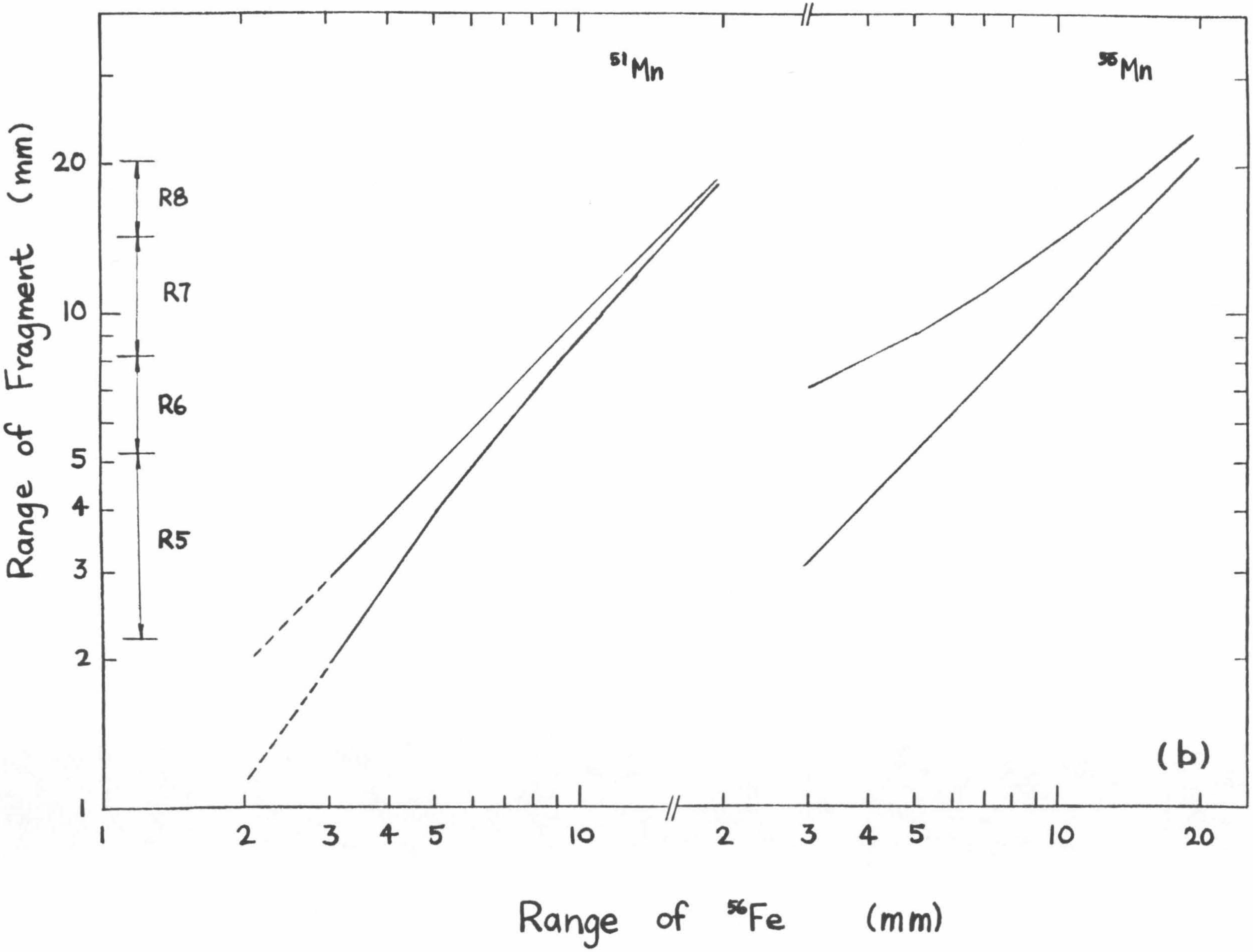
^{51}Mn
^{58}Mn
(b)
Range of Fragment (mm)
20
10
5
4
3
2
1
R8
R7
R6
R5
1
2
3
4
5
10
2
3
4
5
10
20
Range of ^{56}Fe (mm)

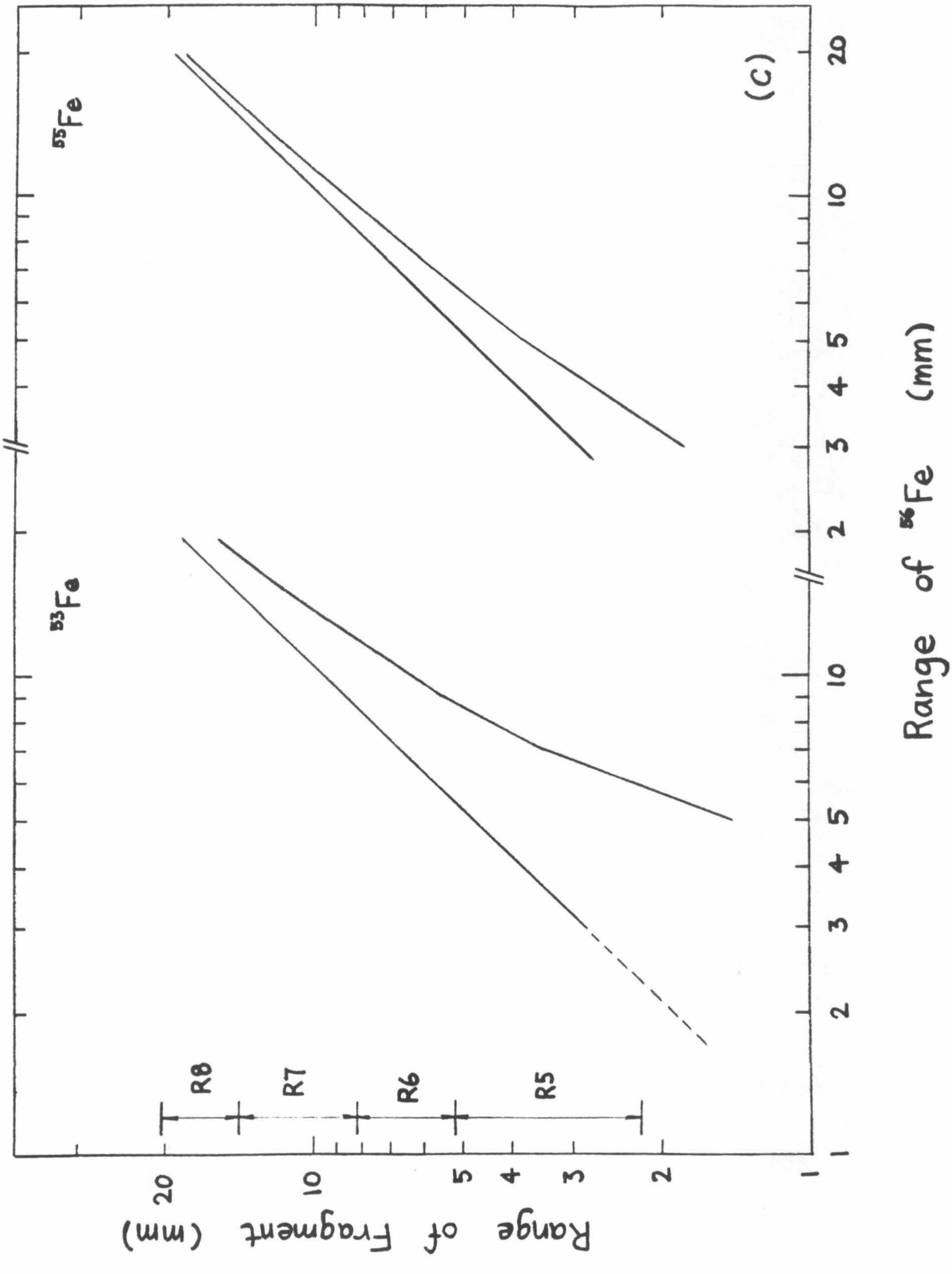
(c)
^{53}Fe
^{55}Fe
R8
R7
R6
R5
Range of ^{56}Fe (mm)
Range of Fragment (mm)
1
2
3
4
5
10
20
2
3
4
5
10
2
3
4
5
10
20

data subsets. One subset will have all the Cr and Mn fragments stopping in D5 through D8 and the other subset will have all the Mn and Fe fragments stopping in D5 through D8. The two subsets will be normalized using the total number of Mn fragments in each of the subsets. To select the data subsets, we will look at the isotopes with the longest and shortest ranges in each subset. In the first subset the isotope with the longest range is ^{54}Cr. Using figure 3.16a, the ^{56}Fe beam particles should stop with range less than 11800μm if we want all ^{54}Cr fragments to stop before exiting D8. The isotope with the shortest range is ^{51}Mn (ignoring ^{50}Mn since it does not have a significant contribution). Using figure 3.16b, the ^{56}Fe beam particles should stop with range greater than 3250μm if we want all ^{51}Mn fragments to reach D5. Using this analysis we have restricted our first data subset to have the ^{56}Fe beam particles stop with range greater than 3250μm and less than 11800μm. Doing similar analysis for the second data subset (with ^{53}Fe and ^{55}Mn) the ^{56}Fe beam particles were restricted to have range greater than 5800μm and less than 16000μm. Figure 3.17 shows the range distributions of the ^{56}Fe beam particles for the two data subsets. In each case we were trying to maximize the number of events we could use in our analysis without allowing a significant number of interesting events to stop outside D5 through D8.

3.3.2.4. Observed Isotope Yields

Now we are ready to obtain the observed isotope yields. For each of the data subsets, we calculated two masses for each of the events with the corrections (as discussed in section 3.4.2.1) applied. Background and "fold-back" events were rejected as described in section 3.4.2.2. Now for each of the 4 ranges (Range 5 through 8), we obtained a mass histogram, of the weighted sum of the two calculated masses, for each of the elements of

Figure 3.17

Range distributions of the ^{56}Fe beam particles for (a) data subset 1 with all Cr and Mn fragments stopping in D5 through D8, and (b) data subset 2 with all Mn and Fe fragments stopping in D5 through D8. The peaks are due to the discrete steps in thickness of the Cu absorbers.

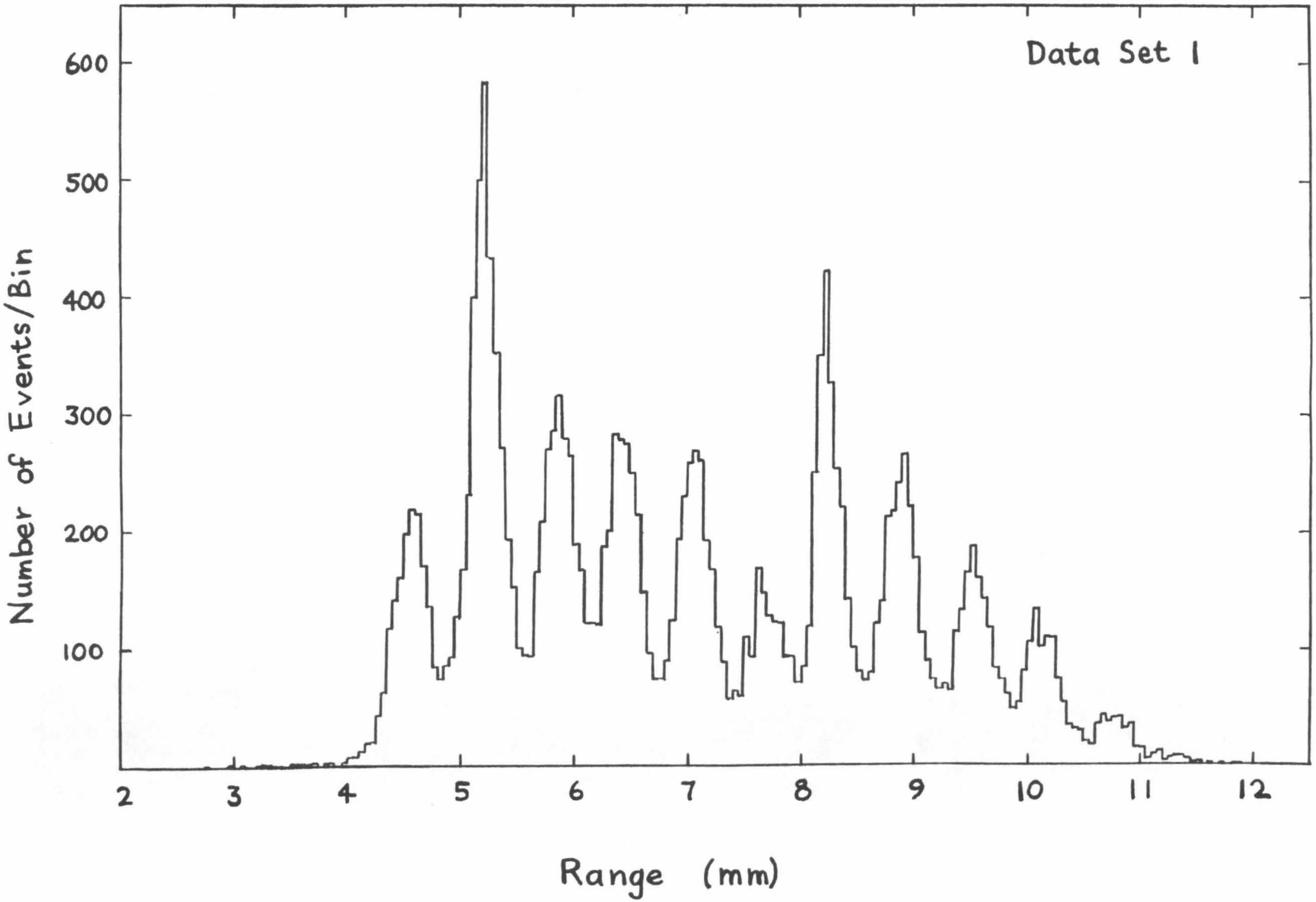
Data Set 1
Number of Events/Bin
600
500
400
300
200
100
2
3
4
5
6
7
8
9
10
11
12
Range (mm)

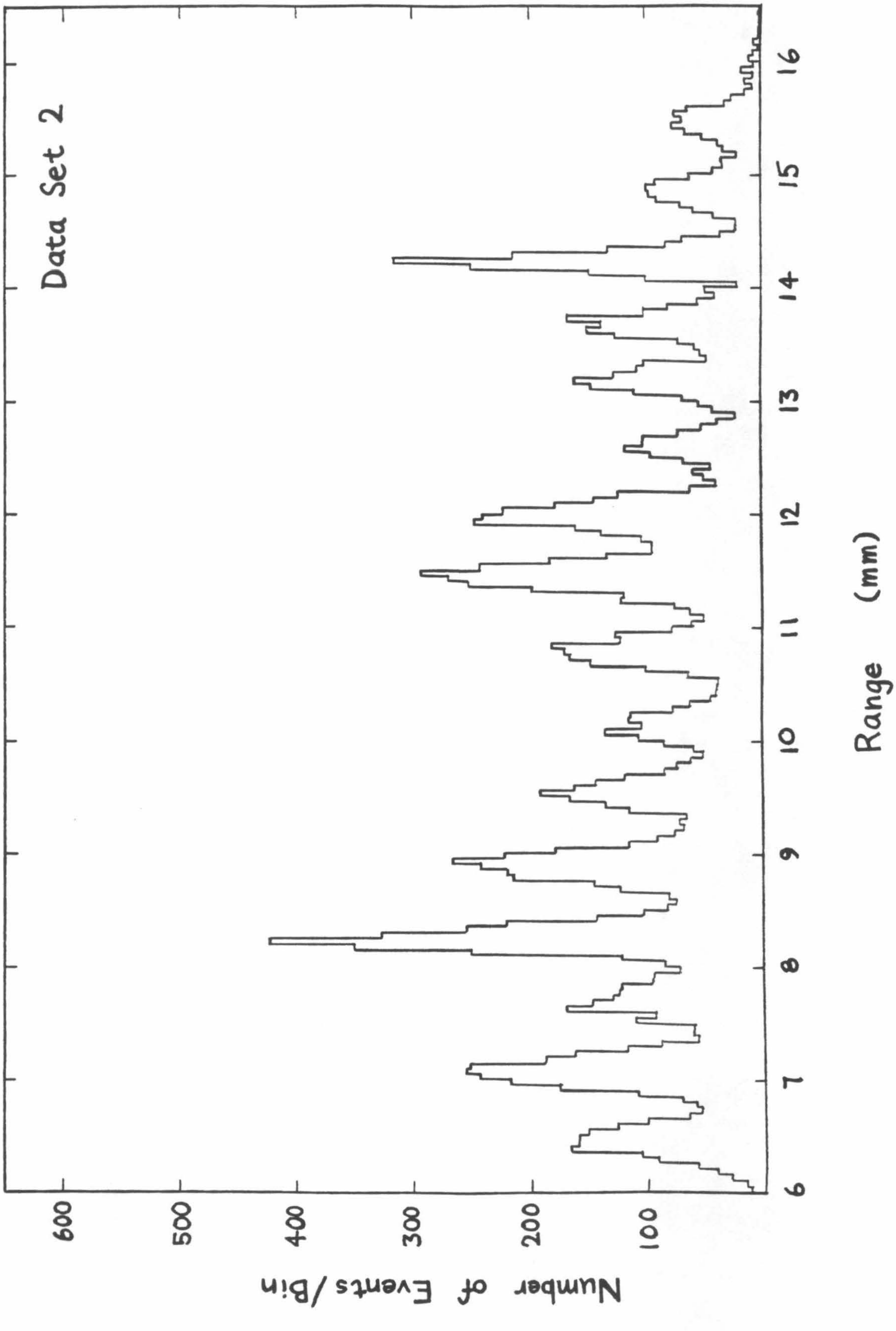
Data Set 2
Number of Events/Bin
100
200
300
400
500
600
Range (mm)
6
7
8
9
10
11
12
13
14
15
16

interest in the data subset. Gaussian distributions were then fitted to each of the mass histograms using the least-squares fit method described in Chapter 11 of Bevington (1969). In each fit, the gaussian distributions were assumed to have the same widths; and the separation of one distribution from the next was also assumed to be the same. The whole group of gaussian distributions was allowed to shift on the mass scale to optimize the fit. The free parameters in the least-squares fit were the individual heights, the width, the separation, and the overall location of the gaussian distributions. Figure 3.18 shows such fits to mass histograms, for Cr, Mn, and Fe fragments stopping in detector D6, as well as for Mn fragments stopping detectors D8, D7, and D5. From these least-squares fits, the mass resolutions for Mn are 0.22, 0.26, 0.22, and 0.32 amu for particles stopped in detector D8, D7, D6, and D5 respectively.

Using the least-squares fit calculations, we obtained the number of each isotope stopping in the analyzable range of each detector. The least-squares fit also calculated the uncertainties in the number of each isotope. To get the total observed abundances, the results from each of the 4 ranges were added together and their respective uncertainties were added in quadrature. To estimate the number of each isotopes stopped in the non-analyzed ranges, we analyzed the mass histograms for the 500 μm segments before and after the non-analyzed ranges. Least-squares fits were performed on each of these mass histograms to get the number of each isotopes in these 500 μm detector segments and the uncertainties. These numbers were then used to estimate the number of fragments stopped in the 100 μm, 500 μm, and 800 μm of non-analyzed ranges between detectors. Uncertainties in these estimates were also calculated. The statistical uncertainty in the estimate was then added to the respective estimation uncer-

Figure 3.18

Least-squares fits to mass histograms for (a) Fe fragments, (b) Mn fragments, and (c) Cr fragments which stopped in detector D6. Figures 3.18(d) through 3.18(f) are least-squares fits to mass histograms for Mn fragments stopped in detectors D8, D7, and D5 respectively. The mass histograms were fitted with gaussian distributions each representing an isotope. In each fit, the gaussian distributions were assumed to have the same width; and the separation of one distribution from the next was also assumed to be the same (approximately, but not necessarily 1 amu). The whole group of gaussian distributions was allowed to shift on the mass scale to optimize the fit. The free parameters in the least-squares fit were the individual heights, the width, the separation, and the overall location of the gaussian distributions.

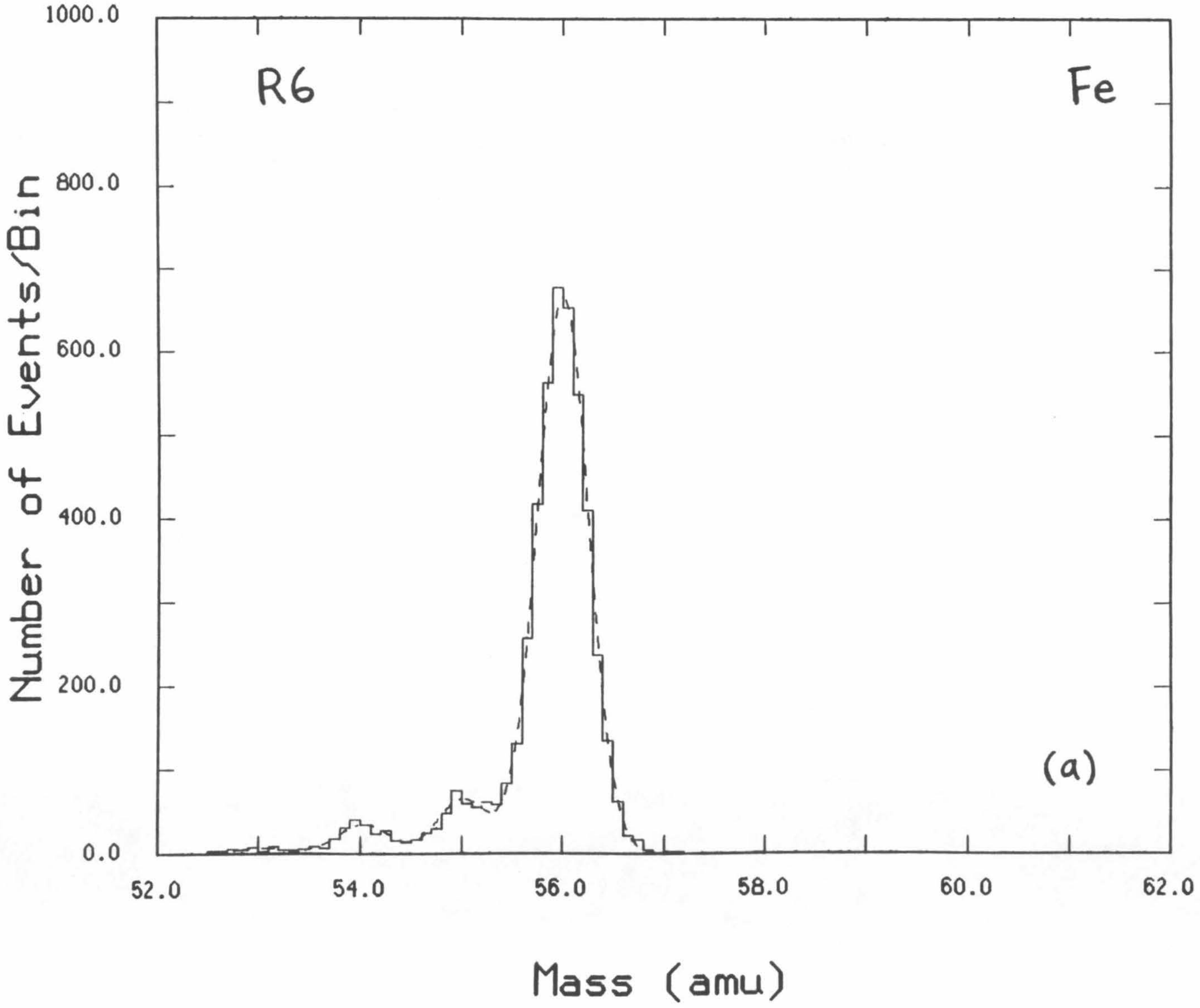
R6
Fe
(a)
Number of Events/Bin
0.0
200.0
400.0
600.0
800.0
1000.0
52.0
54.0
56.0
58.0
60.0
62.0
Mass (amu)

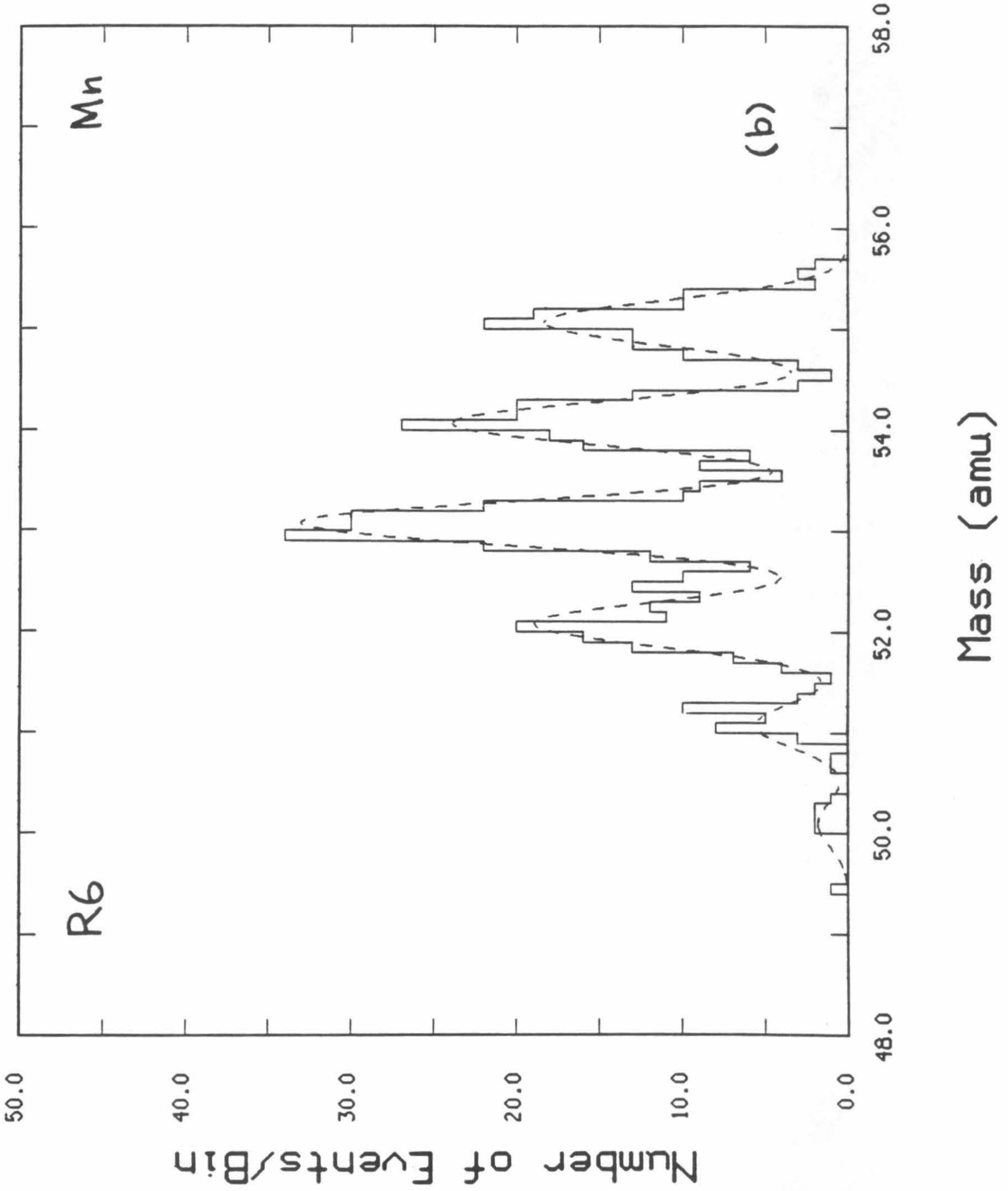
R6
Mn
(b)
Number of Events/Bin
0.0
10.0
20.0
30.0
40.0
50.0
Mass (amu)
48.0
50.0
52.0
54.0
56.0
58.0

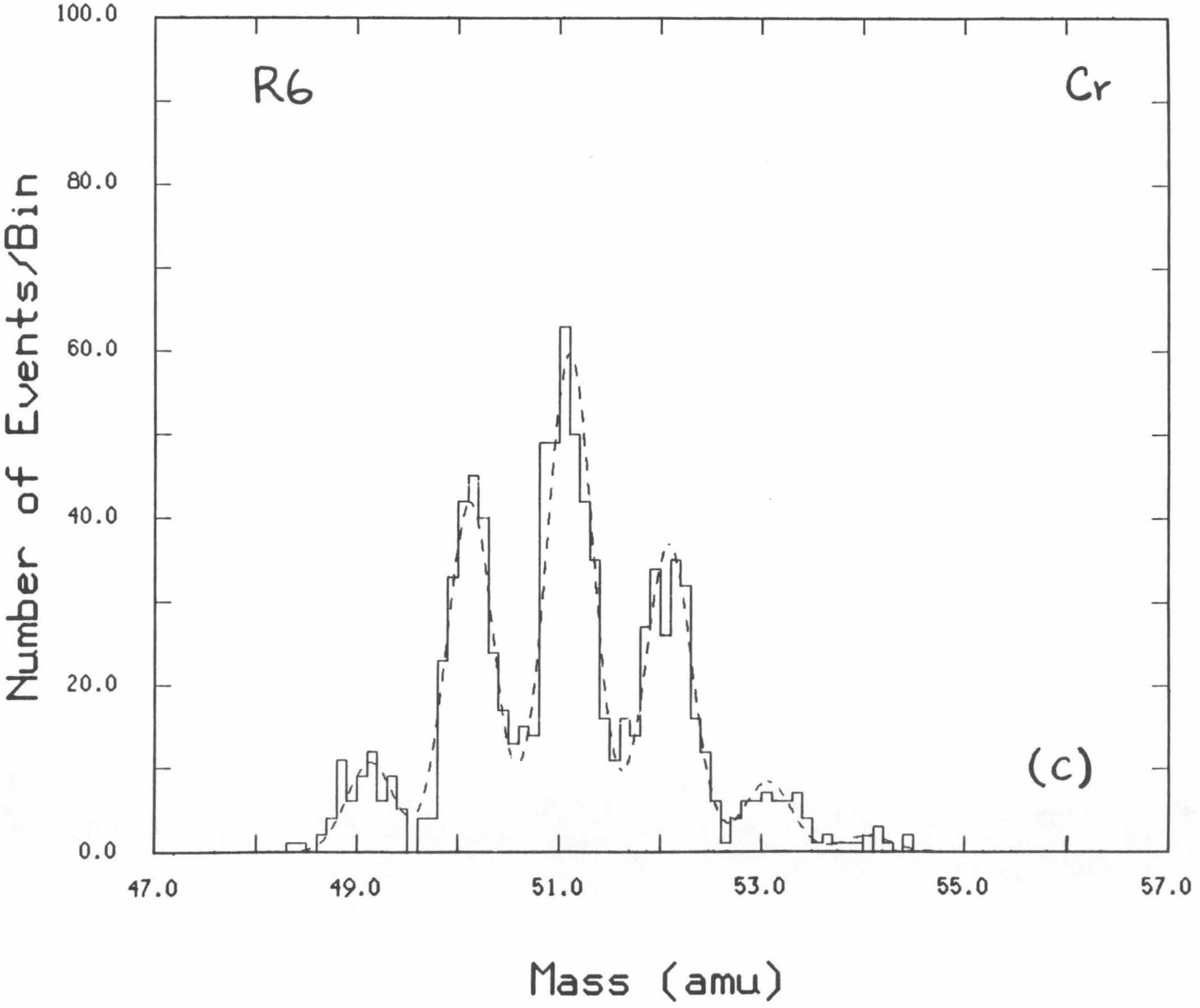
R6
Cr
(c)
Number of Events/Bin
100.0
80.0
60.0
40.0
20.0
0.0
47.0
49.0
51.0
53.0
55.0
57.0
Mass (amu)

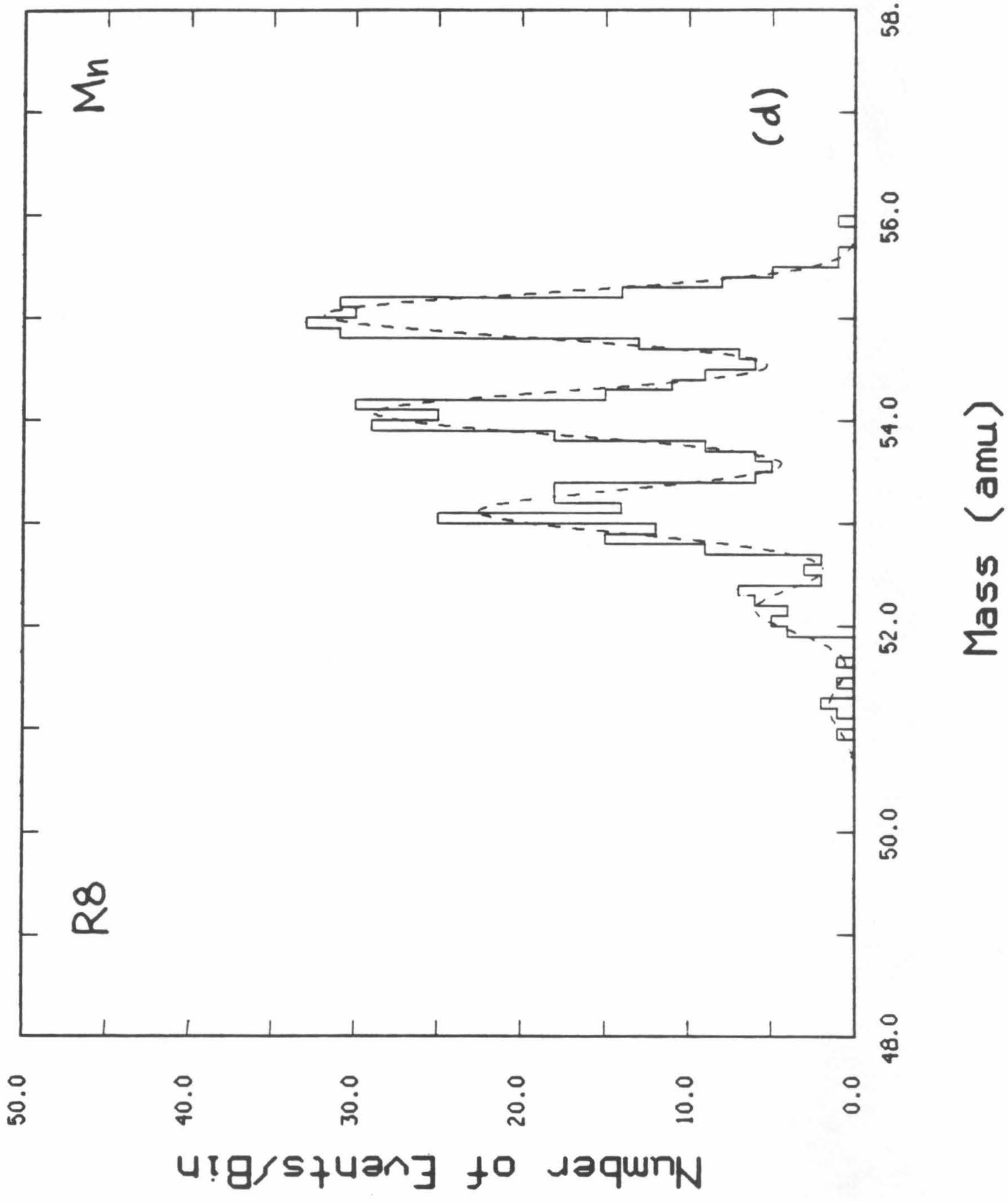
R8
Mn
(d)
Number of Events/Bin
0.0
10.0
20.0
30.0
40.0
50.0
Mass (amu)
48.0
50.0
52.0
54.0
56.0
58.0

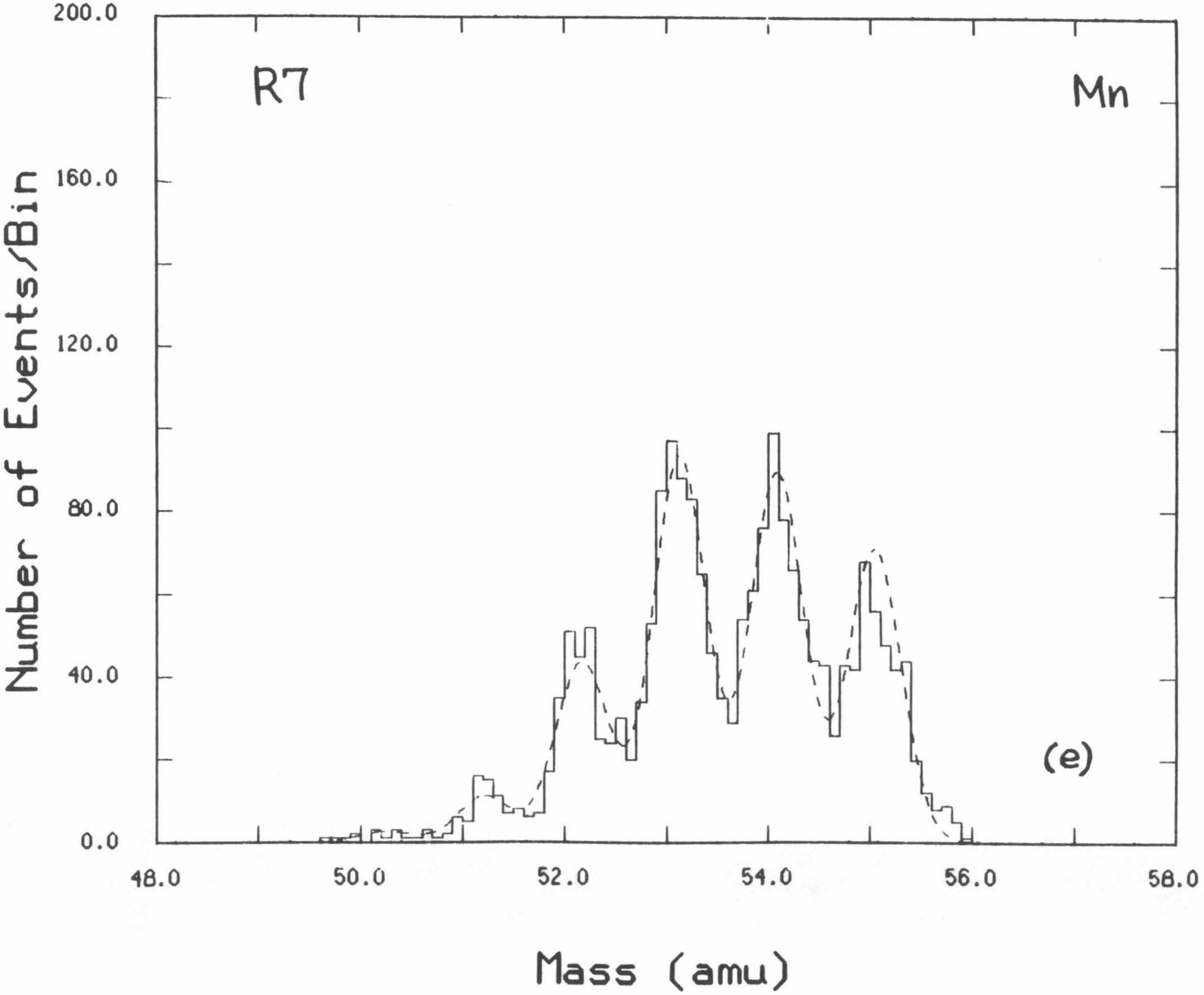
R7
Mn
(e)
Number of Events/Bin
0.0
40.0
80.0
120.0
160.0
200.0
48.0
50.0
52.0
54.0
56.0
58.0
Mass (amu)

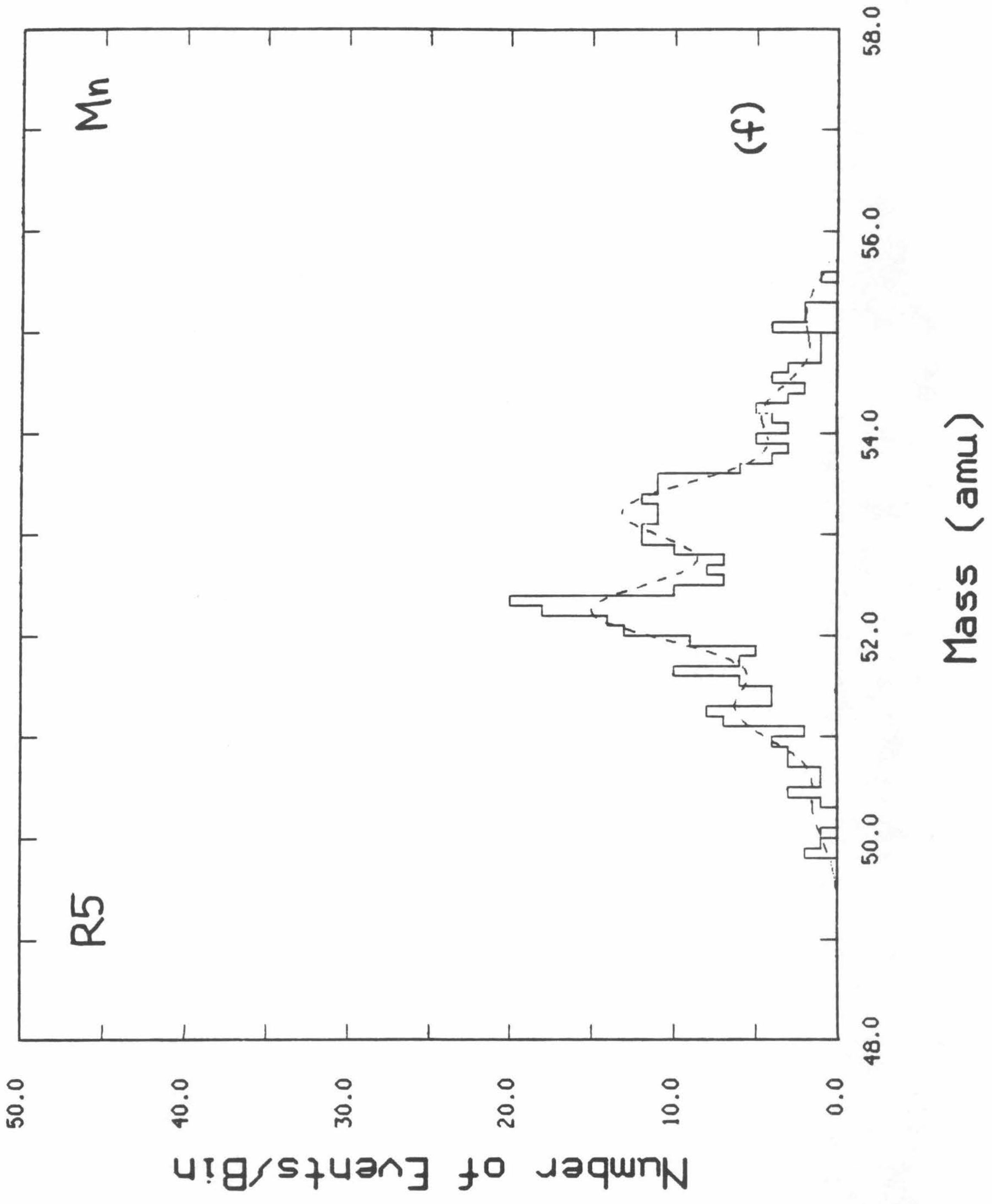
Mn
R5
(f)
Number of Events/Bin
0.0
10.0
20.0
30.0
40.0
50.0
Mass (amu)
48.0
50.0
52.0
54.0
56.0
58.0

tainty in quadrature. Table 3.9 shows the results of the least-squares fits. The table contains the measured isotope yields for the two data subsets along with the estimates for fragments stopped in the non-analyzed ranges. These results will be normalized and compared to the Monte Carlo calculations in the next section.

We have also analyzed the Co events for the second data subset because the Monte Carlo calculations suggest that there might be observable yields of ^{56}Co and ^{55}Co. Figure 3.19 shows the individual mass histograms for each of the 4 ranges as well as the combined mass histogram. The large peak to the left is due to Fe events, in this case analyzed with an assumed Z of 27. The Fe events do not seem to contaminate the Co events except possibly in Range 5. Even in Range 5, it does not appear that the Fe distribution extends out beyond 53 amu. Because of the limited number of events, no Co track was seen on the mass vs. range plots. As a result, the g(E1) correction (as described by equation 3.12) could not be obtained directly. Instead, we used the Fe correction functions to approximate the g(E1)s for Co. The energy scale of the Fe correction functions was scaled properly using the range energy relationship. This approximation was shown to be reasonably good when Mn corrections were scaled for Fe events, giving a typical mass resolution about 50% worse than if the actual corrections were used. Because of the limited number of events in each range, we did not perform a least-squares fit on the histograms. As a result, the mass scale was not optimized both relatively and absolutely (this was done in the least-squares fit); and when the individual histograms were summed to form the combined histogram, it is possible that the mass resolution was further degraded. There is no evidence for individual isotope peaks for Co, possibly because of the degraded mass resolution and limited statistics. In any case, the isotope

Table 3.9

Isotope	Data Set 1		Data Set 2	
	Analyzable Range	Non-anal. Range [a]	Analyzable Range	Non-anal. Range [a]
^{56}Co	--	--	8.6±6.0	--
^{55}Co	--	--	11.9±6.5	--
^{55}Fe	--	--	1460.9±50.4	178.1±20.4
^{54}Fe	--	--	598.5±29.5	69.0±12.4
^{53}Fe	--	--	126.5±16.6	14.4± 8.1
^{52}Fe	--	--	<37.0 [b]	--
^{55}Mn	645.7±26.4	80.7±12.8	751.5±24.6	86.6±14.5
^{54}Mn	884.8±33.1	81.2±12.4	896.6±35.7	123.8±17.0
^{53}Mn	950.7±35.3	77.3±11.8	983.3±37.7	127.2±17.1
^{52}Mn	459.6±25.7	32.4± 8.1	473.2±27.0	49.8±12.2
^{51}Mn	125.3±14.5	2.9± 3.2	135.0±17.4	8.6± 7.1
^{50}Mn	34.7± 9.9	--	37.4±11.3	--
^{54}Cr	64.0±11.5	7.1± 7.2	--	--
^{53}Cr	223.0±19.5	19.6± 9.5	--	--
^{52}Cr	721.0±30.8	86.6±14.5	--	--
^{51}Cr	779.9±33.3	84.0±14.3	--	--
^{50}Cr	545.4±28.4	56.0±11.3	--	--
^{49}Cr	144.5±17.8	14.8± 7.1	--	--

[a] Estimated number of fragments which stopped in the non-analyzed range (100 μm between D5 and D6, 500 μm between D6 and D7, and 800 μm between D7 and D8). The estimates are based on analysis of the mass histograms for the 500 μm detector segments before and after the non-analyzed ranges.

[b] ^{52}Fe was not fitted in the least-squares fits. The number of events is counted from the mass histograms between 51.5 amu and 52.5 amu. This will include background events and events from the tail of the ^{53}Fe distribution.

Table 3.9 Measured isotope yields for the two data subsets along with the estimates for fragments which stopped in the non-analyzed ranges. The measured yields are the results of the least-squares fits.

Figure 3.19

Individual mass histograms for each of the 4 ranges, and combined mass histograms (sum of individual mass histograms) for Co events. The large peak to the left is due to Fe events, in this case analyzed with an assumed Z of 27. The Fe events do not seem to contaminate the Co events except possibly in range 5.

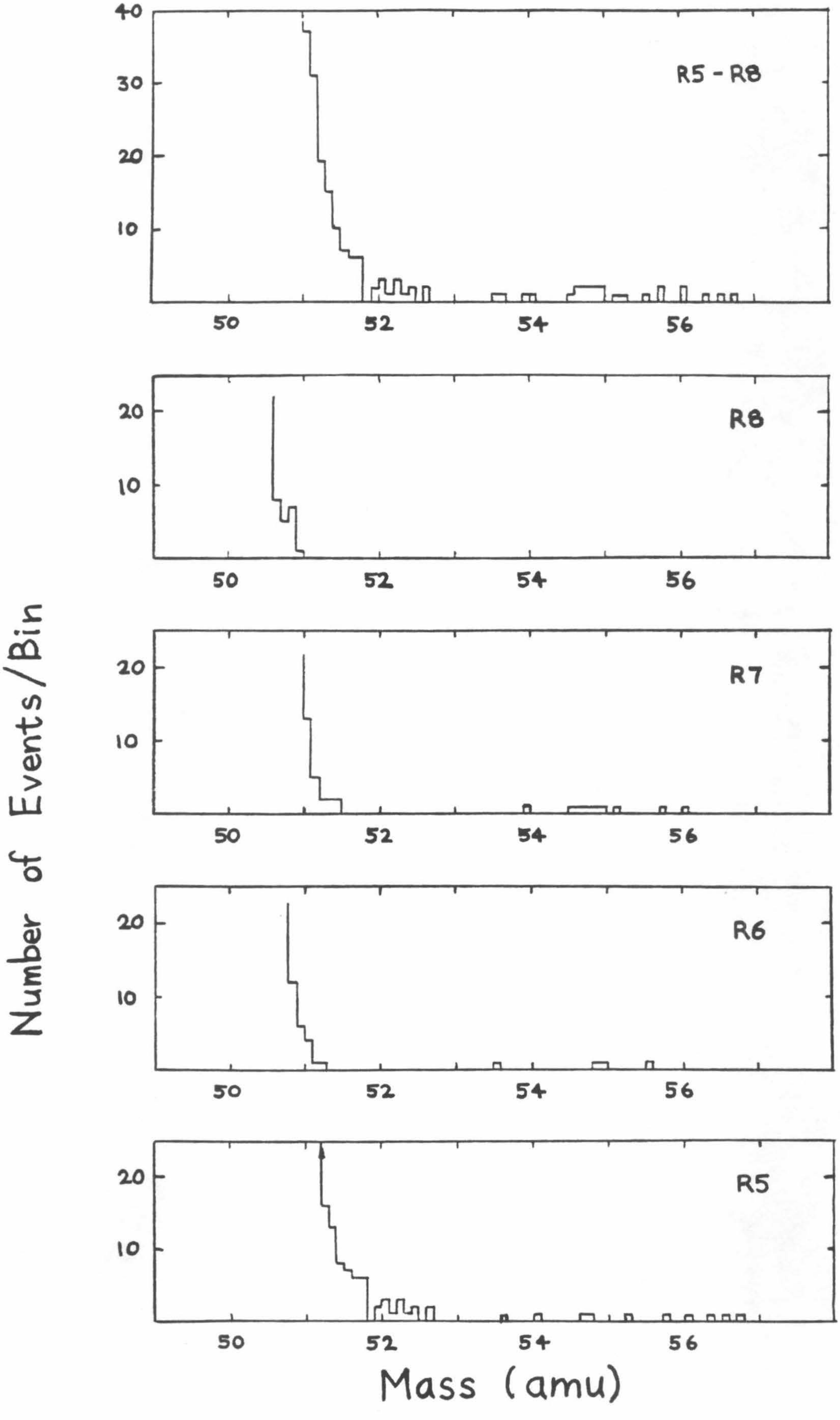
R5 - R8
40
30
20
10
50
52
54
56
R8
20
10
50
52
54
56
R7
20
10
50
52
54
56
R6
20
10
50
52
54
56
R5
20
10
50
52
54
56
Number of Events/Bin
Mass (amu)

yields were estimated by counting the number of events which fell in the intervals between 54.2 amu and 55.5 amu for ^{55}Co and between 55.5 amu and 56.8 amu for ^{56}Co. Using this counting scheme, we counted 11 ^{55}Co and 8 ^{56}Co. We estimated the corrections for the non-analyzed ranges for the Co events to be ~5%, somewhat less than for the other elements. Note that the 800 μm of non-analyzed range between detectors D7 and D8 constituted more than half of the thickness of the non-analyzed ranges; and the number of Co events stopped in this 800 μm segment would be insignificant because Co events had shorter ranges than the other fragments. The number of Co events that stopped before reaching detector D5 was estimated to be 3±2% for ^{55}Co and 2±1% for ^{56}Co by the Monte Carlo calculations. Based on the Monte Carlo calculation, no ^{54}Co was expected; whereas there were 4 possible candidates for ^{54}Co. These might be background events or they could be Fe events. Since there were no possible candidates for ^{58}Co, even if these 4 ^{54}Co candidates were due to background, one cannot use this as an indication of the background level for either ^{55}Co or ^{56}Co. In fact, these 4 events could be ^{55}Co and some of the identified ^{55}Co events could be ^{56}Co due to the poor resolution and possible shift of the mass scale. Therefore, we average the 4 possible ^{54}Co and 0 ^{58}Co, and add 2 to the uncertanties to include this possible systematic uncertainty. When these corrections are applied, the best estimates are 11.9±6.5 for ^{55}Co and 8.6±6.0 for ^{56}Co.

Perron (1976) measured the decayed cross-sections for Cr and Mn isotopes from fragmentation of ^{56}Fe by bombarding a ^{56}Fe target with 600 MeV protons. We have decayed our observed isotope yields and compared them with the decayed cross-sections measured by Perron. The comparison shows that our relative isotope yields are consistent with their cross-sections.

When selecting the data subsets, we were trying to maximize the number of events we could analyze without allowing a significant number of interesting events to stop outside D5 through D8. To make sure this objective is met, the range profile was plotted for each of the isotopes with the exception (because of limited statistics) of ^{50}Mn, ^{55}Co, and ^{56}Co. Figure 3.20 shows the range profiles. Each data point represents the number of events which stopped in a 500 μm segment of detector range. Extrapolating from the range profiles, there does not appear to be significant number of interesting events which stopped outside D5 through D8 ($2300\mu m <$ range $< 19500\mu m$).

Figure 3.20

Range profiles (measured) for each of the isotopes with the exception of ^{50}Mn, ^{55}Co, and ^{56}Co. Each data point represents the number of events which stopped in a 500 μm segment of detector range.

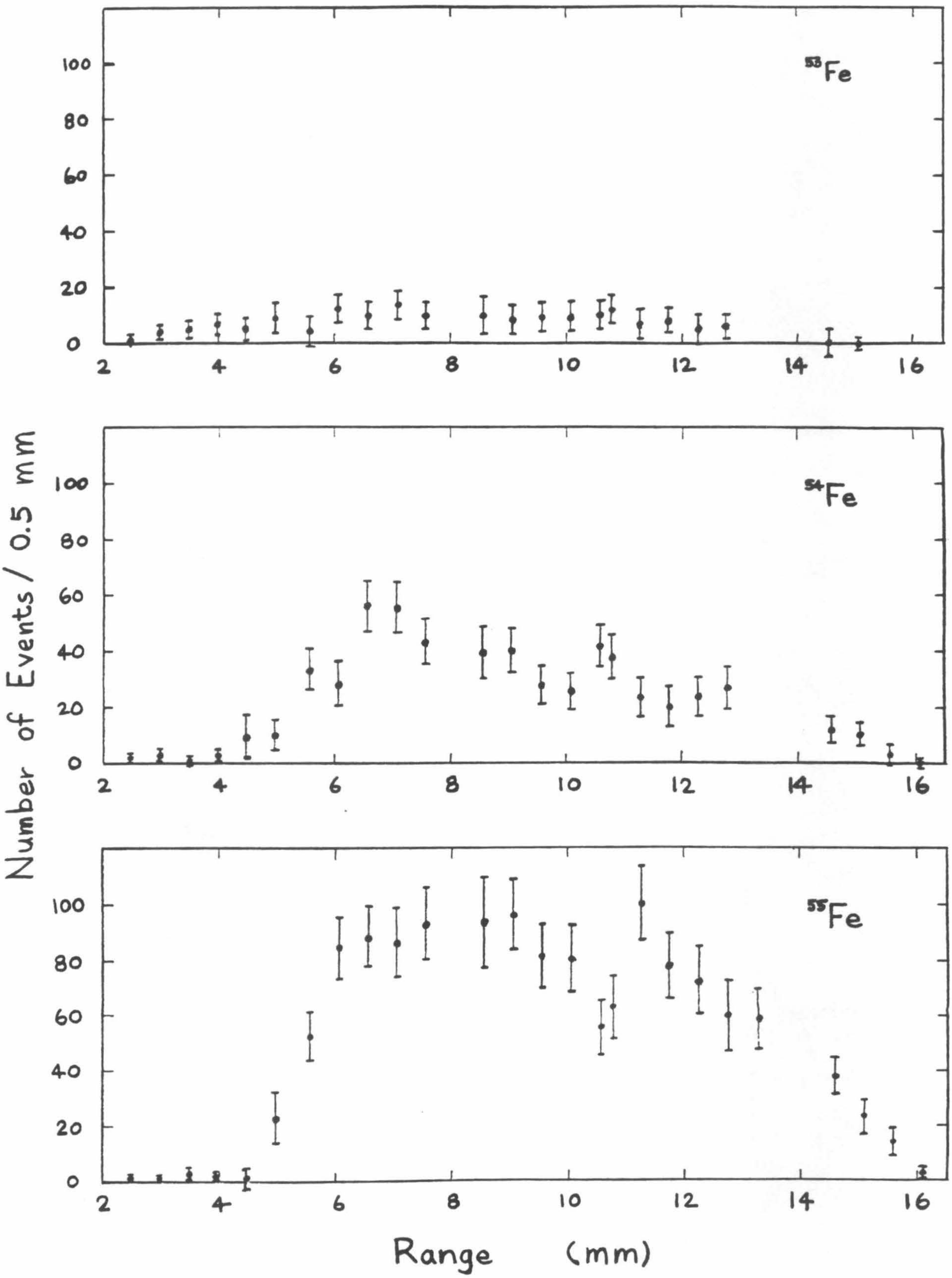
^{53}Fe
^{54}Fe
^{55}Fe
0
20
40
60
80
100
2
4
6
8
10
12
14
16
Number of Events / 0.5 mm
Range (mm)

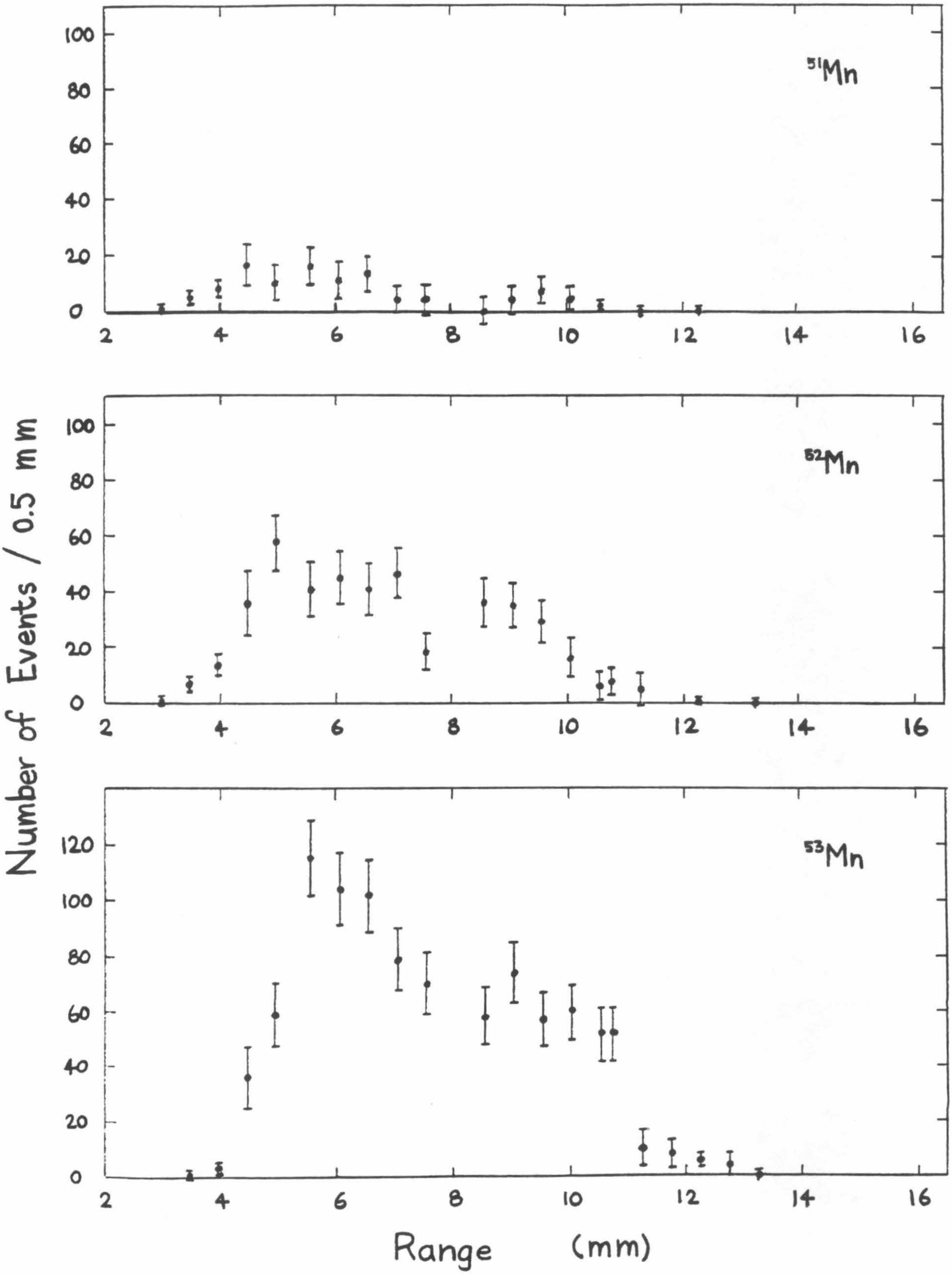

^{51}Mn
^{52}Mn
^{53}Mn
0
20
40
60
80
100
120
2
4
6
8
10
12
14
16
Number of Events / 0.5 mm
Range (mm)

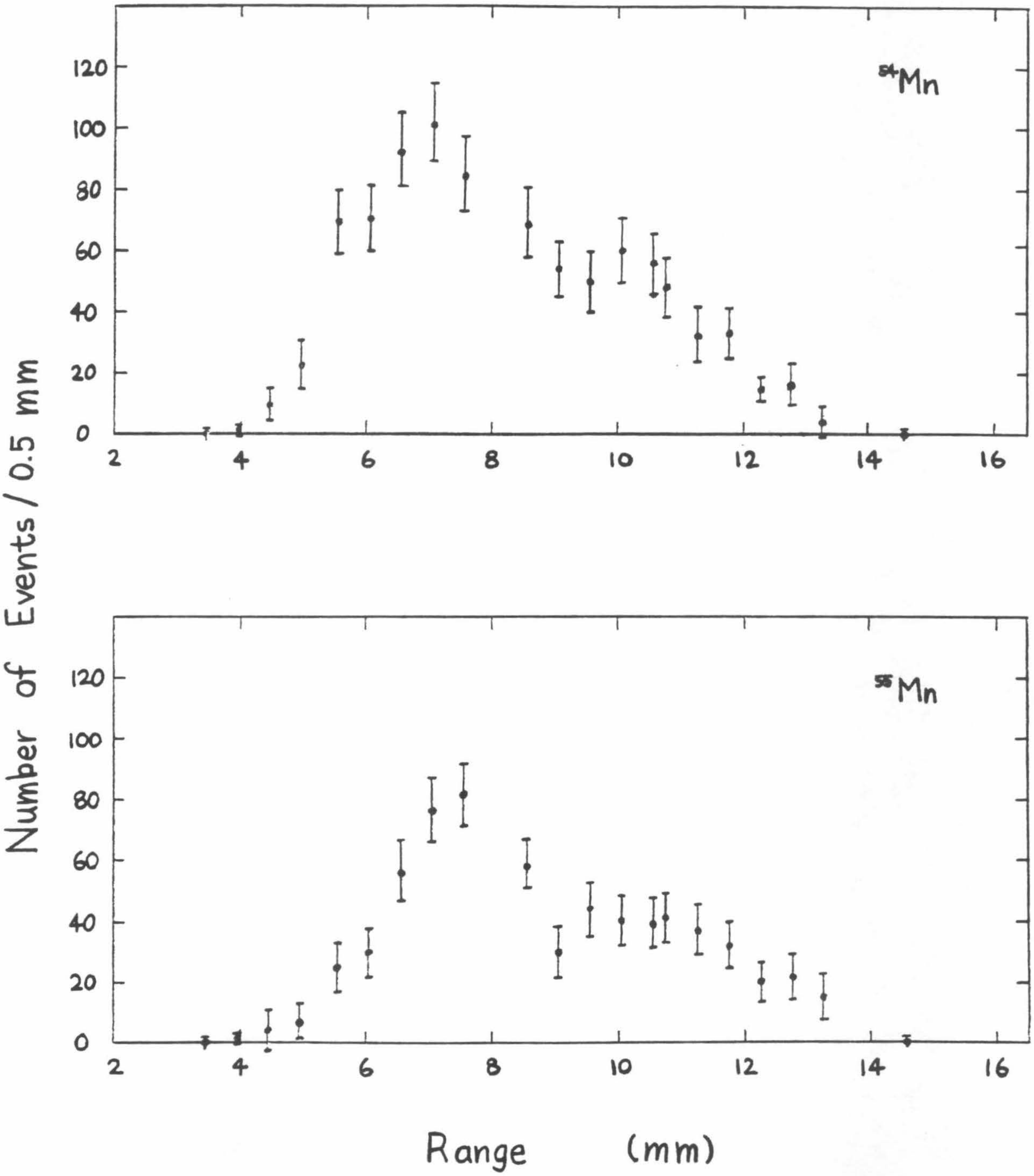
^{54}Mn
120
100
80
60
40
20
0
2
4
6
8
10
12
14
16
Number of Events / 0.5 mm
^{55}Mn
120
100
80
60
40
20
0
2
4
6
8
10
12
14
16
Range (mm)

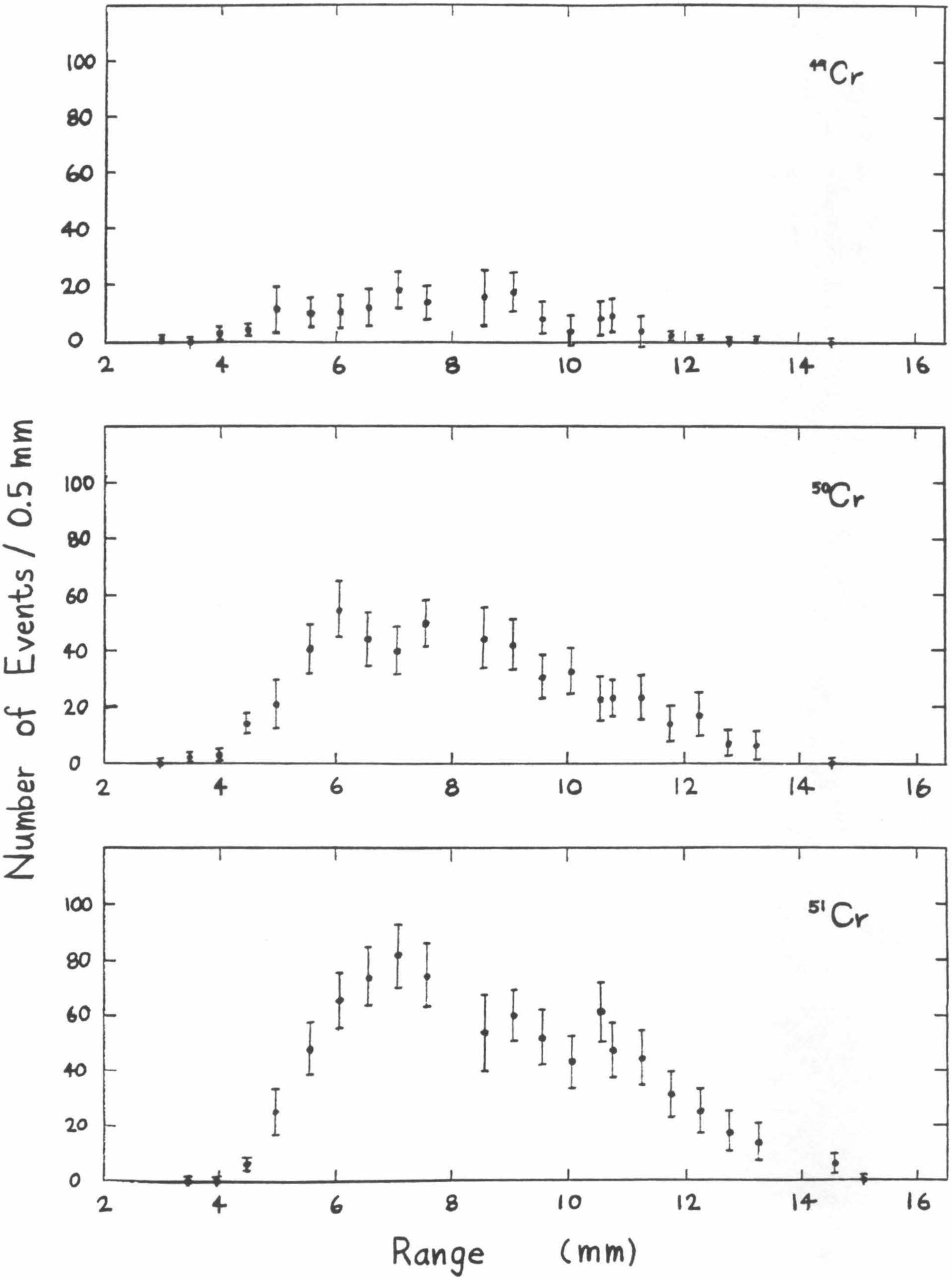
^{49}Cr
^{50}Cr
^{51}Cr
Number of Events / 0.5 mm
0
20
40
60
80
100
2
4
6
8
10
12
14
16
Range (mm)

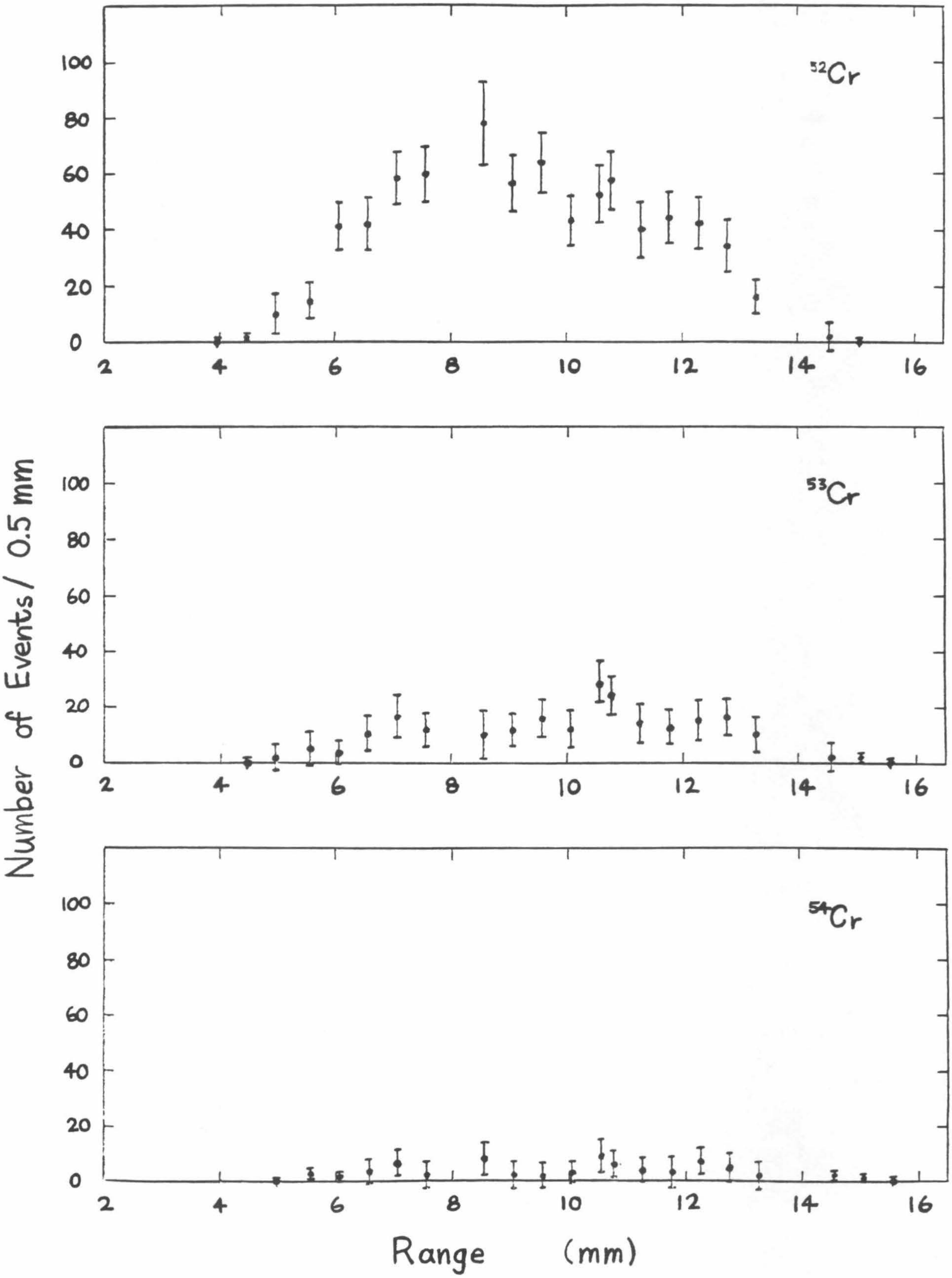
^{52}Cr
^{53}Cr
^{54}Cr
Number of Events / 0.5 mm
Range (mm)
0
20
40
60
80
100
2
4
6
8
10
12
14
16

3.3.3. Comparison with Calculations

The measured isotope yields presented in Table 3.9 were observed for a thick CH_2 target. The ^{56}Fe beam particles interacted in the target (or even outside the target) at various energies. In addition, fragments that were emitted at angles > 1° were generally not detected. As a result, we did not have a direct measure of the interaction cross-sections. However, as for the case of the ^{40}Ar fragmentation study, we can still test the semi-empirical cross-sections by comparing the observed relative yields with those expected from a Monte Carlo calculation based on the semi-empirical cross-sections of Silberberg and Tsao. The experimental setup was modeled in the Monte Carlo simulation. Table 3.10 gives a list of the materials modeled in the Monte Carlo calculation. The thickness of the Cu absorber was varied (from 0.52 g/cm^2 to 3.59 g/cm^2). The relative number of events we ran at each of the Cu thicknesses was deduced using the range distributions of figure 3.17. Interactions in the Cu absorber $\sim$ 10 m upstream are not included in our analysis because our efficiency is very low for detecting these fragments if they are emitted at an angle $\geq 0.2°$. According to the calculation, less than 5% of the interactions occurred in the Cu and their inclusion or exclusion does not affect the relative yields of the isotopes. We ran enough events in the calculation so that the statistical uncertainties of the calculated yields were small compared to the uncertainties of the observed yields.

The results of the Monte Carlo calculations are presented in Table 3.11. The calculated isotope yields are tabulated along with the observed yields for the two data sets. The observed yields were obtained from Table 3.9 by adding the contributions from both the analyzable range and the non-analyzable range. The uncertainties were added in quadrature.

Table 3.10

Slab Description	Thickness (g/cm^2)	Material Assumed (and mass fractions)
Variable Absorber	0.52-3.59	Cu (1.000)
Air	0.13	N (.745), O (.229), Ar (.026)
CH_2 Target	5.258	H (.143), C (.857)
Beam Spreader[a]	3.586	Al (1.000)
Air	0.32	N (.745), O (.229), Ar (.026)
MWPCs	0.025	H (.013), C (.192), O (.103), Ar (.692)
Telescope Window	0.0034	Al (1.000)
M1-D2	0.079	Si (1.000)
D3-D4	0.513	Si (1.000)
D5	0.700	Si (1.000)
D6	0.700	Si (1.000)
D7	1.400	Si (1.000)
D8	1.400	Si (1.000)
D9	0.700	Si (1.000)

[a] The beam spreader is a slab of Al with 1mm grooves cut in one section of the surface so that a monoenergetic beam which goes through the grooved section will have a distribution of energy for the exiting particles. However, when the data was taken, the beam spreader was not aligned correctly; and the beam did not go through the grooved section. As a result, the beam spreader is just a piece of Al absorber in this case.

Table 3.10 The list of materials modelled in the Monte Carlo Calculation.

Table 3.11

Isotope	Data Set 1		Data Set 2	
	Observed Yield	Calculated Yield	Observed Yield	Calculated Yield
^{56}Co	--	--	8.6±6.0	206
^{55}Co	--	--	11.9±6.5	100
^{55}Fe	--	--	1639.0±54.3	16056
^{54}Fe	--	--	667.5±32.0	8660
^{53}Fe	--	--	140.9±18.4	7643
^{52}Fe	--	--	<37.0 [a]	419
Fe_{total} [b]	--	--	2447.4±65.7	32359
^{55}Mn	726.4±29.3	7889	838.1±28.6	8175
^{54}Mn	966.0±35.4	11215	1020.4±39.5	11495
^{53}Mn	1028.0±37.2	6926	1110.5±41.4	7420
^{52}Mn	492.0±27.0	3954	523.0±29.6	4061
^{51}Mn	128.2±14.9	1263	143.6±18.8	1423
^{50}Mn	34.7± 9.9	265	37.4±11.3	290
Mn_{total}	3375.3±67.4	31512	3673.0±73.8	32864
^{54}Cr	71.1±13.6	886	--	--
^{53}Cr	242.6±21.7	4962	--	--
^{52}Cr	807.6±34.0	14376	--	--
^{51}Cr	863.9±36.2	10764	--	--
^{50}Cr	601.4±30.6	6009	--	--
^{49}Cr	159.3±19.2	1367	--	--
Cr_{total}	2745.9±66.5	38364	--	--

[a] ^{52}Fe was not fitted in the least-squares fits. The number of events is counted from the mass histograms between 51.5 amu and 52.5 amu. This will include background events and events from the tail of the ^{53}Fe distribution.

[b] Not including ^{52}Fe.

Table 3.11 Isotope yields (not normalized) for the two data sets.

The two data sets were then normalized using the total number of Mn fragments in each of the data sets. This normalization was done independently for the calculated and observed yields. For the observed yields, the second data set was scaled down by a factor of 0.92; and for the calculated yields, the second data set was scaled down by a factor of 0.96. These combined results are tabulated in columns 2 and 3 in Table 3.12. For comparison purposes, we normalized the calculated yields to the observed yields using the total number of Cr and Mn fragments. Column 4 gives the normalized calculated yields which were obtained by scaling column 3 by a factor of 11.42. These normalized calculated yields are plotted along with the observed yields (column 2) in figure 3.21. Column 5 gives the ratios of the observed yields to the calculated yields.

One noticeable difference between the observed and calculated yields is in the comparison of total elemental yields of Cr and Mn. The Monte Carlo calculation predicted higher total elemental yield for Cr than for Mn (a Mn to Cr ratio of 0.82). On the other hand, we observed more total elemental yield for Mn than for Cr (an observed Mn to Cr ratio of 1.23±.04). Webber et al. (1982) studied the fragmentation of ^{56}Fe in CH_2 targets and found a similar discrepancy when their results were compared with the Siberberg and Tsao cross-sections. Their studies were done at 710, 950, and 1050 MeV per nucleon. The Mn to Cr cross-section ratio was found to be 1.19±.03 and 1.28±.02 at average interaction energy of 660 and 980 MeV per nucleon respectively. Westfall et al. (1979) did a similar study with an H target at higher energy (1.88 GeV per nucleon) and found a similar discrepancy (an observed cross-section ratio of 1.59±.40). Poferl-Kertzman et al. (1983) also studied the fragmentation of ^{56}Fe in CH_2 at 960 MeV per nucleon and found similar discrepancy (an observed cross-section ratio of 1.43±.06). Our study

Table 3.12

Isotope	Observed Yield	Calculated Yield	Normalized Calc. Yield [a]	Ratio [b] (Obs./Calc.)
^{56}Co	7.9±5.5	197.5	17.3	0.46±.32
^{55}Co	10.9±6.0	95.9	8.4	1.30±.71
^{55}Fe	1506.2±49.9	15395.5	1348.7	1.12±.04
^{54}Fe	613.4±29.4	8303.7	727.4	0.84±.04
^{53}Fe	129.5±16.9	7328.6	642.0	0.20±.03
^{52}Fe	<34.0	401.8	35.2	<0.97
^{55}Mn	726.4±29.3	7889	691.1	1.05±.04
^{54}Mn	966.0±35.4	11215	982.4	0.98±.04
^{53}Mn	1028.0±37.2	6926	606.7	1.69±.06
^{52}Mn	492.0±27.0	3954	346.4	1.42±.08
^{51}Mn	128.2±14.9	1263	110.6	1.16±.13
^{50}Mn	34.7± 9.9	265	23.2	1.50±.43
$\mathrm{Mn_{total}}$	3375.3±67.4	31512	2760.4	1.22±.02
^{54}Cr	71.1±13.6	886	77.6	0.92±.18
^{53}Cr	242.6±21.7	4962	434.7	0.56±.05
^{52}Cr	807.6±34.0	14376	1259.4	0.64±.03
^{51}Cr	863.9±36.2	10764	942.9	0.92±.04
^{50}Cr	601.4±30.6	6009	526.4	1.14±.06
^{49}Cr	159.3±19.2	1367	119.8	1.33±.16
$\mathrm{Cr_{total}}$	2745.9±66.5	38364	3360.8	0.82±.02

[a] Calculated yields are normalized to observed yields using the total number of Cr and Mn fragments.

[b] Ratio of observed to calculated yields. Uncertainties only include uncertainties in the observed yields.

Table 3.12 Combined results from data sets 1 and 2.

Figure 3.21

A comparison of measured and calculated fragmentation yields, normalized to the same total yield of Cr and Mn fragments. The Co yields are magnified by a factor of 10.

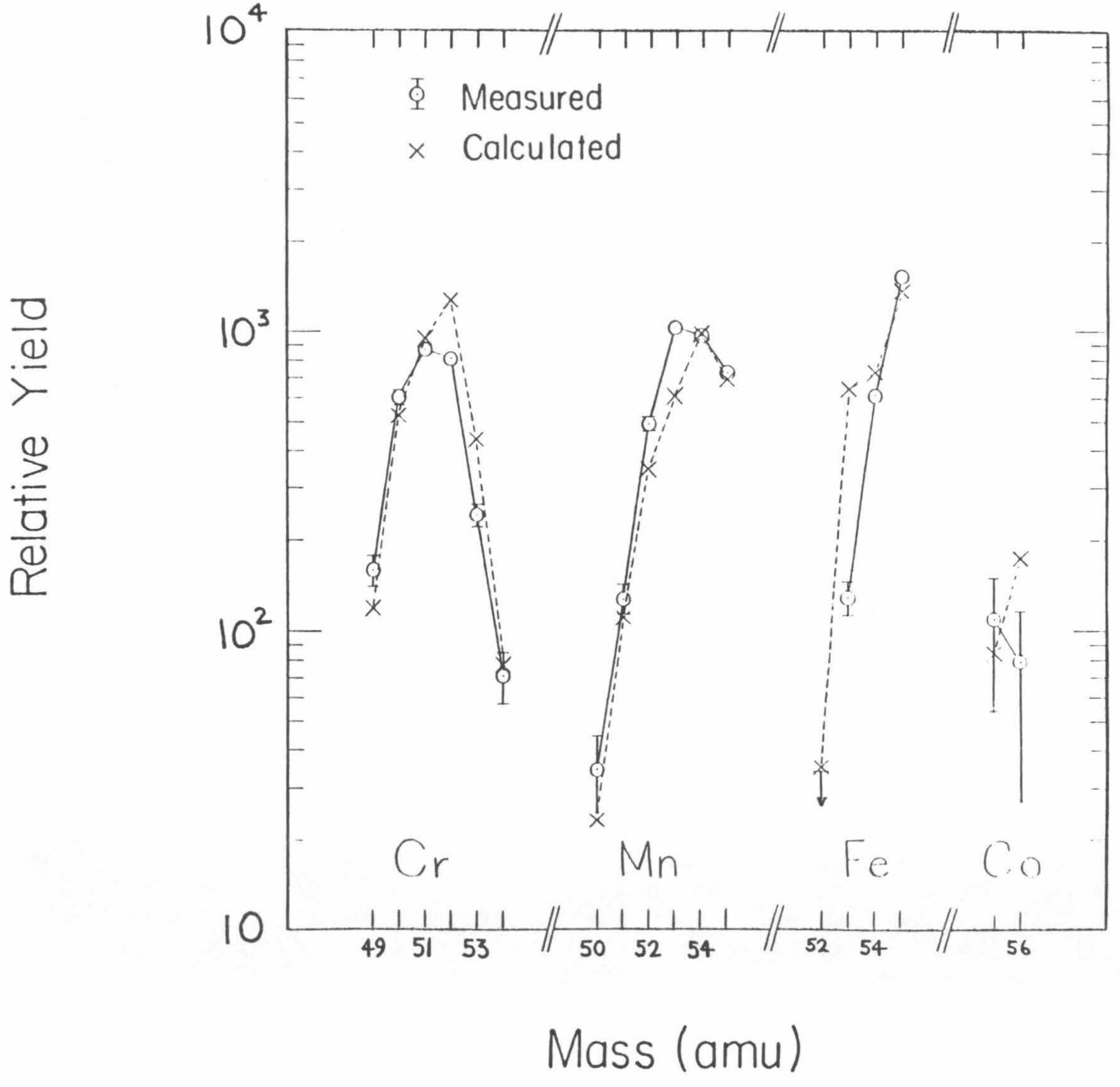
Measured
Calculated
Relative Yield
10^4
10^3
10^2
10
Cr
Mn
Fe
Co
49
51
53
50
52
54
52
54
56
Mass (amu)

was done with a thick target with an average interaction energy of ~377 MeV per nucleon (interaction energy ranges from 100 to 570 MeV per nucleon). It is interesting to note that our observed Mn to Cr elemental yield ratio with a value of 1.23, is quite similar to the Mn to Cr cross-section ratio measured at higher energies.

Another noticeable difference between the observed and calculated yields is the case of ^{53}Fe. The observed yield is about one fifth of the calculated yield, while the observed yields of ^{54}Fe and ^{55}Fe are comparable to the calculated yields. Note that the number of neutrons in ^{53}Fe is one less than the magic number 28; this implies that the production of ^{53}Fe involves the removal of a neutron from a complete nuclear shell. Once again, as was in the case for ^{38}K, it appears that the Silberberg and Tsao cross-section formula overestimates the production because it fails to take into account nuclear shell structure.

For the elements Cr through Fe, the isotope yields in Table 3.12 are presented in Table 3.13 in terms of isotope fractions. The isotope fractions for the isotopes of Cr and Mn are plotted (in Gaussian probability scale) in figure 3.22. For the both elements, the observed and calculated yields fit very well to straight lines; in other words, the mass distributions are Gaussian. It appears that peripheral reactions do not alter the Gaussian nature of the mass distribution. The width (standard deviation) of the observed mass distribution is slightly wider than the calculated for Cr and is slightly narrower than the calculated for Mn. The medians of the observed mass distributions are systematicly lower than those of the calculated distributions by more than 0.1 amu.

We have also studied the ratio between the observed and calculated isotope fractions. Figure 3.23 shows the distribution of the ratio of calculated

Table 3.13

Isotope	Fraction of Element	
	Observed	Calculated
^{55}Fe	0.669±.010	0.496±.003
^{54}Fe	0.273±.009	0.268±.002
^{53}Fe	0.058±.005	0.236±.002
^{55}Mn	0.215±.007	0.250±.002
^{54}Mn	0.286±.008	0.356±.003
^{53}Mn	0.305±.008	0.220±.002
^{52}Mn	0.146±.006	0.126±.002
^{51}Mn	0.038±.003	0.040±.001
^{50}Mn	0.010±.002	0.008±.001
^{54}Cr	0.026±.003	0.023±.001
^{53}Cr	0.088±.005	0.129±.002
^{52}Cr	0.294±.009	0.375±.002
^{51}Cr	0.315±.009	0.280±.002
^{50}Cr	0.219±.008	0.157±.002
^{49}Cr	0.058±.004	0.036±.001

Table 3.13 Observed and calculated isotope fractions.

Figure 3.22

Observed and calculated mass distributions for Cr and Mn. The mass distributions are shown in Gaussian probability scale for the fraction of isotopes within an element with mass greater than that indicated by the horizontal axis.

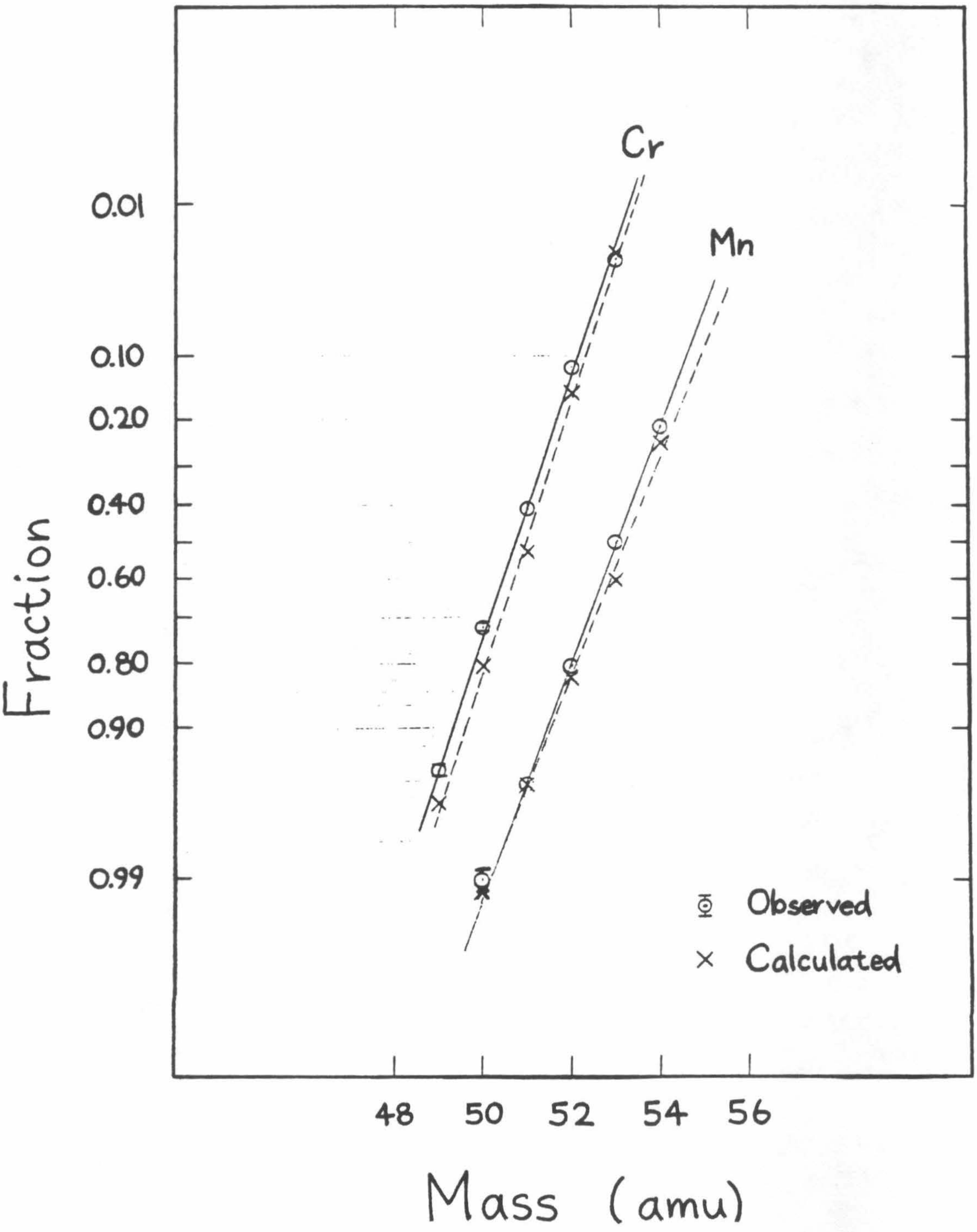
Cr
Mn
0.01
0.10
0.20
0.40
0.60
0.80
0.90
0.99
Fraction
48
50
52
54
56
Mass (amu)
Observed
Calculated

Figure 3.23

Distribution of the ratio of calculated to measured isotope fractions for Cr, Mn, and Fe (with the exception of ^{53}Fe).

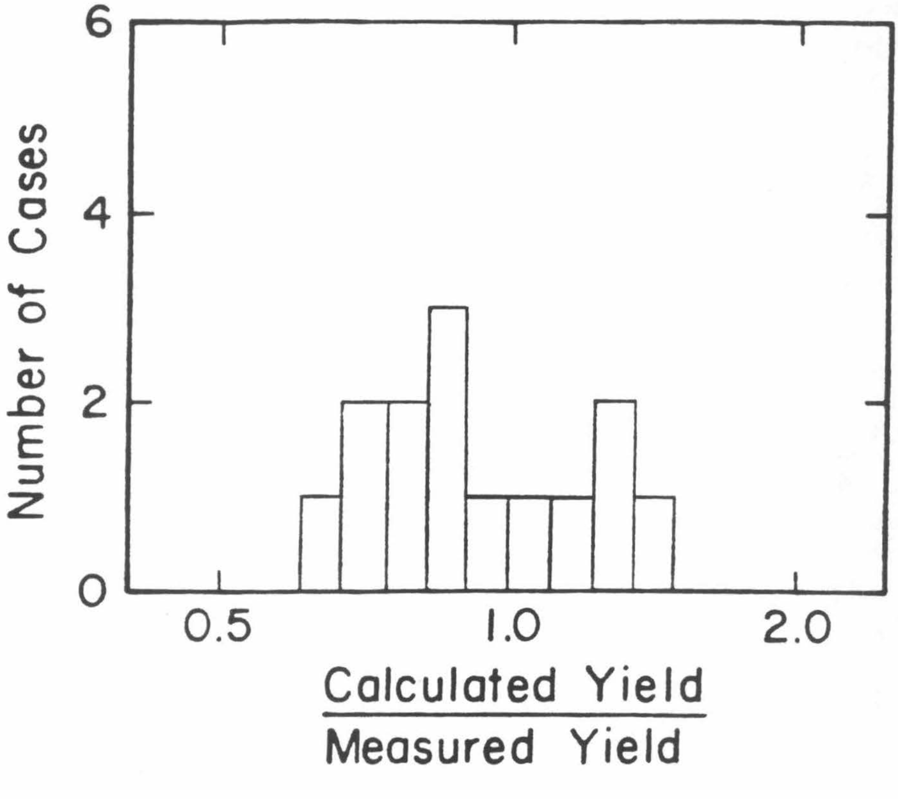
6
4
2
0
Number of Cases
0.5
1.0
2.0
Calculated Yield
Measured Yield

to measured isotope fractions for the isotopes of Cr, Mn, and Fe (with the exception of ^{53}Fe which has a ratio of 4.07). Excluding ^{53}Fe, this distribution has an rms spread of 25%.

We summarize the findings of the ^{56}Fe fragmentation study as follows. The observed Mn to Cr elemental yield ratio is higher than the calculated ratio. The Monte Carlo calculation also over-estimates the production of ^{53}Fe which involves the removal of a neutron from a complete nuclear shell. This suggests that the nuclear shell structure should not be ignored in the semi-empirical formulae. For the elements Cr and Mn, the medians of the observed mass yield distributions are lower than expected from the calculation.

3.4. Summary

Cosmic ray composition studies rely heavily on semi-empirical estimates of the cross-sections for the nuclear fragmentation reactions which alter the composition during propagation through the interstellar medium. In many cases the errors in these cross-section estimates result in significant uncertainties in cosmic ray source abundances or in propagation model parameters derived from observed abundances. To reduce these uncertainties, direct measurements of nuclear fragmentation cross-sections would be desirable. However, measurements of cross-sections are tedious and time consuming and the number of possible nuclear interactions is enormous.

In this chapter, we have presented a method which provides a mechanism for testing the semi-empirical formulae without directly measuring nuclear fragmentation cross-sections. This method involves the comparison of experimentally measured fragmentation yields with those expected from a Monte Carlo simulation calculation based on the semi-empirical cross-section formulae. Even though this method does not provide an absolute measurement of the cross-sections and their energy dependence, any systematic difference between the measurements and calculations can be used as a basis for refining the semi-empirical formulae.

We have presented experimentally measured isotope yields, resulting from the fragmentation of ^{40}Ar and ^{56}Fe in CH_2 targets, with good mass resolutions and statistics. Comparison of our experimentally measured isotope yields with calculated yields shows some significant differences. Some of our measured yields have also been compared with previous work by others which appeared in the literature. Our results are summarized as follows:

- Comparison of our measured relative isotope yields for Ar on CH_2, for the elements Mg through S, with relative cross-sections measured by Viyogi et al. (1978) for Ar on C shows good agreement, suggesting that relative isotope yields do not depend strongly on the target material.
- The medians of the observed mass-yield curves are systematically shifted to lower masses than expected from the calculation. This suggests that adjustments to some of the parameters (which affect the isotope distributions) in the semi-empirical formulae are necessary.
- The observed isotope distributions of S and Cl suggest that the semi-empirical formulae underestimate the yield from peripheral reactions for ^{40}Ar.
- The observed yields of ^{38}K and ^{53}Fe suggest that the semi-empirical formulae overestimate the production of fragments from interactions which involve the removal of a nucleon from a complete nuclear shell.
- In both the Ar and Fe fragmentation cases, when the observed relative isotope fractions (within an individual element) are compared to those of the calculations, the distributions of the ratio have rms spreads of about 25%.

Based on our observed differences between the measured and calculated yields, we conclude that the semi-empirical cross-section formulae could be refined. In particular, the following areas should be examined:

- Nuclear shell structure should be incorporated into the semi-empirical formulae.
- The parameters R, S, and T, which affect the isotope distribution within an element should be examined and re-adjusted. Although the observed distributions are generally Gaussian, systematic differences are evident

when both the median and width of the distributions are compared to the calculations.

- The parameters which affect the fragmentation yields resulting from peripheral reactions from Ar particles should be examined and corrected.

References

Althouse, W.E., et al., "A Cosmic Ray Spectrometer", *IEEE Transactions on Geoscience Electronics* **GE-16**, 204 (1978).

Arens, J.F., "Position-Determining Scintillator", *Nuclear Instruments and Methods* **120**, 275 (1974).

Arens, J.F., et al., "An Instrument to Measure the Spectrum of Cosmic Ray Iron and Other Nuclei to Above 100 GeV-Nucleon", *NASA Technical Memorandum* **79677**, (1978).

Audouze, J., Ephere, M., and Reeves, H., "Spallation of Light Nuclei", *Nuclear Physics* **A97**, 144 (1967).

Barkas, W.H., Berger, M.J., "Tables of Energy Losses and Ranges of Heavy Charged Particles", NASA SP-3013 (1964).

Beck, F., and Yiou, F., "On the Evolution of Element Abundances in Galactic Cosmic Rays", *Astrophysical Letters* **1**, 75 (1968).

Bernas, R., et al., "On the Nucleosynthesis of Lithium, Beryllium and Boron", *Annals of Physics* **44**, 426 (1967).

Bevington, P.R., "Data Reduction and Error Analysis for the Physical Sciences", McGraw-Hill (1969).

Bouffard, M., et al., "The HEAO-3 Cosmic Ray Isotope Spectrometer", *Astrophysics and Space Sciences* **84**, 3 (1982).

Buffington, A., Lau, K.H., and Schindler, S.M., "Position Measurements for Heavy Ion Beams Using a Sodium Iodide Scintillator", *Proc. 17th Int. Cosmic Ray Conf.* **8**, 117 (1981).

Buffington, A., et al., "A Cerenkov-$\Delta E/\Delta X$ Experiment for Measuring Cosmic-Ray Isotopes from Neon through Iron", *Proc. 18th Int. Cosmic Ray Conf.*, paper OG2-7 (1983).

Brautigam, D.A., Chapell, J.H., Kish, J.C., Simpson, G.A., and Webber, W.R., "Fragmentation of Fe Nuclei on Carbon, Hydrogen and CH_2 Targets. I. Individual Charge Changing and Total Cross Sections", *Proc. 18th Int. Cosmic Ray Conf.*, paper OG3.1-2 (1983).

Brautigam, D.A., Chapell, J.H., Kish, J.C., Simpson, G.A., and Webber, W.R., "Fragmentation of Fe Nuclei on Carbon, Hydrogen and CH_2 Targets. II. Isotopic Cross Sections", *Proc. 18th Int. Cosmic Ray Conf.*, paper OG3.1-3 (1983).

Dahlquist, G., and Björck, A, "Numerical Methods", Prentice Hall (1974).

DeBrion, J.P., et al., "Silica Aerogel Cherenkov Counter in a Missing-Mass Experiment", *Nuclear Instruments and Methods* **179**, 61 (1981).

Henning, S., and Svensson, L., "Production of Silica Aerogel", *Physica Scripta* **23**, 697 (1981).

Henning, S., et al., "An Aerogel Cerenkov Counter for the AFS Experiment", *Physica Scripta* **23**, 703 (1981).

Hagen, F.A., "On the Age of Cosmic Rays as Derived From the Abundance of ^{10}Be", *University of Maryland Ph.D. Thesis*, 1976; correction of typographical error in Protheroe, R.J., Ormes J.F., and Comstock, G.M., *Ap. J.* **247**, 362 (1981).

"Harshaw Scintillation Phosphors", 3rd Edition, Harshaw Chemical Company.

Hinshaw, G.F., and Wiedenbeck, M.E., "Quantitative Estimates of the Effects of Cross Section Uncertainties on the Derivation of GCR Source Composition", *Proc. 18th Int. Cosmic Ray Conf.*, paper OG5.2-7 (1983).

Jackson, J.D., "Classical Electrodynamics", second edition, Wiley (1975).

Janni, J.F., "Calculations of Energy Loss, Range, Pathlength, Straggling, Multiple Scattering, and the Probability of Inelastic Nuclear Collisions for 0.1 to 1000 MeV Protons", *Air Force Weapons Lab. Technical Report* no. AFWL-TR-65-150 (1966).

Lau, K.H., Mewaldt, R.A., and Wiedenbeck, M.E., "An Accelerator Test of Semi-Empirical Cross-Sections", *Proc. 18th Int. Cosmic Ray Conf.*, paper OG5.2-5 (1983).

Mewaldt, R.A., Spalding, J.D., Stone, E.C., and Vogt, R.E., "High Resolution Measurements of Galactic Cosmic-ray Neon, Magnesium, and Silicon Isotopes", *Ap. J.* **235**, L95 (1980).

Perron, C., "Cross Sections for Production of Stable and Long-lived Nuclides by High Energy Spallation of iron; Cosmic Ray Implications", *Physical Review* **C 14**, 1108 (1976).

Poferl-Kertzman, M., Freier, P.S., and Waddington, C.J., "Fragmentation of Iron Nuclei", *Proc. 18th Int. Cosmic Ray Conf.* **9**, 187 (1983).

Rogers, E.H., Arens, J.F., and Whiteside, H., "Position-Sensitive Scintillator Detectors", *Nuclear Instrument and Methods* **121**, 599 (1974).

Rasmussen, I.L., et al., "Calibration of An Aerogel Counter of Index 1.1 at The Bevalac" *Proc. 18th Int. Cosmic Ray Conf.*, paper T2-21 (1983).

Rossi, B., "High Energy Particles", Prentice-Hall (1952).

Rudstam, G., "Spallation of Elements in the Mass Range 51-75", *Philosophical Magazine* **46**, 344 (1955).

Rudstam, G., "Spallation of Medium Weight Elements", *University of Uppsala Ph.D. Thesis*, (1956).

Rudstam, G., "Systematics of Spallation Yields", *Zeitschrift fur Naturforschung* **21A**, 1027 (1966).

Rudstam, G., "The Evaporation Step in Spallation Reactions", *Nuclear Physics* **A126**, 401 (1969).

Salamon, M.H., and Ahlen, S.P., "NaI:Tl Response to Relativitic Ne, Ar, and Fe Ions", *Physical Review* **B 24**, 5026 (1981).

Salamon, H.H., and Ahlen, S.P., "Plastic Scintillator Response to Relativisic Ne, Ar, and Fe Ions", *Nuclear Instruments and Methods* **195**, 557 (1982).

Schindler, S.M., Buffington, A., Lau, K.H., and Rasmussen, I.L., "Calibration of A Stack of NaI Scintillators at the Berkeley Bevalac", *Proc. 18th Int. Cosmic Ray Conf.*, paper T2-20 (1983).

Silberberg, R., and Tsao, C.H., "Partial Cross-Sections in High-Energy Nuclear Reactions, and Astrophysical Applications. I. Targets with Z ≤ 28", *Ap. J. Suppl.* **25**, 315 (1973a).

Silberberg, R., and Tsao, C.H., "Partial Cross-Sections in High-Energy Nuclear Reactions, and Astrophysical Applications. II. Targets Heavier Than Nickel", *Ap. J. Suppl.* **25**, 335 (1973b).

Silberberg, R., and Tsao, C.H., "Cross Sections for (*p,xn*) Reactions, and Astrophysical Applications", *Ap. J. Suppl.* **35**, 129 (1977a).

Silberberg, R., and Tsao, C.H., "Modification of Semiempirical Equations for Calculating Partial Cross Sections of p-Nucleus Reactions", *Proc. 15th Int. Cosmic Ray Conf.* **2**, 84 (1977b).

Silberberg, R., and Tsao, C.H., "Calculations of Nucleus-Nucleus Cross Sections, and the Attenuation of Complex Cosmic-Ray Nuclei in the Atmoshpere", *Proc. 15th Int. Cosmic Ray Conf.* **2**, 89 (1977c).

Silberberg, R., and Tsao, C.H., "Improved Semiempirical Estimates of Cross Sections", *Proc. 16th Int. Cosmic Ray Conf.* **2**, 202 (1979).

Silberberg, R., Tsao, C.H., and Letaw, J.R., "Improvement of Calculations of Cross Sections and Cosmic-ray Propagation", *Composition and Origin of Cosmic Rays*, M. M. Shapiro (ed.), 321-336, D. Reidel Publishing Company (1983).

Spalding, J., "The Isotopic Composition of Energetic Particles Emitted from a Large Solar Flare", *Caltech Ph.D. Thesis*, 1983.

Stone, E.C., "Methods for the Determination of Z and M Using dE/dx, Cerenkov, and Total Energy Measurements", Invited paper presented at the ESRO workshop on "Research Goals for Cosmic Ray Astrophysics in the 1980's", Frascati, Italy, 1974.

Stone, E.C., and Wiedenbeck, M.E., "A Secondary Tracer Approach to the Derivation of Galactic Cosmic Ray Source Isotopic Abundances", *Ap. J.* **231**, 95 (1979).

Tsao, C.H., and Silberberg, R., "Improved Semiempirical Estimates of Cross Sections", *Proc. 16th Int. Cosmic Ray Conf.* **2**, 202 (1979).

Viyogi, Y.P., et al., "Fragmentations of ^{40}Ar at 213 MeV/Nucleon", *Physical Review Letters* **42**, 33 (1978).

Webber, W.R., and Brautigam, D., "Fragmentation of ^{56}Fe Nuclei on CH_2, Carbon, and Hydrogen Targets: Individual Charge Changing and Total Cross Sections", *Ap. J.* **260**, 894 (1982).

Westfall, G.D., et al., "Fragmentation of ^{56}Fe", *Physical Review* **C 19**, 1309 (1979).

Wiedenbeck, M.E., and Greiner, D.E., "High-Resolution Observations of the Isotopic Composition of Carbon and Silicon in the Galactic Cosmic Rays", *Ap. J.* **247**, L119 (1981).

Woosley, S.E., "Importance of Isotopic Composition of Iron in Cosmic Rays", *Astrophysics & Space Sci.* **39**, 103 (1976).

Woosley, S.E., and Weaver, T.A., "Anomalous Isotopic Composition of Cosmic Rays", *Ap. J.* **243**, 651 (1981).

Zych, A.D., et al., "Double Scatter Telescope for Medium Energy Gamma Ray Astronomy from A Satellite", *IEEE Transactions in Nuclear Science* **NS-26**, 506 (1979).